

DEVELOPMENT OF n-ZnO/p-Si SINGLE HETEROJUNCTION SOLAR CELL WITH
AND WITHOUT INTERFACIAL LAYER

by

Babar Hussain

A dissertation submitted to the faculty of
The University of North Carolina at Charlotte
in partial fulfillment of the requirements
for the degree of Doctor of Philosophy in
Electrical Engineering

Charlotte

2017

Approved by:

Dr. Yong Zhang

Dr. Michael Fiddy

Dr. Mohamed-Ali Hasan

Dr. Michael Walter

ABSTRACT

BABAR HUSSAIN. Development of n-ZnO/p-Si single heterojunction solar cell with and without interfacial layer. (Under the direction of DR. YONG ZHANG)

The conversion efficiency of conventional silicon (Si) photovoltaic cells has not been improved significantly during last two decades but their cost decreased dramatically during this time. However, the higher price-per-watt of solar cells is still the main bottleneck in their widespread use for power generation. Therefore, new materials need to be explored for the fabrication of solar cells potentially with lower cost and higher efficiency. The n-type zinc oxide (n-ZnO) and p-type Si (p-Si) based single heterojunction solar cell (SHJSC) is one of the several attempts to replace conventional Si single homojunction solar cell technology. There are three inadequacies in the literature related to n-ZnO/p-Si SHJSC: (1) a detailed theoretical analysis to evaluate potential of the solar cell structure, (2) inconsistencies in the reported value of open circuit voltage (V_{OC}) of the solar cell, and (3) lower value of experimentally achieved V_{OC} as compared to theoretical prediction based on band-bending between n-ZnO and p-Si. Furthermore, the scientific community lacks consensus on the optimum growth parameters of ZnO.

In this dissertation, I present simulation and experimental results related to n-ZnO/p-Si SHJSC to fill the gaps mentioned above. Modeling and simulation of the solar cell structure are performed using PC1D and AFORS-HET software taking practical constraints into account to explore the potential of the structure. Also, unnoticed benefits of ZnO in solar cells such as an additional antireflection (AR) effect and low temperature deposition are highlighted. The growth parameters of ZnO using metal organic chemical vapor deposition and sputtering are optimized. The structural, optical, and electrical characterization of ZnO

thin films grown on sapphire and Si substrates is performed. Several n-ZnO/p-Si SHJSC devices are fabricated to confirm the repeatability of the V_{OC} . Moreover, the AR effect of ZnO while working as an n-type layer is experimentally verified. The spatial analysis for thickness uniformity and optical quality of ZnO films is carried out. These properties turn out to play a fundamental role in device performance and so far have been overlooked by the research community. Three different materials are used as a quantum buffer layer at the interface of ZnO and Si to suppress the interface states and improve the V_{OC} . The best measured value of V_{OC} of 359 mV is achieved using amorphous-ZnO (a-ZnO) as the buffer layer at the interface. Finally, supplementary simulations are performed to optimize the valence-band and conduction-band offsets by engineering the bandgap and electron affinity of ZnO.

After we published our initial results related to the feasibility of n-ZnO/p-Si SHJSC [Sol. Energ. Mat. Sol. Cells 139 (2015) 95–100], different research groups have fabricated and reported the solar cell performance with the best efficiency of 7.1% demonstrated very recently by Pietruszka et al. [Sol. Energ. Mat. Sol. Cells 147 (2016) 164–170]. We conclude that major challenge in n-ZnO/p-Si SHJSC is to overcome Fermi-level pinning at the hetero-interface. A potential solution is to use the appropriate material as buffer layer which is confirmed by observing an improvement in V_{OC} using a-ZnO at the interface as buffer layer. Once the interface quality is improved and the experimental value of V_{OC} matched the theoretical prediction, the n-ZnO/p-Si SHJSC can potentially have significant contribution in solar cells industry.

ACKNOWLEDGEMENTS

I had three advisors during different times of my PhD: Dr. Yong Zhang, Dr. Abasifreke Ebong and Dr. Ian Ferguson. I have no words to show my gratitude to Dr. Yong Zhang for careful and detailed review of my PhD dissertation as well as for providing me useful intellectual guidance throughout my PhD. I am grateful to Dr. Abasifreke Ebong for letting me use his suns- V_{OC} system and referring me to Dr. Paul Basore. I am gratified to Dr. Basore who provided me modified files of PC1D software and guided me significantly for my PhD work. I am thankful to Dr. Ian Ferguson for providing me most financial support and resources during my PhD.

I am obliged to show my gratitude to Dr. Michael Fiddy for providing me most intellectual input throughout my PhD. Most importantly, Drs. Michael Fiddy, Yong Zhang, and Paul Basore showed me path to opt a good academic character. One example is that they declined to be a co-author in my papers saying that they did not have enough contribution.

I am indebted to Dr. Mohamed-Ali Hasan and Dr. Michael Walter for useful discussions and guidance throughout my PhD. Additionally, Dr. Michael Walter graciously let me use his equipment in his Lab. I am thankful to Dr. Edward Stokes as well for providing his lab equipment for characterization of my samples. I am obliged to Dr. Christiaan Richter (University of Iceland) for extraordinarily advising and helping me whenever I needed.

I am thankful to Dr. Raphael (Ray) Tsu and Dr. Yogendra Kakad for useful discussions and sharing their interesting and unique experiences of life. I would like to remember Dr. Bharat Joshi (RIP) for his helpful attitude and thanks to Stephanie as well.

I express my appreciation to the Lab managers John Hudak, Lou Deguzman, Robert (Bob) Hudgins, Mark Clayton and undergraduate students Prakash Mishra, Brianna Monroe, Rahi Patel, Justin Stansell, Crystal Conde, Hanin Elathram, Joshua Dulin, and Jeremy Nortey for their technical assistance.

I made so many friends on-campus and off-campus during my PhD and spent so much delighted time with them. It is not possible to include all the names here but I will mention as many as I remember at the time of writing this acknowledgement section; Fevziye, Mutlu, Emre, Mithat, Jyoti, Mark, Gene, Steward, Rochelle, Lila, Yousra, Fida, Maryam, Abeer, Diana, Malik, Halima, Eliza, Jack, Betsy, Naseem, Mehdi, Frances, Zeba, Nian, Ahrar, Veysel, Alekhya, Camilo, Dewayne, Terrance, Eric, Fareeha, Ifeanyi, Maddie, Marl, Tanmay, Fanise and many more. I would like to exclusively mention Ravil Bikmetov for being always available and helpful to me, and Thiara Ortiz for reviewing my dissertation for language mistakes and also helping me in experiments. I am thankful to my teenage friend Waqar who is one of my best friends and helped me to solve many issues in my absence back in Pakistan during my PhD.

I am thankful to my loving parents especially my mother who faced so many hardships for decades to take care of her children. I am thankful to my loving siblings for tolerating my less-responsive attitude. I am especially thankful to my elder sister Noshin for providing me loan in the period of financial crisis during my PhD.

There are many other known and unknown people whom I came across during my life and they helped me in difficult times without expecting any benefit in return. Our world exists because of such people.

*Dedicated to all the vegans, alive or dead, who are/were vegans genuinely
for ethical reasons, not for ego/social status or business reasons.*

LIST OF ABBREVIATIONS

AFM	atomic force microscopy
AFORS-HET	automat for simulation of heterostructures (software)
Ag	silver
Al	aluminum
Al ₂ O ₃	sapphire
ALD	atomic layer deposition
AlN	aluminum nitride
AOS	amorphous oxide semiconductor
AR	antireflection
a-Si	amorphous silicon
a-ZnO	amorphous zinc oxide
BL	buffer layer
BSF	back surface field
CdTe	cadmium telluride
CO ₂	carbon dioxide
c-Si	crystalline silicon
c-ZnO	crystalline zinc oxide
DC	direct current
DEZn	diethyl zinc
DI	deionized
EA	electron affinity

EQE	external quantum efficiency
FET	field effect transistor
FF	fill factor
FWHM	full width at half maximum
Ga	gallium
GaAs	gallium arsenide
GaN	gallium nitride
Gd	gadolinium
HEMT	high electron mobility transistor
HF	hydrofluoric
HIT	heterojunction with intrinsic thin layer
I_0	reverse saturation current
I_D	diode current
I_L	Photo-generated current
In	indium
IQE	internal quantum efficiency
I_{SC}	short circuit current
I_{SH}	current through shunt resistance
ITO	indium tin oxide
I-V	current-voltage
J_{01}	saturation current density
J_{02}	junction reverse saturation current density
J_{SC}	short circuit current density

LCD	liquid crystal display
LPCVD	low pressure chemical vapor deposition
MBE	molecular beam epitaxy
Mg	magnesium
MgO	magnesium oxide
MgZnO	magnesium zinc oxide
MOCVD	metal organic chemical vapor deposition
N ₂	nitrogen gas
NBE	near band edge
Ni	nickel
n-ZnO	n-type zinc oxide
O ₂	oxygen gas
PC1D	personal computer one dimensional (software)
PECVD	plasma enhanced chemical vapor deposition
PERL	passivated emitter rear locally diffused
PL	photoluminescence
PLD	pulsed laser deposition
p-Si	p-type silicon
PV	photovoltaic
PVD	physical vapor deposition
RF	radio frequency
R _S	series resistance
R _{SH}	shunt resistance

SEM	scanning electron microscopy
SHJSC	single heterojunction solar cell
Si	silicon
SiN	silicon nitride
SiO ₂	silicon dioxide
SPR	surface plasmon resonance
TCO	transparent conductive oxide
TEM	transmission electron microscopy
TFT	thin film transistor
TiN	titanium nitride
UV	ultraviolet
V _{oc}	open circuit voltage
XRD	x-ray diffraction
Zn _i	zinc interstitials
ZnO	zinc oxide

TABLE OF CONTENTS

ABSTRACT.....	iii
ACKNOWLEDGEMENTS	v
LIST OF ABBREVIATIONS.....	viii
TABLE OF CONTENTS.....	xii
CHAPTER 1: HETEROJUNCTION SOLAR CELLS AND IMPORTANCE OF ZINC OXIDE	17
1.1 Background	17
1.2 Heterojunction Solar Cells	20
1.3 Zinc Oxide.....	24
1.3.1 Synthesis Techniques of ZnO Thin Films	26
1.3.2 Doping in ZnO	28
1.3.3 ZnO in TFTs and HEMTs.....	30
1.3.4 ZnO as TCO.....	32
1.4 n-ZnO/p-Si Heterojunction Solar Cell	34
1.5 Summary of the Chapter and Outline of Next Chapters	36
CHAPTER 2: ZINC OXIDE GROWTH BY MOCVD AND CHARACTERIZATION.....	40
2.1 Introduction	40
2.2 Materials and Methods.....	41
2.3 Characterization for Growth Temperature Optimization.....	42

2.3.1	Growth Rate Observations	42
2.3.2	Photoluminescence	43
2.3.3	Spectral Reflectance.....	45
2.3.4	Transmittance.....	46
2.3.5	Defining Figure of Merit.....	47
2.4	Spatial analysis of the ZnO Films	48
2.4.1	Photoluminescence	49
2.4.2	Thickness Uniformity	50
2.4.3	Transmittance.....	52
2.5	Summary	53
CHAPTER 3: ZINC OXIDE GROWTH BY SPUTTERING AND CHARACTERIZATION		55
3.1	Introduction	55
3.2	ZnO Deposition by RF Magnetron Sputtering.....	56
3.3	Structural Characterization of ZnO	56
3.3.1	XRD	56
3.3.2	SEM	58
3.3.3	AFM.....	60
3.4	Spatial Analysis of Sputtered ZnO Thin Films	61
3.4.1	Thickness Measurements by Spectral Reflectance.....	61
3.4.2	Photoluminescence	62

3.4.3	Transmittance.....	64
3.4.4	Discussion on Spatial Analysis.....	65
3.5	Summary	67
CHAPTER 4: n-ZnO/p-Si HETEROJUNCTION SOLAR CELL MODELING AND SIMULATIONS		68
4.1	Introduction	68
4.2	Schematic and Modeling of n-ZnO/p-Si Solar Cell.....	69
4.3	Simulations.....	72
4.3.1	PC1D Software	72
4.3.2	Quantum Efficiency	72
4.3.3	Electrical Parameters and Efficiency	74
4.3.4	Effect of Doping Concentration.....	78
4.4	Summary	81
CHAPTER 5: n-ZnO/p-Si HETEROJUNCTION SOLAR CELL FABRICATION AND CHARACTERIZATION		83
5.1	Introduction	83
5.2	Heterojunction Formation	84
5.3	n-ZnO/p-Si Solar Cell Device Fabrication.....	86
5.3.1	ZnO Deposition by RF Sputtering	86
5.3.2	Electrical Characterization.....	86
5.3.3	Contacts Formation by E-Beam Evaporation	88

5.4	Effect of Series Resistance on I-V Measurements	89
5.5	Suns- V_{OC} Measurements	91
5.6	Contribution by Other Researchers	94
5.7	Issues at the Interface of ZnO/Si Heterojunction	97
5.8	Gallium Alloying in ZnO to Increase Bandgap	98
5.9	Summary	101
CHAPTER 6: IMPROVEMENT IN OPEN CIRCUIT VOLTAGE OF n-ZnO/p-Si SOLAR CELL BY USING AMORPHOUS-ZnO AT THE INTERFACE.....		103
6.1	Introduction	103
6.2	Materials and Methods	104
6.3	Characterization Results and Analysis	106
6.3.1	Effects of Type of Wafer on the Crystallinity of ZnO.....	106
6.3.2	Suns- V_{OC} Measurements	108
6.3.3	Antireflection Effect of ZnO.....	110
6.4	Discussion	111
6.4.1	Importance of Buffer Layer	111
6.4.2	Effect of Buffer Layer Thickness	115
6.5	Summary	116
CHAPTER 7: FURTHER SIMULATIONS FOR POTENTIAL IMPROVEMENT IN THE SOLAR CELL PERFORMANCE.....		118
7.1	Introduction	118

7.2	Optimization of Bandgap and Electron Affinity of Zinc Oxide for n-ZnO/p-Si Heterojunction Solar Cell.....	119
7.2.1	Background.....	119
7.2.2	Results and Analysis.....	120
7.3	Bifacial n-ZnO/p-Si Single Heterojunction Solar Cells.....	124
7.3.1	Simulation Procedure.....	124
7.3.2	Results and Discussion.....	125
7.4	Summary.....	131
	CHAPTER 8: CONCLUSIONS.....	133
	REFERENCES.....	141
	PUBLICATIONS.....	152

CHAPTER 1: HETEROJUNCTION SOLAR CELLS AND IMPORTANCE OF ZINC OXIDE

1.1 Background

Energy production is one of the biggest and most rapidly growing sectors globally. The continuous increase in world population and industry will result in 100% increase in global energy consumption by 2050 and CO₂ emission will rise by 150% of the current level [1]. The analysts forecast that investments in renewable energy will reach \$630 billion within a decade. According to International Energy Agency, \$1.3 trillion will have been invested in solar power by 2035 and the world will be producing 662 gigawatts (GW) of solar energy [2]. The worldwide cumulative installed photovoltaic (PV) capacity has already reached 233 GW at the end of year 2015 [3]. It is predictable that solar power generation can contribute prominently to overcome the indisputable problems of global warming and climate change.

Since discovery of the first solar cell in mid-nineteenth century, several individuals including Albert Einstein (Stark-Einstein Law) and groups have contributed to understanding the underlying mechanism of light induced carrier generation/excitation. The first practical solar cell was demonstrated by Bell Laboratories in 1954 using a diffused Si p-n junction having efficiency around 6% [4]. The table 1.1 shows to-date state-of-the-art-efficiencies of different types of research-cells [5]. Although, four-junction concentrator solar cells are reported with an efficiency of 46%, the fabrication cost impedes their extensive use. The Si based solar technology is still one of the most cost effective and

practically feasible options. The table 1.2 shows evolution of silicon solar cell efficiency divided in decades since 1940. The most widely used single junction crystalline Si passivated emitter rear locally diffused (PERL) solar cells have surpassed the milestone of 25% conversion efficiency in lab conditions several years before [6]. But the best achieved conversion efficiency using commercial solar panels is not more than 22%. Although price per watt of Si-based solar modules has dramatically reduced recently, nevertheless, low efficiency and high cost of solar cells are two main bottlenecks in widespread use of solar panels. The efficiency of standard silicon solar cells has improved by only 2% during last more than two decades as shown in Fig. 1.1. Therefore, it is important that new materials and structures should be explored to make new solar cell devices which may have higher efficiency and lower cost.

Table 1.1. Best Research Solar Cell Efficiencies [5]

Solar Cell Type	To Date Efficiency in Lab (%)
<i>Multijunction cells (2-terminal, monolithic)</i>	
Four junction (concentrator)	46.0
Three junction (concentrator)	44.4
Three junction (non-concentrator)	37.9
Two junction (non-concentrator)	29.8
<i>Single junction GaAs cells</i>	
Concentrator	29.1
Non-concentrator	28.8
<i>Crystalline Si cells</i>	
Single crystal (concentrator)	27.6
Single crystal (non-concentrator)	25.0
Silicon heterostructures (HIT)	25.6
Multicrystalline	21.2
<i>Thin film chalcogenide</i>	
CIGS	21.0
CdTe	21.0
<i>Other emerging technologies</i>	
Perovskite thin film	20.0
Dye sensitized	14.0
Organic thin film	11.0
Amorphous Si	10.2

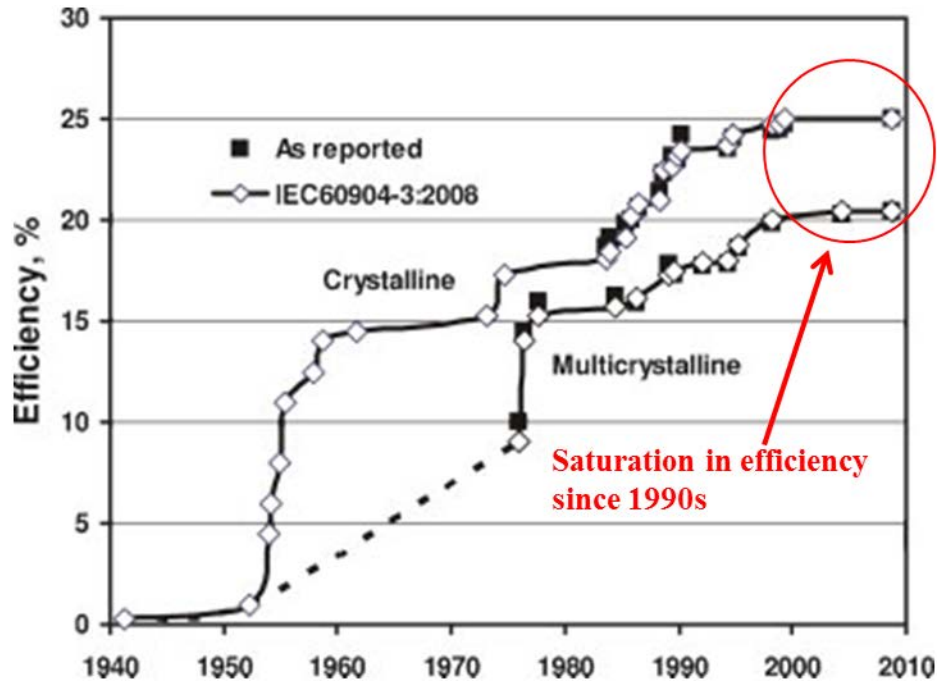


Fig. 1.1. Improvement in efficiency of single junction Si solar cell since 1940 [6].

Table 1.2. Evolution of silicon solar cell efficiency divided in decades since 1940

Decade	Description	Efficiency	Major Organizations	Refs.
1940s	First Si solar cell was reported in 1941	<1%	Bell Labs	[7]
1950s	First major improvement in efficiencies occurred by development of crystal growth/junction diffusion techniques and the refinement of the cell and contact design	1–14%	Bell Labs & Hoffman Electronics	[8] [9] [10]
1960s	<i>No major improvement</i>	-	-	-
1970s	Second major improvement phase occurred by using shallow junctions, metallization by photolithography, and improved antireflection coating and surface texturing	15–18%	COMSAT Labs	[11] [12]
1980s	Third major phase of improvement arose resulted from progress in surface passivation, bulk lifetimes, contact passivation and light trapping in the cell	18–24%	University of NSW	[13]
1990s	<i>No major improvement</i>	-	-	-
2000s	The revision of standard solar spectrum resulted in 25% efficiency milestone in 2009	25%	University of NSW	[6]
2010s	<i>No major improvement to date</i>	-	-	-

1.2 Heterojunction Solar Cells

The advantages of hetero p-n junction solar cell are the liberty to choose material, layer thickness, dopant concentrations, inherent surface passivation, and low temperature approach [14] [15]. The most standard type of heterojunction solar cell uses hydrogenated amorphous silicon (a-Si:H) to create a-Si:H(n,p)/c-Si(p,n) structure. The fundamental challenge in this and other heterojunction solar cells is to avoid recombination due to interface states which is mostly addressed by inserting a buffer layer. The key to the success of heterojunction solar cells lies in separation of highly recombination-active contacts from the crystalline semiconductor surface by the insertion of a passivating semiconductor film with a wider bandgap [16]. For heterojunction solar cell, a-Si:H is an ideal candidate as a buffer layer because its bandgap is wider than that of c-Si and it can be n- or p-doped relatively easily enabling the fabrication of electronic heterojunction for solar cell.

The first a-Si:H/c-Si heterostructures were studied in 1970s and it was found that a-Si:H films passivate c-Si surface extraordinarily well [17] [18]. In 1983, Hamakawa et al. reported first Si heterojunction solar cell by depositing a-Si:H on poly-Si film [19] [20]. Contemporarily, the heterojunction between a-Si:H and c-Si was extensively investigated [21] [22]. Motivated by the study of the detailed properties of low-temperature emitters applicable to thin film poly-Si solar cells in 1990 [23], Sanyo (Japan) started working on the development of c-Si based heterojunction solar cells. Initially, devices composed of n-type c-Si wafer and a thin boron-doped a-Si:H(p) produced efficiencies around 12% with a reasonable fill factor. The device characterization revealed a large reverse current density, indicating large interface state density. The insertion of a thin buffer layer of undoped a-Si:H between doped emitter and wafer significantly reduced interface state density and

increased the efficiency up to 14.5%. This configuration is commonly known as Heterojunction with Intrinsic Thin-layer (HIT) structure. The introduction of the buffer layer mainly improved the open circuit voltage (V_{OC}) by 30 mV. This result prompted the importance of having a heterostructure contact at the rear side of the solar cell. Implementing a similar heterostructure as a passivating back contact enhanced the cell efficiency to over 18% [24].

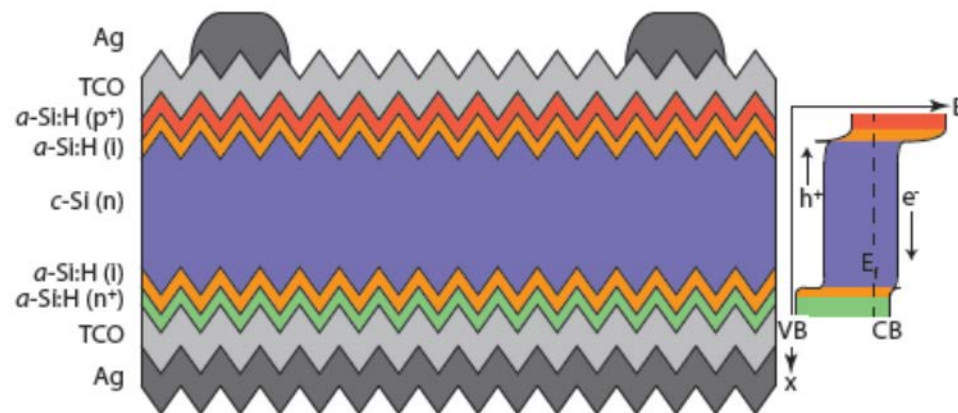


Figure 1.2. The schematic of the a-Si:H/c-Si heterojunction solar cell with front and rear buffer layers, as developed by Sanyo, and its band diagram [15].

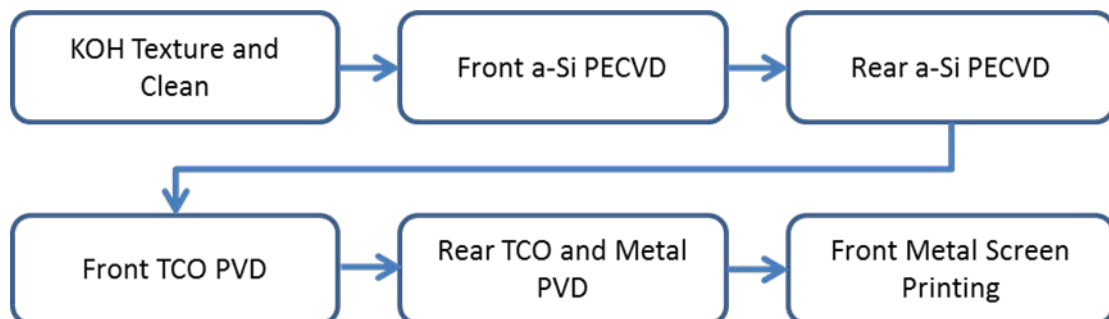


Figure 1.3. Basic process steps for a-Si:H/c-Si heterojunction solar cell devices.

The schematic of the a-Si:H/c-Si heterojunction solar cell with front and rear buffer layers, as developed by Sanyo, and its band diagram are illustrated in Fig. 1.2. In 2000, Sanyo reported an open circuit voltage of 702 mV and an efficiency of 20.1% for a solar

cell with the area of 101 cm^2 [25]. The solar cell was fabricated at a temperature of less than $200 \text{ }^\circ\text{C}$. The main reasons of this high efficiency were; optimization of surface treatment by carrier lifetime measurements, high quality doped layers, and control of the texturing process. In 2011, loss mechanism in HIT solar cells was examined which led to the improvements in optical and electrical properties of the transparent conductive oxide (TCO) layer, the metal grid electrode, and the window layer [26]. As a result, the conversion efficiency of 23.7% was achieved with an open circuit voltage, short circuit current density, and fill factor of 745 mV, 39.38 mA/cm^2 , and 80.9%, respectively, for a cell area of 100.7 cm^2 .

The fabrication process of HIT solar cell is depicted in Fig. 1.3. On the front (illuminated) side of solar cell, an intrinsic a-Si:H passivation layer and a p-doped a-Si:H emitter are deposited on an n-type c-Si wafer successively using plasma enhanced chemical vapor deposition (PECVD). On top of the structure, a TCO film with a low sheet resistance is deposited by physical vapor deposition (PVD). A metallic grid is then screen-printed at the front for current collection. On the rear side, an intrinsic a-Si:H passivation layer is followed by deposition of n-type a-Si:H film for back surface field (BSF). On this doped film, a TCO layer and then a metallic contact layer are deposited. Alternatively, a TCO layer followed by a metallic grid can be used. The device can then be finished with either a white back sheet for standard solar modules or a transparent back sheet for bifacial solar module. The interface recombination is yet an impediment in making efficient heterojunction solar cells.

By making some assumptions, Wilhelm et al. [27] proved the recombination rate (R) at a heterostructure depends on the interface recombination velocity of holes (S_p) as

$$R \approx S_p p_a^{if} \quad (1.1)$$

where p_a^{if} is the hole concentration on the absorber (Si in our case) side of interface. The direct relation between saturation current density (needs to be minimized) and interface recombination velocity of holes is

$$J_0 = e S_p N_{v,a} \exp\left(\frac{E_{n,w}}{kT}\right) \exp\left(-\frac{E_A}{AkT}\right) \quad (1.2)$$

where e is the electronic charge, $N_{v,a}$ is the effective density of states in the absorber valence band, $E_{n,w}$ is the energy difference between the conduction band edge and the electron quasi-Fermi level in the window layer (ZnO in our case), E_A is the activation energy that would be the bandgap for a Si homo-junction, but reduced in a type II heterostructure, as shown in Fig. 1.4, and A is the diode ideality factor. The activation energy can be approximated as

$$E_A \approx E_{g,Si} - \Delta E_C \quad (1.3)$$

where $E_{g,Si}$ is the bandgap of Si and ΔE_C is the conduction band offset. The ideality factor depends on material parameters as [28]

$$A = 1 + \frac{\varepsilon_a N_{A,a}}{\varepsilon_w N_{D,w}} \quad (1.4)$$

where ε_a and ε_w are the relative permittivities, and $N_{A,a}$ and $N_{D,w}$ are the doping densities of the absorber and window, respectively. The values of A can be engineered depending on the ratio of the doping densities of Si and ZnO. Simple algebraic manipulations in basic diode equations relating open circuit voltage (V_{oc}) and short circuit current density (J_{sc}) of the solar cell infer

$$V_{oc} = \frac{E_A}{e} - \frac{AkT}{e} \ln\left(\frac{J_{0,r}}{J_{sc}}\right) \quad (1.5)$$

where $J_{0,r}$ is the reference current density of the saturation current density normally having a large value (on the order of 10^5 A/cm²). Equations (1.4) and (1.5) indicate that in order to have A small and V_{oc} large, n-doping density in ZnO must be much larger than p-doping density in Si ($N_{D,w} \gg N_{A,a}$).

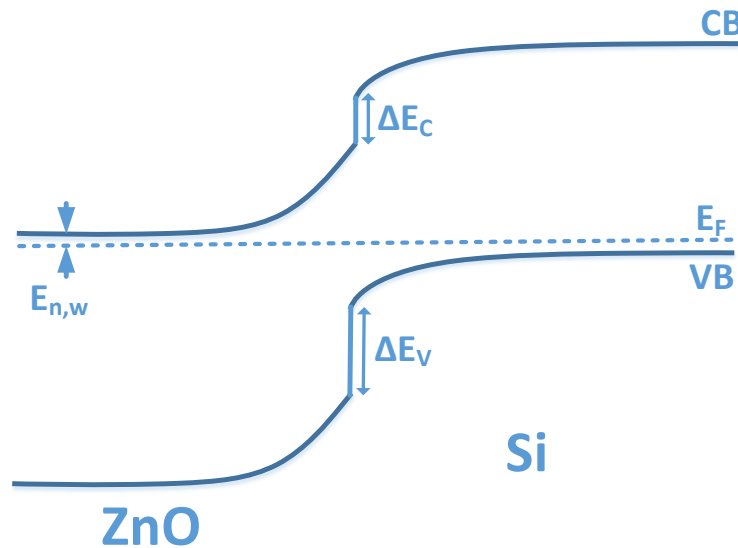


Figure 1.4. Basic band diagram of n-ZnO/p-Si single heterojunction solar cell. CB: conduction band, VB: valence band, E_F : fermi level, ΔE_C : conduction band offset, ΔE_V : valence band offset.

1.3 Zinc Oxide

With the increased demand for high power and high temperature optoelectronic devices, wide-bandgap semiconductor materials have drawn major attention from researchers and industry in recent years. These materials have additional advantages including light emission/absorption in the UV/visible range, broad transmission, a large piezoelectric effect, high breakdown voltages, and low electronic noise. Zinc oxide (ZnO) is a compound semiconductor with wide bandgap tunable from 3 to 4 eV with doping or alloying. Its unique advantages over other II-VI and III-V wide-bandgap materials include lower processing costs, low-level of toxicity, and natural abundance. The relatively small

refractive index of ZnO compared to gallium nitride (GaN) results in larger exciton binding energy (60 meV), much greater than kT at room temperature guarantees efficient luminescent and photovoltaic characteristics. The wurtzite structure with tetrahedral arrangement is the most stable form of ZnO with lattice parameters $a=3.25 \text{ \AA}$ and $c=5.21 \text{ \AA}$ which make it a potential substrate for another widely used material GaN [29]. This allows fabrication of useful heterostructures for complex optical and electronic devices. The c/a ratio of ZnO wurtzite structure is 1.603 which is very close to the ideal ratio (1.633) for highly stable structures. The non-centrosymmetric wurtzite structure of ZnO gives rise to large piezoelectric and pyroelectric coefficients resulting in its potential use in mechanical sensors and nanogenerators [30]. Extensive research has been carried out on the fabrication and use of ZnO nanostructures owing to its stable morphological structure. In addition, the use of amorphous oxide semiconductors has appeared as a new technology which may overcome many of the problems associated with conventional silicon technology [31]. A review of recent advances in oxide semiconductors shows that amorphous ZnO appears to have the most desirable properties of all the amorphous oxide semiconductors [32]. The high electron mobility and wide bandgap of ZnO make it a suitable candidate for fabrication of thin film transistors (TFTs) and high electron mobility transistors (HEMTs) [33] [34] [35]. Aluminum- or gallium-doped ZnO has recently gained much attention as a suitable replacement for indium tin oxide (ITO), which is comparatively expensive material and less stable in hydrogen plasma, in fabrication of transparent conducting oxide (TCO) thin films [36] [37] [38] [39].

1.3.1 Synthesis Techniques of ZnO Thin Films

Several methods have been used to grow high quality doped and undoped ZnO films [40] [41]. The most common methods are magnetron sputtering [42] [43], pulsed laser deposition (PLD) [44] [45], molecular beam epitaxy (MBE) [33] [34], ion plating [46] and MOCVD [37] [39] [47]. The main advantage of magnetron sputtering which makes it suitable for ZnO growth is that materials with high melting point can be easily sputtered where evaporation of such materials is difficult. But diffuse transport, a characteristic of sputtering, results in contamination problems. The sputtering method may cause poor reproducibility from run to run due to its low controllability over film composition [35]. Also, dynamic control for multiple layer growth is demanding in sputtering as compared to PLD and MOCVD. ZnO porous thin films can be easily produced using PLD at room temperature [48]. The films grown by PLD are free of impurities with good stoichiometric control, but uniformity in thickness and other characteristics of the film is a big challenge in PLD. It is also difficult to scale-up PLD equipment for large wafers. The basic setup of PLD is simple as compared to other techniques but physical phenomena of laser-material interaction are very complicated. It is well accepted that MBE is one of the best choices to achieve high purity and crystallinity of ZnO thin films. Magnesium doped ZnO films with high carrier concentration and high mobility have been achieved using MBE [33] [34] for high current electronic devices. The absence of carrier gas leads to highest purity of the ZnO films. Besides, disadvantages of this method are graded edges of grown films, low growth rate, and high cost to implement and preserve. Transparent conducting polycrystalline Gallium doped ZnO films with different thicknesses have been deposited on glass substrates at temperatures as low as 200 °C using ion plating method [46];

however, like MBE, low deposition rate and high cost for equipment and maintenance are some of the shortcomings of ion plating.

Using MOCVD, ZnO can be grown at moderate temperatures ($<500\text{ }^{\circ}\text{C}$) with growth rate above $2\text{ }\mu\text{m/hr}$ which leads to sharp interfaces with low inter diffusion [49]. The MOCVD technique has many other benefits like high controllability of film structure, deposition of high quality films over large areas, and possibility of scaling up the process to commercial base production [35]. Higher temperature growth is possible in MOCVD therefore the process is thermodynamically favorable. So far, various studies have been reported about optimized parameters for ZnO thin film growth using MOCVD for specific applications. S. Nicolay et al. have studied orientation and surface morphology evolution of ZnO films with different thicknesses grown on Schott glass substrates using low pressure MOCVD at different temperatures [50]. Proposing a growth model for polycrystalline ZnO thin films, the authors have demonstrated that preferred orientation of films changes from c-axis to a-axis as the growth temperature is increased from $110\text{ }^{\circ}\text{C}$ to $220\text{ }^{\circ}\text{C}$ and then returns back to c-axis at $380\text{ }^{\circ}\text{C}$. Many other researchers have reported optimized growth parameters for ZnO using MOCVD such as VI/II ratio, growth temperature, and pressure [51] [52] [53] [54].

There are some advantages associated with sputtering as compared to MOCVD. It is possible to implement shadow-mask lithography in sputtering if ZnO (or any other material) needs to be deposited on selected areas. Also, source vapors can penetrate below the substrate in case of MOCVD causing unwanted growth of material at back side of substrate where this is not possible in sputtering. Thickness uniformity of the film is an important parameter because thickness directly affects physical properties of the single- or

multi-layer structure and thus performance of the device. Also, it plays important role in sample evaluation especially in electrical characterizations like Hall and 4-probe measurements because thickness is a fundamental factor which is used to calculate carrier concentration, lifetime, resistivity, and mobility of the sample. Uniformity in thickness distribution over the surface of ZnO films prepared by sputtering is better than the films produced by MOCVD [55] according to characterization results of the samples produced in our Labs.

1.3.2 Doping in ZnO

Although ZnO is getting enormous attention due to its unique properties and potential applications in thin film transistors, coatings and transparent conductors, there is a major difficulty associated with ZnO that hinders its use in various electrical and optical devices. This problem is the lack of understanding and controlling the conductivity, especially p-type, in ZnO. Undoped ZnO naturally has n-type conductivity with carrier concentration ranging from 10^{16} to 10^{18} cm^{-3} depending on the growth methods and conditions. The undoped samples that I have prepared using MOCVD and sputtering showed electron concentration on the order of 10^{18} cm^{-3} . The unintentional n-type conductivity in ZnO has been attributed to oxygen vacancies and/or zinc interstitials, however, it has been argued that hydrogen and other impurities are more responsible for this behavior [56] [57]. As compared to p-type doping, it is easy to achieve n-doped ZnO layers with desired carrier concentration using different techniques. Various researchers have reported n-doped ZnO thin films by incorporating Mg [33] [34], In [58], Al [59], Ga [36] [60] and their combinations. But it is still a challenge to obtain reproducible, consistent, reliable and highly conductive p-type ZnO thin films and nanostructures.

In 2000, Aoki et al. demonstrated fabrication of ZnO based short wavelength diodes using excimer-laser doping technique by growing phosphorous-doped p-type ZnO layer on an n-type ZnO substrate [61]. Then Kim et al. in 2003 reported very interesting results about phosphorous-doped p-type ZnO preparation on sapphire substrate [62] by radio frequency sputtering method. Initially, phosphorous-doped ZnO films showed n-type behavior with electron concentration in the range of 10^{16} to 10^{17} cm^{-3} . These films were then converted to p-type by a thermal annealing process at a temperature above 800 °C under nitrogen flow. The Hall measurements of different films of the p-type ZnO films revealed a hole concentration of 1×10^{17} to 1.7×10^{19} cm^{-3} , a mobility of 0.53 to 3.51 $\text{cm}^2\text{V}^{-1}\text{s}^{-1}$, and resistivity of 0.59 to 4.4 Ωcm . In a review [63] on p-type doping of ZnO, well organized data is reported about the work by various researchers using different growth techniques and different dopants such as nitrogen, arsenic, and phosphorous. Recently, Ding et al. have published two papers reporting p-type ZnO grown on m-plane and r-plane sapphire substrate using plasma assisted MBE method [64] [65]. Prior to ZnO growth at higher temperature, buffer layers were grown at lower temperature to improve the structure quality of the top film. Some reports correlate 3.31 eV (A-band) as an optical signature of p-doping of ZnO [66] [67]. According to these reports, basal plane stacking faults are mainly responsible for the A-band. A comprehensive analysis of this relationship is discussed and very detailed theoretical and experimental evidence is provided in support of association between stacking faults, 3.31 eV luminescence, and p-type doping of ZnO. Nevertheless, it is well known that p-type doping of ZnO is not completely understood and a lot of work is required to establish reliable techniques to grow p-type ZnO structures. The

two industrial applications of ZnO that require only n-type ZnO are discussed in next two subsections.

1.3.3 ZnO in TFTs and HEMTs

Problems related to p-type doping in ZnO are well known. Therefore, the most feasible and practical application of ZnO is to fabricate high frequency and high power field effect transistors (FETs) which is well supported by currently available semiconductor technology. The FETs may not need a pn junction avoiding p-type doping of ZnO. A substantial improvement in electrical and optical properties due to formation of two-dimensional electron gas at the heterostructure interface of ZnO and MgZnO in a strained ZnO potential well has been reported [68].

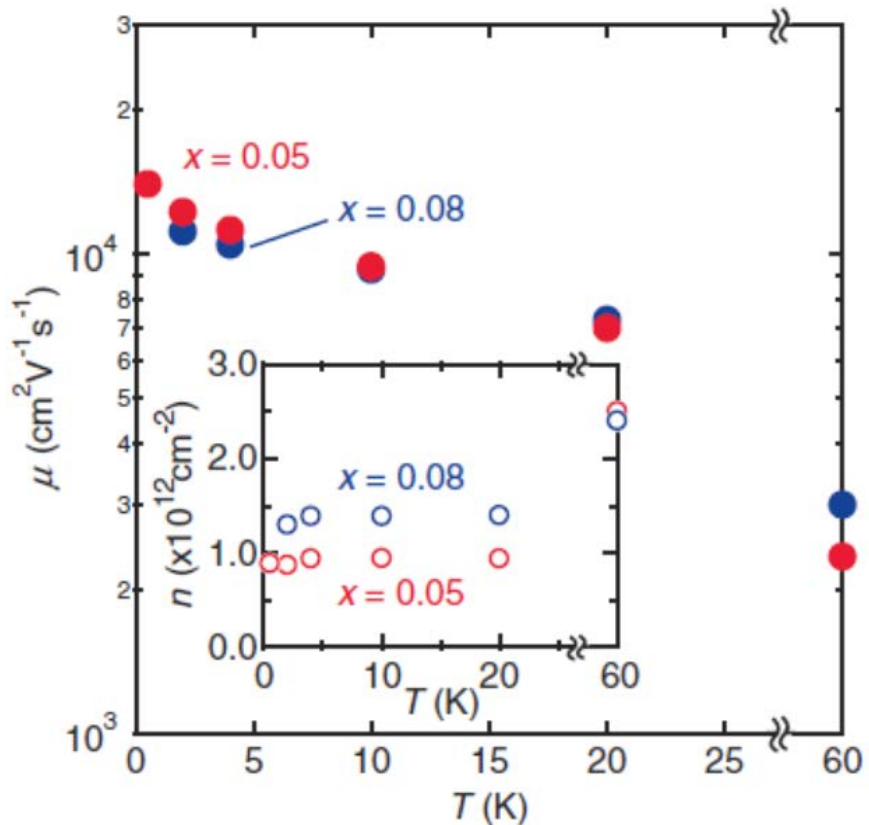


Fig. 1.5. Influence of temperature on electron mobility and electron concentration (inset) of ZnO/MgZnO heterostructures for two different compositions (5% and 8%) of Mg [33].

In 2008, Tsukazaki et al. achieved high electron mobility ($14000 \text{ cm}^2\text{V}^{-1}\text{s}^{-1}$) at low temperature due to strong two-dimensional confinement of electrons by growing ZnO/MgZnO heterostructures using plasma induced MBE [33]. This work exhibits the possibility of ZnO based high performance HEMTs. Figure 1.5 shows dependence of mobility and carrier concentration of ZnO/MgZnO heterostructures on temperature demonstrated by Tsukazaki et al. A similar study demonstrated the mechanism and origin of two-dimensional electron gas in ZnO/MgZnO heterostructures [34]. The increase in carrier concentration and mobility with incorporation of Magnesium, reported in this study, is illustrated in Fig. 1.6. The highest carrier concentration and mobility at room temperature were obtained for Magnesium composition of 0.61.

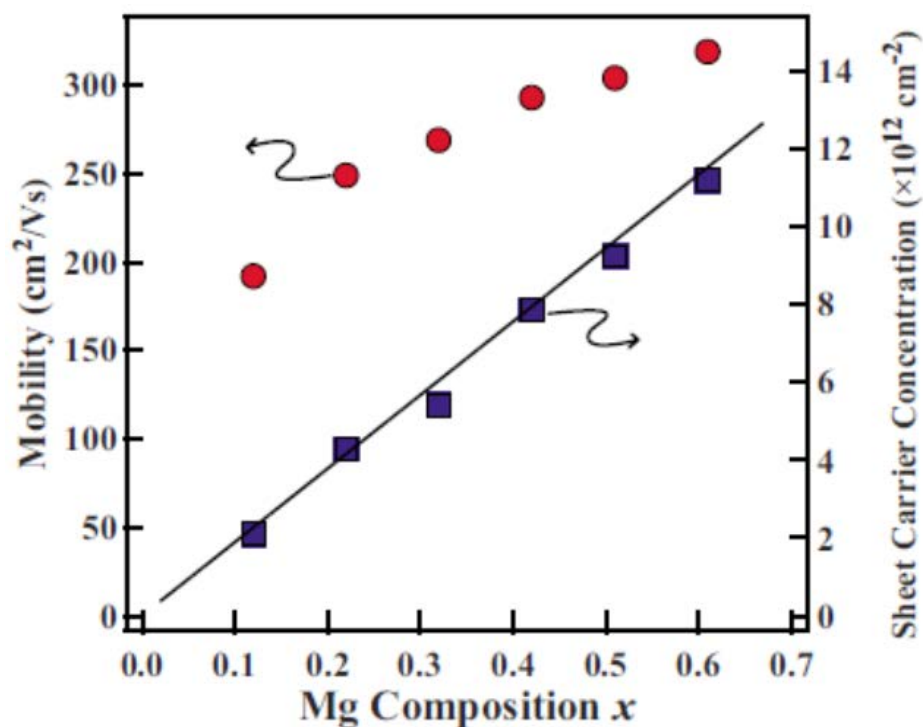


Fig. 1.6. Increase in mobility and carrier concentration with increase in Mg incorporation [34].

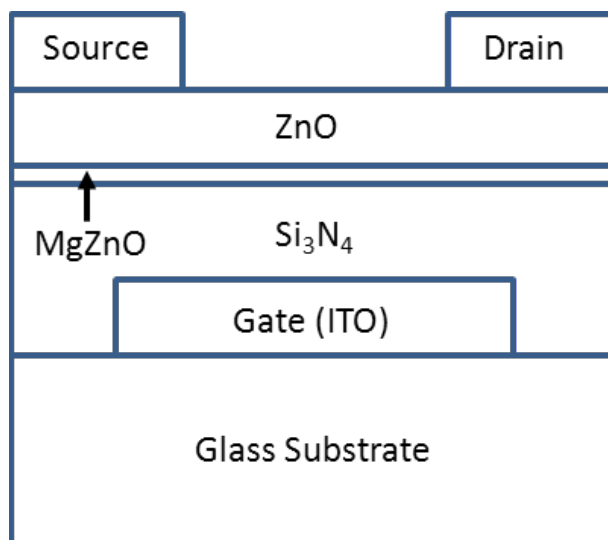


Fig. 1.7. A schematic showing bottom-gate ZnO TFT structure with enhanced electrical characteristics by introducing a thin MgZnO layer at channel-gate insulator interface.

A scheme for bottom-gated ZnO TFTs with enhanced electrical characteristics grown by MOCVD on glass substrate has been proposed [35]. The schematic is shown in Fig. 1.7 which illustrates incorporation of a thin MgZnO layer at the channel-gate insulator interface. The mobility, on/off current ratio, turn on voltage, and subthreshold slope for ZnO TFTs without MgZnO layer were $2.3 \text{ cm}^2\text{V}^{-1}\text{s}^{-1}$, 6.4×10^7 , -6.75 V , and 0.78 V/decade , respectively. The same features for ZnO TFTs with MgZnO layer (Fig. 1.7) were measured as $9.1 \text{ cm}^2\text{V}^{-1}\text{s}^{-1}$, 2.3×10^8 , -2.75 V , and 0.38 V/decade , respectively. The results achieved in this study are very promising to employ HEMT-type TFTs fabricating ZnO/MgZnO heterostructures on glass substrate. These TFTs can be used in displays, ultraviolet detectors, and transparent electronics.

1.3.4 ZnO as TCO

A new category of semiconductor materials, amorphous oxides semiconductors (AOS), reveals an exciting combination of high optical transparency and high electron mobility. Transparent liquid crystal display (LCD) panels, an important application of AOS based

TFTs, enable a person to look through the panel like glass. These panels consume 90% less energy as compared to conventional flat panels using back light unit. After a few demonstrations of ZnO TFTs based completely transparent devices in 2003 [69] [70], oxide semiconductor based TFTs started becoming a feasible technology. The number of publications per year related to oxide based TFTs in a decade (2001-2010) are depicted in Fig. 1.8 [32]. The data reveal that binary and complex zinc oxides seem to be the best compounds for oxide TFT applications.

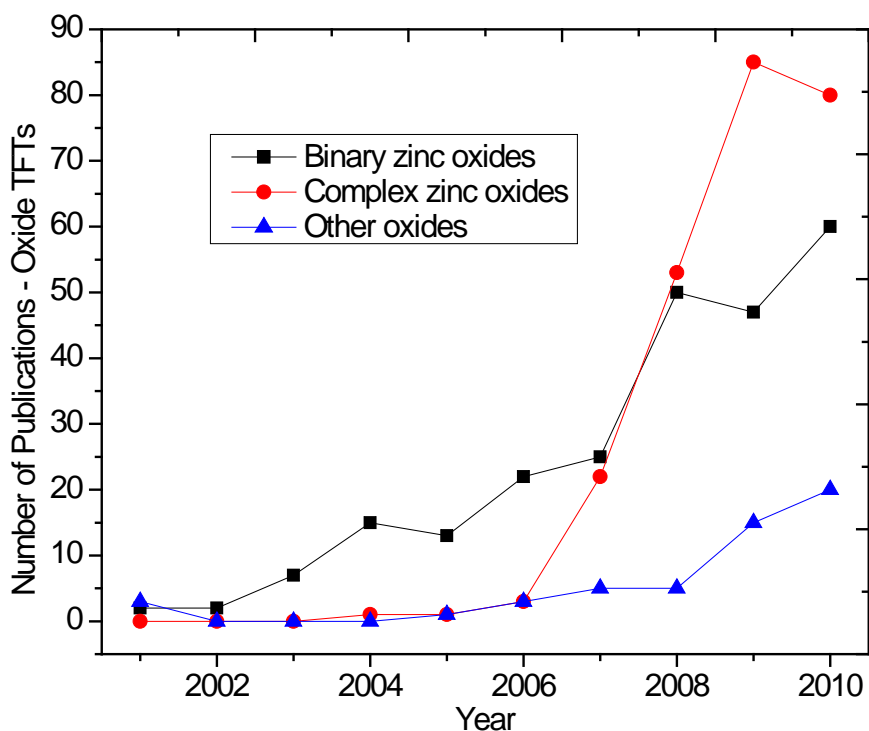


Fig. 1.8. The number of publications per year from 2001 to 2010 related to binary ZnO, complex ZnO, and other oxides based TFTs [32].

Recently, Bernal et al. presented an optical study of CuInGaSe₂ (CIGS) solar cells in order to improve the device performance by selecting ZnO:Al as TCO layer and optimizing its thickness [71]. In 2009, Nayak et al. [36] demonstrated Ga-doped ZnO transparent conducting thin films for optoelectronic device applications using sol-gel spin coating

technique. The transparency of the films was more than 80% with resistivity as low as $3.3 \times 10^{-3} \Omega\text{cm}$ with 2 at% Ga. Contemporarily, Huang et al. [37] and Zhao et al. [38] reported highly transparent Ga doped ZnO thin films with low resistivity using MOCVD. Huang et al. achieved highest transparency of 85%, mobility of $30.4 \text{ cm}^2\text{V}^{-1}\text{s}^{-1}$, and lowest resistivity of $3.6 \times 10^{-4} \Omega\text{cm}$. Also, the optical bandgap of Ga-doped ZnO increased from 3.26 to 3.71 eV with increase in Ga incorporation due to Burstein Moss shift. Zhao et al. achieved bandgap engineering of Ga-rich GaZnO thin films in a range of 3.3–4.9 eV by varying the Ga content. Previously, a similar work was carried out fabricating high quality single-crystal Ga-doped ZnO films on sapphire substrate using low-pressure MOCVD to investigate influence of Ga doping on structural, electrical, and optical properties [39].

1.4 n-ZnO/p-Si Heterojunction Solar Cell

High fabrication cost in order to realize the appropriate structure necessary for high efficiency is a serious drawback for the Si *pn*-homojunction solar cells. As a result, heterojunction solar cells (HJSCs) prepared by depositing wide bandgap TCO on Si wafer has gained significant attention because of simpler manufacturing steps, lower processing temperature and lower fabrication cost. The conversion efficiency of 15% for indium tin oxide (ITO)/Si HJSC was achieved long before [72], but due to limited quantity of indium on earth, a substitute for ITO is required for large-scale production of TCO/Si HJSC.

During last decade, zinc oxide (ZnO) has drawn attention of the semiconductor industry after the awareness that ZnO is one of the rare semiconductors that retain magnetic properties above room temperature [73]. Because of the recognition of ZnO and the requirement of an ITO substitute, the research and industry attention in regards to n-ZnO/p-Si HJSCs got invigorated. Furthermore, ZnO as compared to ITO is better with respect to

its band alignment with CIGS. ZnO satisfies all the six criteria established for the solar cell device designers when considering any new material, which are unconstrained supply of material, low variability of key processes, low production cost, potential further cost reduction, environmental safety and health issues, and reliability/lifetime [74]. In 2006, Ibrahim and Ashour claimed 6.6% conversion efficiency of ZnO/Si HJSC prepared by depositing aluminum (Al)-doped n-ZnO (AZO) thin films on p-Si by spray pyrolysis [75]. In 2008, Zhang et al. demonstrated fabrication and characterization of ZnO/Si HJSC by deposition of intrinsic ZnO on p-Si substrates using DC reactive sputtering [76]. The variations in PV efficiency was investigated with varying deposition conditions in order to understand the photoelectric conversion behavior of the ZnO/Si heterojunction. In 2010, Shen et al. reported 0.7–1.14% conversion efficiency of the n-ZnO/p-Si HJSC fabricated by DC magnetron sputtering [77]. The authors analyzed the dark and light I-V curves to investigate the influence of interface states, back contact barrier, and series resistance in determining the solar cell performance. Knutsen et al. recently recognized by numerical simulations that conduction band offset in n-ZnO/p-Si HJSC is serious impediment to obtain high efficiency [78]. They theoretically proposed that, alloying ZnO with magnesium (Mg), the conduction band of ZnO can be raised so that the effect of recombination centers at the interface can be strongly reduced enabling high efficiency despite recombination velocities as high as 10^6 cm/s. Baturay et al. very recently reported deposition of intrinsic as well as gadolinium (Gd)-doped ZnO films on p-Si wafers to fabricate HJSC [79]. It was concluded that the heterojunction formed with 1% Gd-doped ZnO had the strongest rectification, highest barrier height, and the lowest series resistance. Contemporarily, it was theoretically proved that efficiency as high as 19% can be achieved

by n-ZnO/p-Si HJSC with the fabrication cost much lower than conventional Si solar cells [80]. The best experimental efficiency of 7.1% for n-ZnO/p-Si HJSC is recently reported by Pietruszka et al. using atomic layer deposition (ALD) [81]. Utilizing the model proposed by Knutsen et al. [78], they have incorporated Mg in ZnO to reduce conduction band offset between ZnO and Si that resulted in higher conversion efficiency.

The main reason behind the difference between theoretically predicted and practically achieved conversion efficiency of n-ZnO/p-Si HJSC is that experimental open circuit voltage (V_{OC}) is much lower than the predicted value of V_{OC} (~650 mV) based on band-bending between n-ZnO and p-Si. Most of the researchers attribute this lower value of V_{OC} to the interface states because of lattice mismatch between ZnO and Si. In 2015, we have achieved experimental value of V_{OC} as 260 mV after preparing several samples of n-ZnO/p-Si HJSC by depositing intrinsic ZnO on p-Si wafers by RF magnetron sputtering [82]. This value of V_{OC} is very close to the recently reported values 292 mV [79] and 257 mV [81] but much lower than the values reported by other researchers earlier as 520 mV [75], 350 mV [76], 400 mV [77], and >330 mV [78] proving discrepancies in V_{OC} values of n-ZnO/p-Si HJSC stated in the literature. Based on the understanding of HIT solar cells and ZnO TFTs, there is a need to introduce an interfacial layer for ZnO/Si HJSCs to improve the device performance especially V_{OC} .

1.5 Summary of the Chapter and Outline of Next Chapters

This chapter summarized background and evolution of the solar cell efficiency over several decades. History of the heterojunction solar cell with reference to Si HIT structure was deliberated in detail. Also, the steps involved in fabrication of Si HIT solar cell were discussed. A brief review was presented on synthesis and applications of ZnO which is a

rapidly emerging material in semiconductor device applications. Different synthesis techniques to grow ZnO thin films were discussed with more emphasis on MOCVD and Sputtering which are the most common and well established techniques for ZnO growth and which I have used to fabricate n-ZnO/p-Si solar cell samples. The most prevalent problem in fabrication of ZnO based devices, the p-type doping, was discussed with references to previous and current investigations on doping in ZnO. The prominent applications of n-ZnO, FETs and transparent conducting oxides, were reviewed. At the end, a brief review on the previous work related to n-ZnO/p-Si single heterojunction solar cell (SHJSC) was presented.

Experimental work starts from chapter 2 which covers the details of ZnO thin film growth using MOCVD, characterization, and optimization of parameters. Spatial analysis is also carried out to evaluate thickness uniformity over the surface of sample and also the optical properties are characterized as a function of distance from the center of the wafer in the sample. A figure of merit is defined to evaluate the overall quality of ZnO thin films.

In chapter 3, I present deposition of ZnO using RF magnetron sputtering and structural characterization using XRD, SEM, and AFM. The growth temperature and RF power for ZnO crystal quality are optimized by iterative experiments. Also, spatial thickness uniformity and optical quality were evaluated and compared with ZnO thin films prepared by MOCVD.

Chapter 4 includes modeling and simulations of n-ZnO/p-Si single heterojunction solar cell. Electrical parameters, doping concentrations in ZnO and Si, and internal/external quantum efficiencies are evaluated using well known personal-computer-one-dimensional

(PC1D) software. The optimized parameters of the solar cell structure are listed with best achieved values of electrical parameters, fill factor, and power conversion efficiency.

In chapter 5, I discuss type-II n-ZnO/p-Si heterojunction formation with the help of band-bending diagram and Anderson's rule. Experimental steps for n-ZnO/p-Si SHJSC device fabrication and electrical characterization by Hall and suns- V_{OC} measurements are presented. The possible reasons and potential solutions of the lower experimental value of V_{OC} are discussed. Furthermore, preparation of Ga-doped ZnO films is demonstrated to study effective bandgap widening of ZnO to utilize maximum possible energy of the solar spectrum.

The last phase of experiments is demonstrated in chapter 6. Preparation of n-ZnO/p-Si heterojunction solar cells using three different materials (AlN, a-Si and a-ZnO) at the interface as the buffer layer to reduce recombination velocity as well as avoid oxide (SiO_2) formation during ZnO deposition at higher temperature is presented. The effects of wafer selection on the performance of the finally fabricated device are also studied. Furthermore, an additional advantage of ZnO as an antireflection coating was experimentally verified for different thicknesses of ZnO film.

In chapter 7, optimization of bandgap and electron affinity of ZnO to enhance the conversion efficiency of ZnO/Si single heterojunction solar cell is performed by PC1D simulations. It is predicted that the open circuit voltage of n-ZnO/p-Si single heterojunction solar cell can be significantly improved by tuning bandgap and/or electron affinity of ZnO by doping or alloying. The major reason of improvement in the solar cell efficiency is enhanced band-bending due to decrease in conduction-band offset which increases built-in voltage. Furthermore, simulations are performed to evaluate the potential of n-ZnO/p-Si

bifacial solar cells. Two different structures of ZnO/Si solar cell are simulated one with doped BSF and other with charge passivated BSF.

Finally, conclusions and summary of the dissertation is provided in chapter 8. The thesis is restated, and the major points are synthesized to bridge the whole work and to highlight the importance of the idea. Potential future work is also briefly proposed.

CHAPTER 2: ZINC OXIDE GROWTH BY MOCVD AND CHARACTERIZATION

2.1 Introduction

Each method of growing thin films or nanostructures has merits associated with certain materials. Recent literature has turned a renewed eye to the MOCVD method due to its capability to transition to mass production fairly easily. MOCVD simply requires a metallorganic vapor carried (mixing occurs via a bubbler) by some nonreactive carrier gas (N_2 , Ar, etc.) to interact with the other reactants in a heated, vacuum-pressurized control chamber [83]. In the chamber, the molecular bonds of precursors break due to the increased free energy created by the heat, and the adatoms are then adsorbed onto the substrate. On the substrate, the product nucleates layer-by-layer forming an epitaxial film on the substrate. The issue with MOCVD is the multiplicity of determinants involved in each deposition, making optimization of the process a painstaking issue in the advancement of the method. Despite the facts that ZnO is one of the best candidates for future devices due to its tunable direct wide bandgap, natural abundance, low toxicity, highly stable wurtzite structure, large piezoelectric and pyroelectric coefficients, and richest nanostructural configuration, growth of ZnO films and nanostructures is still in a developing stage. Semiconductors community still lacks consensus on the optimized parameters of ZnO growth using MOCVD [37] [49] [51] [50] [84]. Extensive efforts are needed to investigate the dynamics during ZnO growth using specific precursors, substrates, and carrier gas to find an optimized window of the growth parameters. In this chapter, results are presented related to growth of several ZnO samples using MOCVD on Sapphire substrates using

most common precursors and carrier gas at a range of temperature. Pressure, flow rates, VI/II ratio, and rotation speed of the susceptor were kept constant to optimize the MOCVD process with respect to temperature with zinc oxide as a focal point.

2.2 Materials and Methods

For the deposition, a homemade MOCVD apparatus was utilized. Zinc oxide was grown on sapphire (Al_2O_3) substrates on a rotating graphite susceptor with different temperatures from 300 °C to 600 °C with a step size of 50 °C. Precursor reactants were diethylzinc (DEZn) as the zinc source, pure oxygen gas (O_2) as the oxygen source, and nitrogen (N_2) as the carrier gas. The susceptor rotated at a fixed speed of 800 rpm [85]. The chamber pressure was held at a set point of 3 torr. The flow rates of oxygen and the carrier gas (nitrogen) were 1000 and 100 sccm respectively. The bubbler pressure was around 180 torr and diethylzinc (DEZn) was kept at constant temperature of 5 °C resulting in vapor pressure of DEZn about 5 torr. This resulted in VI/II ratio of around 330. Substrates were pre-cleaned to remove dust with a sequence of acetone, methanol, isopropanol, and distilled water, then dried with compressed nitrogen. They were loaded one-at-a-time onto the susceptor and allowed to grow for variable amounts of time.

Four types of measurement were conducted on the films. The first was an *in-situ* reflectance measurement through an Epimetric spectrometer, which generated an intensity graph by which growth could be monitored by undulations in the reflectance curves over time (contextualizing this, the curves appeared as cosine curves). Each undulation implied around 175 nm increase in thickness of the film during growth. This is based on the well-known relation

$$2nd \times \cos \theta = m\lambda \quad (2.1)$$

where n is the refractive index at wavelength λ of the growing material, d is the film thickness, and m is the order of undulations. Considering angle of incidence $\theta \approx 0$ and $n \approx 2$ (in our case for ZnO at 700 nm), the approximate thickness relation becomes $d \approx \lambda/4$. Photoluminescence (PL) was conducted with a mini PL/Raman spectrophotometer from Photon Systems (and associated software) in order to determine the crystallinity and crystal quality of the films. A UV-vis Hamamatsu light source was connected to a lens to conduct spectral reflectance and transmittance measurements, which were then read by a Filmetrics spectrophotometer.

2.3 Characterization for Growth Temperature Optimization

2.3.1 Growth Rate Observations

The relationship between temperature and growth rate is largely an issue of kinetic energy. Growth rates for each temperature are summarized in Table 2.1. At low temperature, molecules do not have the energy to overcome pre-existing bonds. This was why the growth rate for the sample grown at 300 °C was exceptionally low; it was thermodynamically impaired in its ability to break reactant molecular bonds. The growth rate remains consistent for all samples grown from 350 °C to 550 °C. The sample grown at 600 °C had a notably lower growth rate, which suggests that it was also impaired somehow. We attribute this to excess of kinetic energy. The excess of kinetic energy made the adatoms less apt to settle into crystal configuration immediately decreasing the perceived growth rate of the epitaxial crystal. Furthermore, high growth temperature has empirically led to desorption of adsorbed reactants and oxygen vacancies in the crystal. In the work of Ye et al., the cracking effect of high temperature growth allowed more effective Zn adatoms but led to a higher rate of oxygen desorption [86]. Ye's discussion

contextualizes our results, which in turn are corroborated by various mathematical models for organic oxygen precursors. The literature suggests an increase in growth rate up to about 400 °C for such oxygen precursors and a stable growth rate until a peak growth temperature after which the growth rate falls again [87]. Our work is about the optimization of the process using pure oxygen gas precursors.

TABLE 2.1. Growth rates for temperatures from 300 to 600 °C

Temperature (°C)	Thickness (nm)	Growth Time (min)	Growth Rate (nm/min)
300	358.69	30	11.96
350	594.09	23	25.83
400	602.09	23	26.18
450	499.66	20	24.98
500	502.96	20	25.15
550	583.88	23	25.39
600	468.01	30	15.60

2.3.2 Photoluminescence

Photoluminescence (PL) spectrometry measures radiative recombination of photo-excited electrons with the holes left in the lower states. PL can provide useful information about the crystallinity of material. Zinc oxide has a characteristic bandgap of 3.34 eV in bulk. The narrower the full-width-at-half-maximum (FWHM) around the highest peak of the PL spectrum, the better the crystal quality [85]. The PL measurement system has a built-in UV- laser with a wavelength 250 nm that corresponds to photon energy of 4.96 eV which is sufficient to excite ZnO sample that has a bandgap around 3.3 eV. The step size of wavelength was set to 1 nm to get a detailed view of the PL spectra. All the measurements were made at room temperature. As seen in Fig. 2.1, the FWHM decreased as temperature increased from 300 °C to 550 °C. However, above 550 °C, the samples

showed an increase in FWHM, suggesting excessive kinetic energy of adatoms above 550 °C causing haphazard nucleation and degradation in crystal quality.

Past papers have suggested a number of other optimal growth temperatures. Huang et al. suggested a temperature of 500 °C as optimal, but this was for gallium-doped films [37]. Other papers using the slower-to-oxidize butanol suggested optimal temperatures in the 400s [49] [51], but our samples were grown using pure oxygen source and different pressure. At lower pressures, furthermore, a lower temperature is allowable due to decreased need of kinetic energy of adatoms [50]. Our FWHM data seem to agree with the data of Wu et al. [84] in finding an optimal growth temperature around 500 °C.

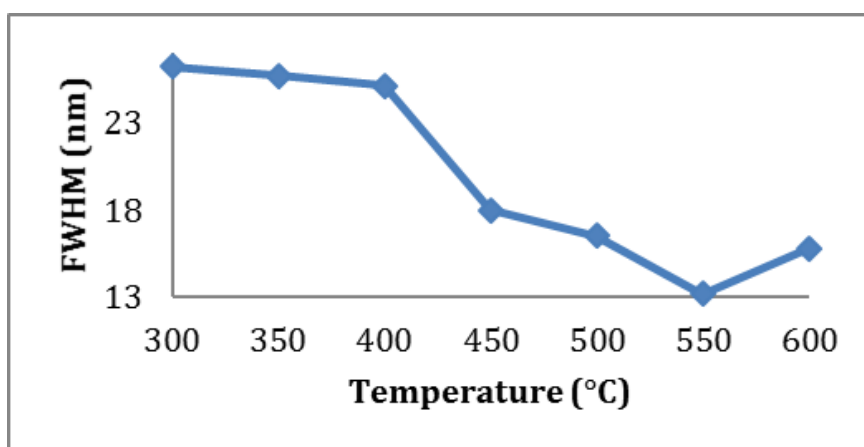


Fig. 2.1. FWHM of PL spectra of the samples grown at various temperatures. The FWHM narrows with increasing temperature until desorption causes it to rise at 600° C.

Looking at the actual intensity of the maximum peak, we see a pattern that corresponds to the FWHM data. The PL peak intensity (on a log scale) increases with the temperature as exhibited in Fig. 2.2, implying again a positive correlation, until 550 °C, after which the peak intensity lowered (in the sample grown at 600 °C). Complete PL spectra of the samples are illustrated in Fig. 2.3.

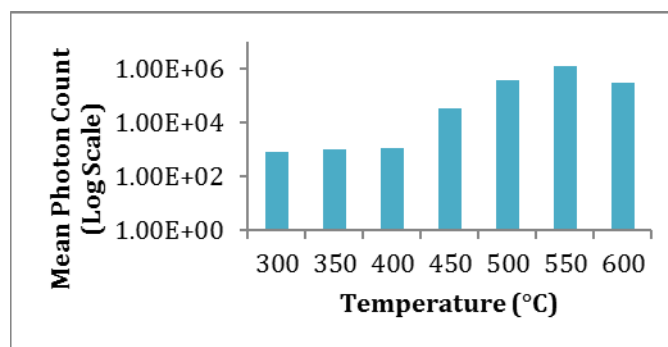


Fig. 2.2. Intensity of PL peak increases with growth temperature, indicating increasing sample quality.

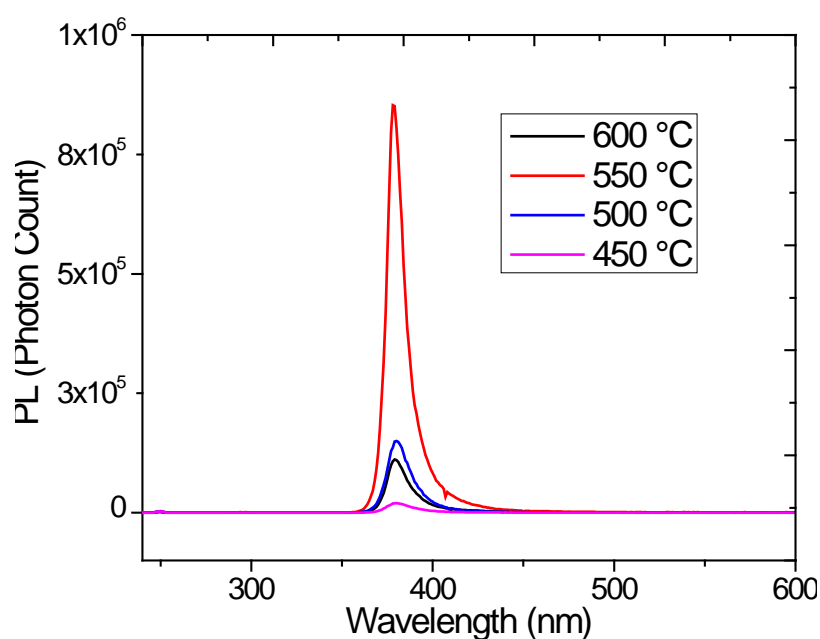


Fig. 2.3. PL spectra for samples grown at growth temperatures from 300-600 °C. PL peaks of the samples grown below 450 °C would not be visible on the linear scale, so are omitted.

2.3.3 Spectral Reflectance

Using spectral reflectance, three measurements were extracted with each sample: the thickness (d) of the sample (Table 2.2), the accuracy of the thickness measurement (%), and the roughness of the sample. The latter two data points are not reported due to a relative consistency in films grown at all temperatures, but thicknesses were intentionally centered around 500 nm. From the data in Table 2.2, though thicknesses were the same in samples

grown at high temperatures, narrower FWHM and higher exciton peak emission were maintained. The degraded crystallinity associated with the higher thickness [40] due to higher defect concentration is somehow ameliorated by the increasing temperature. Thus, increasing temperature seems to lead to an increase in the crystallinity, an effect we define as thermal rectification. However, the roughness of the samples shows a positive correlation with increasing temperature until 550 °C (it drops, like peak intensity and other PL parameters, in the sample grown at 600 °C), meaning that samples are also less “smooth” as temperature increases. These two patterns may be explained by the increased motion of adatoms, allowing them to fill the vacancies.

2.3.4 Transmittance

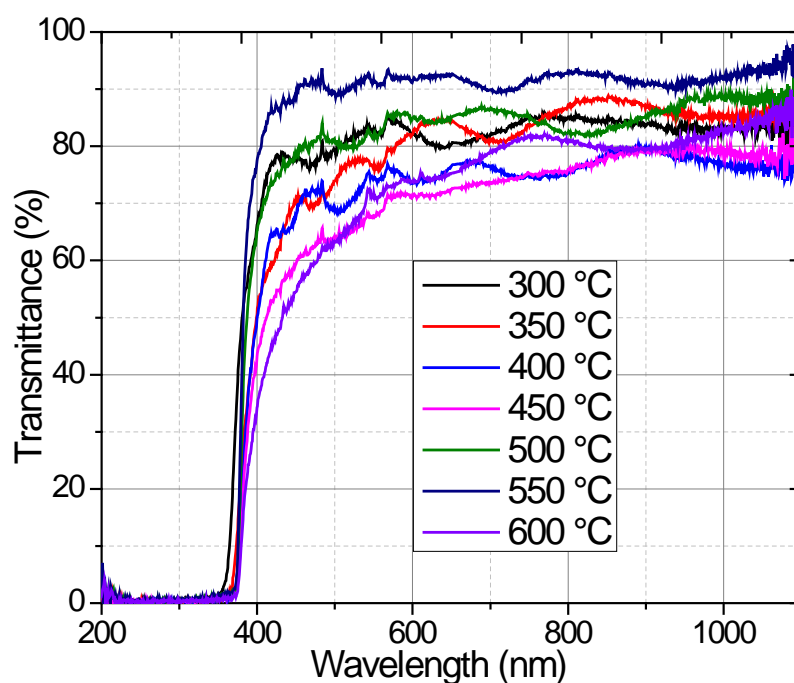


Fig. 2.4. Transmittance spectra for samples grown at temperatures from 300-600 °C. The sample grown at 550 °C has maximum transmission below the bandgap.

The transmittance measurements are graphed in Fig. 2.4. Transmittances below the bandgap were relatively low for all samples, except for that at around 550 °C. The threshold

for inclusion in a transparent conducting oxide solar cell is about 86% [88], which is met only for the samples grown at 550 °C. Tan et al.'s findings corroborate ours in that we can also see that in the sample grown at 400 °C, the transmittance was analogous to that of the sample at 600 °C [89]. The film at 300 °C was unstable during growth so that it was difficult to grow the film nearly as thick as other films, which led to higher transmittance for this sample than most of others, as can be observed in Fig. 2.4.

2.3.5 Defining Figure of Merit

The PL FWHM and peak intensity, film thickness, and average transmittance of the samples grown at different temperatures are summarized in Table 2. From these values, we have defined a temperature-dependent figure of merit for the crystal quality (F_{cq}) as

$$F_{cq} = \frac{f}{d \times p \times T_{av}} \quad (2.2)$$

where f is FWHM (nm) of PL spectrum, d (nm) is film thickness, p is the peak intensity of PL, and T_{av} is the average transmittance at wavelength range of 400–1000 nm. The value of the figure of merit ' F_{cq} ' is desired to be minimized. Applying this equation to the values in Table 2, we obtain the values plotted in Fig. 5. The graph shows that F_{cq} has optimized value for ZnO thin films grown at 550 °C.

TABLE 2.2. Parameters used to calculate figure of merit

Temperature (°C)	PL FWHM (nm)	Film Thickness (nm)	PL Peak Intensity (Photon Count)	T_{ave} (%)
300	26.2	358.69	787	82.23
350	25.7	594.09	972	81.70
400	25.1	602.09	1113	74.88
450	18.0	499.66	31940	72.91
500	16.5	502.96	383885	84.18
550	13.2	579.22	1195532	91.31
600	15.8	467.47	284713	75.27

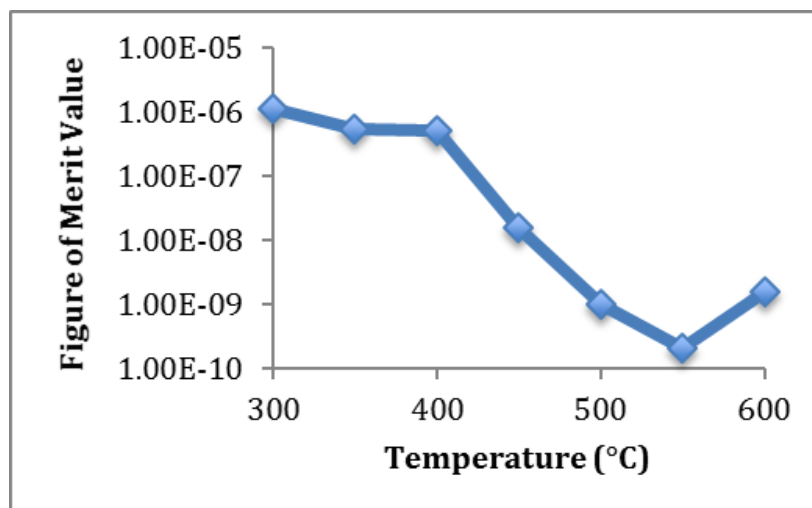


Fig. 2.5. Figure of merit is plotted using values from Table 2.2 from Eq. 2.2.

2.4 Spatial analysis of the ZnO Films

The degradation in device performance based on thin film due to thickness non-uniformity is an important issue in semiconductor device fabrication. Spatial thickness uniformity is an important parameter because it directly affects physical properties and performance of thin film device as well as plays important role in characterization of the material/device. From device point of view, there is a direct relation between thickness uniformity and performance of the thin film solar cell device because spatial thickness distribution influences the electrical and optical properties of thin films.

We experimentally studied the spatial consistency of ZnO thin film with an average thickness of about 500 nm deposition on a sapphire substrate. Measurements were made on five distinct points on the sample to compare transmittance, photoluminescence, thickness, and roughness. The five measurement points were marked front, back, left, right, and center (Fig. 2.6), each 0.5" from the center of the sample having 2" diameter.

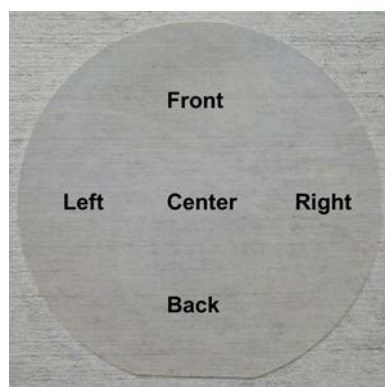


Fig. 2.6. ZnO thin film sample on sapphire substrate with five measurement points labeled.

2.4.1 Photoluminescence

Photoluminescence was used to characterize defect concentration and determine spatial crystal behaviors. Fig. 2.7 demonstrates the full width at half maximum (FWHM) at each of the five points on the sample. FWHM seems to vary more along the back-front axis than it does along the left-right axis. For reference, Fig. 2.8 provides a photoluminescence spectrum for one of the samples, grown at 550 °C. Although sample was rotating during the growth but the difference in crystal quality at different spots is evident. We attribute this difference to the inertial and viscous forces over the surface of the susceptor and the dynamics of the groove used to hold the sample.

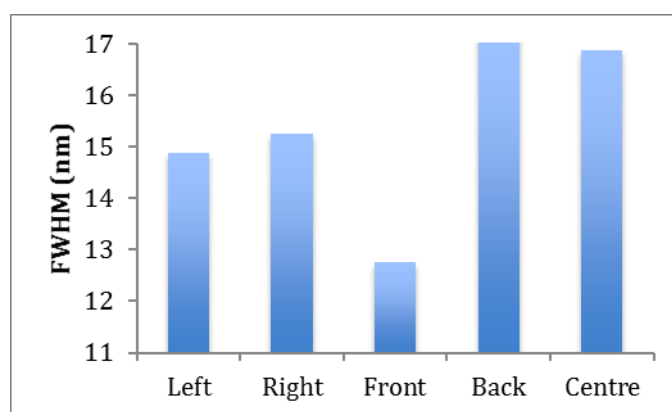


Fig. 2.7. Full width at half-maximum of the PL spectra at each of 5 points measured at room temperature.

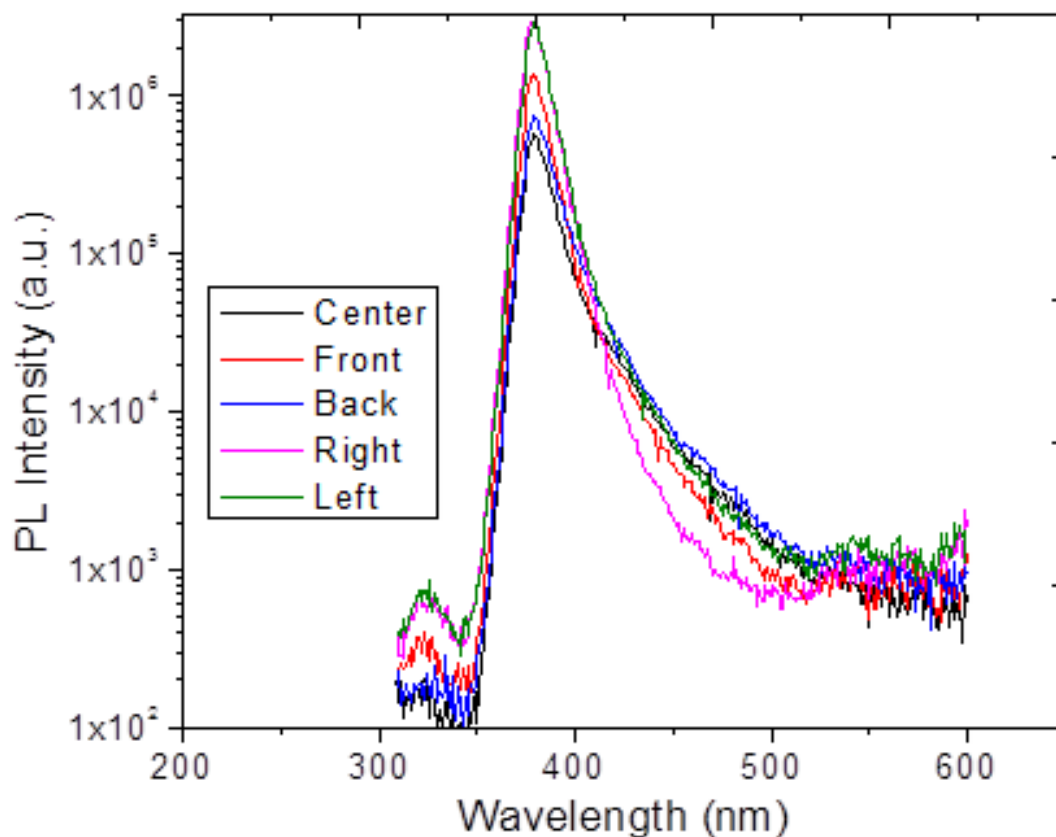


Fig. 2.8. Photoluminescence spectra at five different points for a sample grown at 600 °C.

2.4.2 Thickness Uniformity

Spectral reflectance data is used by Filmetrics tool in an algorithm to calculate three values: the thickness of the sample, the roughness at the surface of the sample, and the fitting accuracy of the algorithm. All accuracies are above 95%. The roughness and thickness values are presented in Fig. 2.9. Roughness of the samples is visibly consistent across the substrate. Thickness deviations are marginal (~ 20 nm) for all regions but the front, which had a deviation of nearly 70 nm.

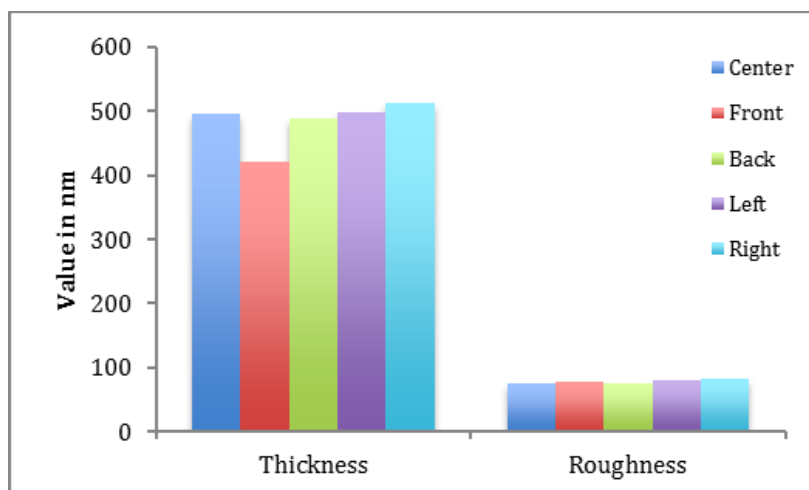


Fig. 2.9. Values of thickness and root mean square roughness as obtained by spectral reflectance by spatial positioning.

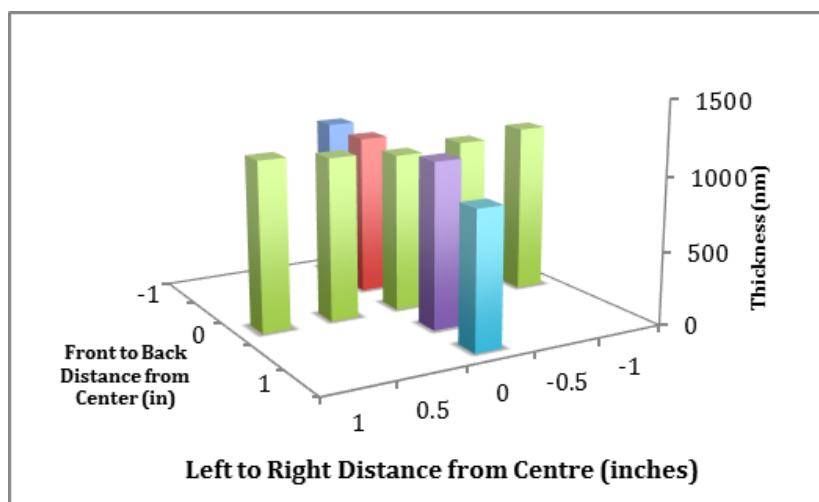


Fig. 2.10. Thickness at 5 points along each axes left-to-right and front-to-back. Positive gradients visible in all four directions from center, with the exception of the negative gradient in the backward direction.

To understand the nature of these thickness variations, we further investigated an additional two points on each axis, intermediary with respect to the measured points and the center on one of the samples. These results are plotted in Fig. 2.10 for a different (thicker) ZnO film. From the figure, we can see a clear gradient-style activity along both axes emanating from the center. The only area to show a decrease with emanation distance

is the back-side of the front-to-back axis, attributed to the fact that it is distal with relation to the sources of the gas, placed near the outer edge of the susceptor [90].

2.4.3 Transmittance

Transmittance spectra for all samples were relatively consistent. The average transmittances at the five points over the wavelength range of 390 – 1100 nm are plotted in Fig. 2.11. Transmittance for the average photocell window layer is >80% [88], which is a criterion met by the front, back, right, and center regions of the samples measured on average. However, the left region shows lower rates of transmittance through the film. As the thicknesses are relatively consistent across the substrate, the lower transmittance of the left region can be attributed to the crystal quality of the ZnO film.

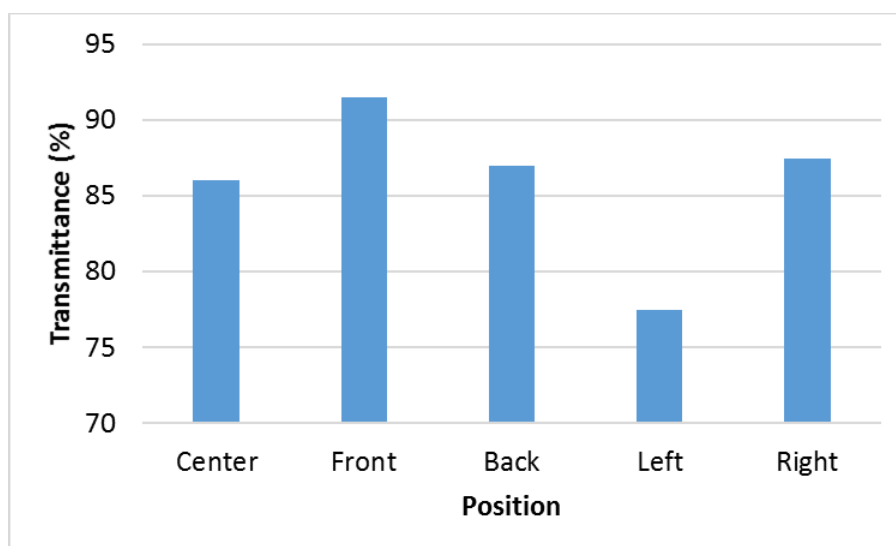


Fig. 2.11. Average transmittance values for wavelength range 400 to 1000 nm.

All of the characteristics discussed above can be attributed to the position of the substrate on the susceptor in MOCVD reactor [91]. The standard deviation of the measured values at different point on the substrate are summarized in Table 2.3.

Table 2.3. The average of all PL-FWHM, transmittances, and thicknesses over the five measured points on the sample.

	Average	Standard Deviation
PL-FWHM (nm)	15.4	1.8
Transmittance (%)	83.61	3.878
Thickness (nm)	483.40	36.620

2.5 Summary

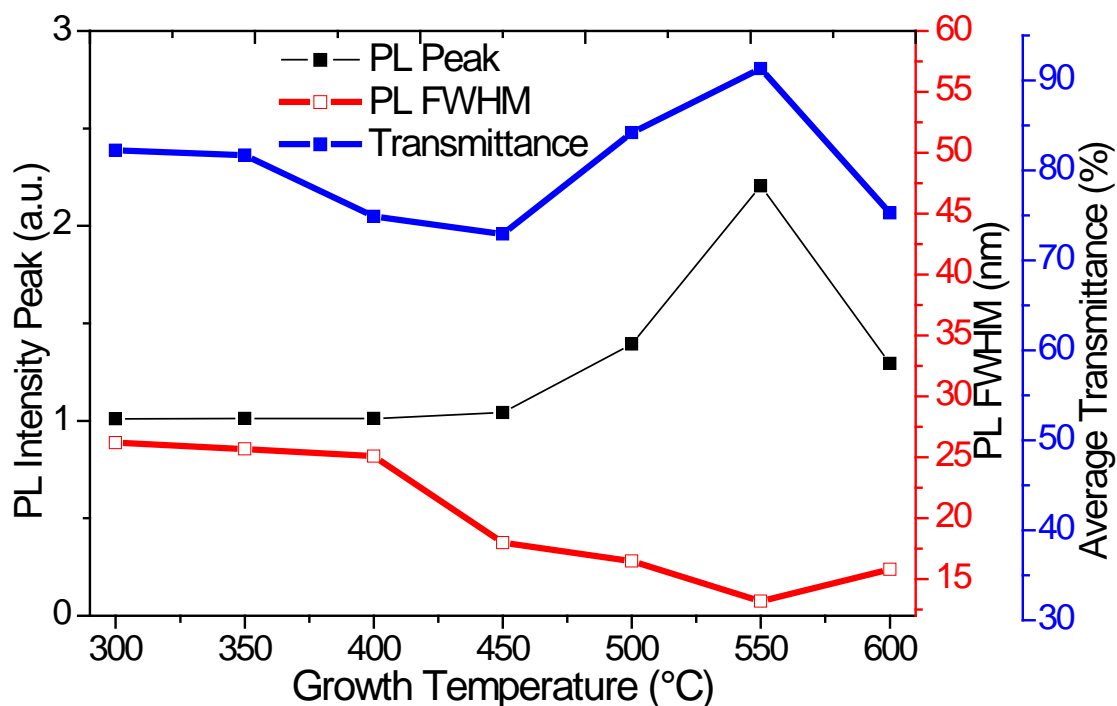


Fig. 2.12. Change in PL peak intensity, PL-FWHM, and average transmittance over the whole spectrum of ZnO films with varying growth temperature. The PL intensity graph is elevated (offset) by 40% of the maximum value for clarity.

This chapter covered the details of ZnO thin film growth using MOCVD, characterization, and optimization of parameters. After analyses of spectral reflectance, transmission, and PL, it was concluded that ZnO thin films grown at substrate temperature of 550 °C demonstrate best crystal quality. A figure of merit was defined in form of a mathematical equation to calculate quality of sample utilizing data from thickness, transmission, and PL measurements. Spatial analysis was also carried out to evaluate

thickness uniformity over the surface of sample and also the optical properties were characterized at different locations on the sample. Figure 2.12 displays summary of the experimental results to optimize ZnO growth temperature. Next chapter presents ZnO growth and characterization using sputtering and its comparison with samples produced by MOCVD.

CHAPTER 3: ZINC OXIDE GROWTH BY SPUTTERING AND CHARACTERIZATION

3.1 Introduction

The material quality plays vital role in performance of the finally fabricated device. Therefore, it is useful to grow material using more than one techniques and characterize for comparison. The MOCVD system used in this study (explained in Chapter 2) is custom made, therefore it produced ZnO films having significant variation in thickness over the surface of a sample. Therefore, ZnO thin films were grown on sapphire substrates using RF magnetron sputtering as well, and structural and optical characterization was carried out by x-ray diffraction (XRD), scanning electron microscopy (SEM), atomic force microscopy (AFM), photoluminescence, transmission, and interferometric spectral reflectance measurements. The ZnO films were grown on textured Si substrates as well to realize the n-ZnO/p-Si SHJSC structure. The deposition parameters of ZnO were optimized. The XRD and SEM confirm that optimized deposition temperature and RF power are $>300\text{ }^{\circ}\text{C}$ and 180 W respectively. The films grown on textured silicon substrates have lower crystallinity as compared to those grown on sapphire [82]. Surface of the film is spatially analyzed and a comparison is established with the previously reported results of MOCVD grown ZnO films. Results show that ZnO films prepared by sputtering technique are superior in thickness uniformity for practical applications. Optical quality of the films prepared by sputtering is similar or even shows better quality compared to MOCVD films probably because the MOCVD system we used, was not a well calibrated

commercial system. Further, the importance of film thickness uniformity in particular with reference to the solar cell performance is discussed. There are several studies reporting sample-to-sample analysis of ZnO films prepared by sputtering for thickness uniformity and reproducibility. However, to the best of our knowledge, in literature no one has reported a study describing thickness uniformity over the surface of ZnO film prepared by sputtering and to have a comparison with the samples prepared by MOCVD which is important for device performance.

3.2 ZnO Deposition by RF Magnetron Sputtering

Several samples of ZnO were grown on sapphire (2" diameter) and textured-Si (1×1 cm²) substrates using sputtering system by AJA International Inc. The films grown on sapphire (transparent) substrates were used for optical characterization and comparison of structural quality. The substrates were cleaned with acetone (using ultrasonic cleaner), methanol, isopropanol and deionized water, and then dried with compressed nitrogen prior to ZnO growth. The sputtering was carried out at a pressure of 3×10^{-3} torr in argon gas environment. The susceptor rotation speed was 20 rpm. The deposition temperature was varied from room temperature to 300 °C for different samples. The RF power was also varied from 130 W to 200 W with a step size of 10 W to find the optimized value.

3.3 Structural Characterization of ZnO

3.3.1 XRD

The XRD of the ZnO samples grown on sapphire and textured-Si substrates was carried out by PANalytical X-ray diffractometer. Figure 3.1 shows 2θ XRD scans of the ZnO samples grown with different RF powers on sapphire substrates. Smaller steps of RF power were used (10 W) to figure out the optimized RF power for best crystal quality. The highest

peak intensity and lowest full width at half maximum (FWHM) were observed for samples grown at 180 W. The XRD scans of the samples grown on textured-Si substrates revealed same trend (not shown here) with comparatively larger FWHM. The grain size of 40–50 nm was calculated using measured value of FWHM of XRD 2θ scan in Debye-Scherrer equation:

$$\tau = \frac{K\lambda}{\beta \cos \theta} \quad (3.1)$$

where τ is the mean size of the crystal grain, K is a dimensionless shape factor having value normally close to 1, λ is the x-ray wavelength which is 1.5418 Å in our case, β is the FWHM of the XRD curve-plot, and θ is the Bragg angle which is $\sim 34^\circ$ (for ZnO) in our case. The calculated grain size is a lower limit on the grain size value because the Debye-Scherrer equation assumes that the contribution in peak broadening from other sources such as dislocations, stacking faults, microstresses, and grain/subgrain boundaries are zero [92].

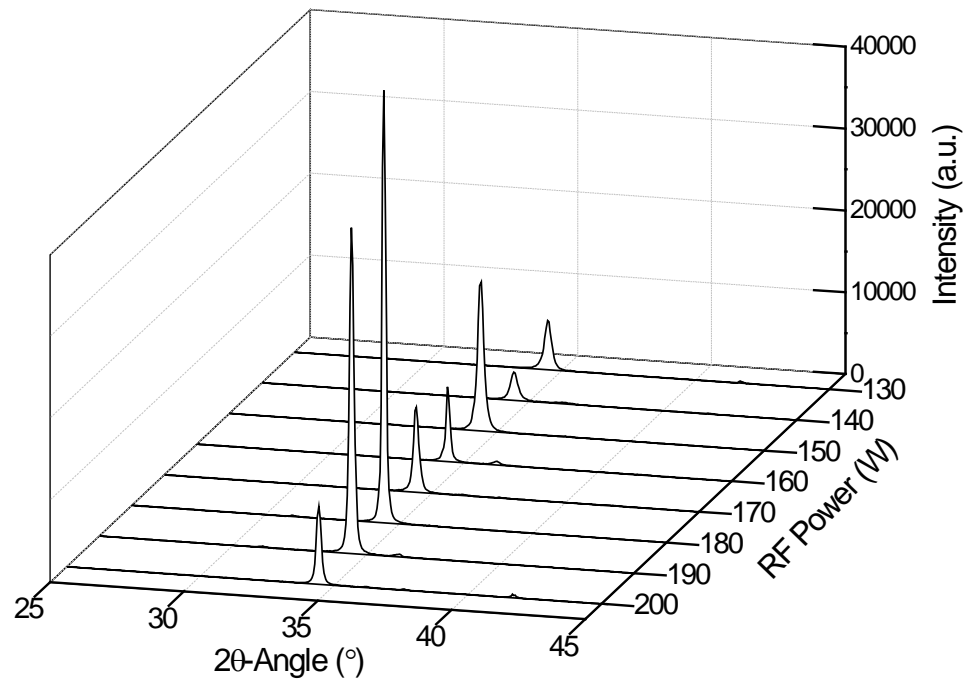


Fig. 3.1. XRD scans showing 002 reflections of the ZnO samples deposited with different RF powers from 130 to 200 W.

Figure 3.2 depicts 2θ XRD scans of the ZnO samples grown at different temperatures. The crystal growth was highly c-axis oriented. The crystal quality monotonically improved by increasing temperature up to 300 °C which proves that it is possible to grow ZnO films with even better crystallinity at higher deposition temperatures; however, the facility available in our cleanroom at UNC-Charlotte has an upper temperature limit of 300 °C.

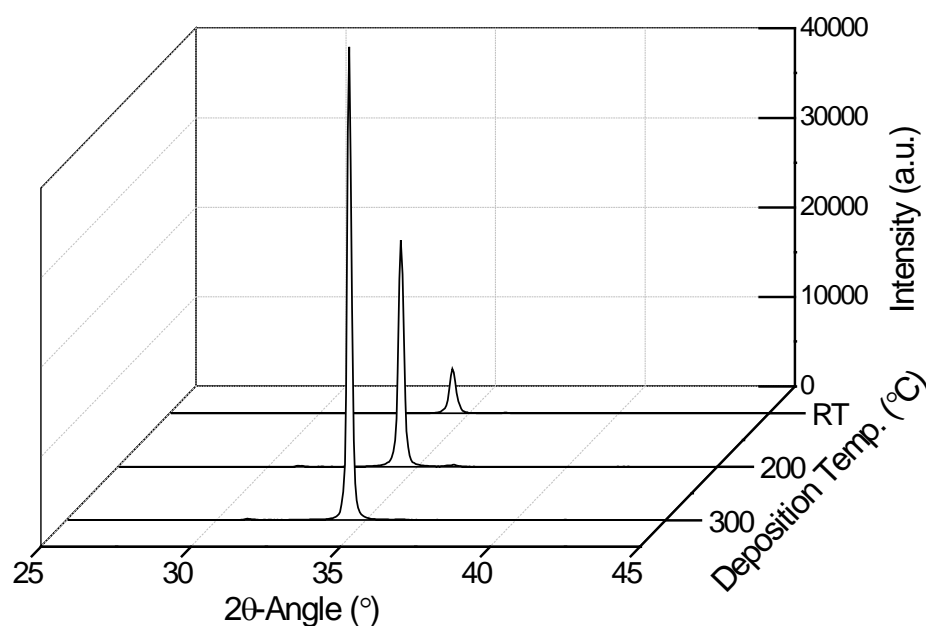


Fig. 3.2. XRD scans showing 002 reflections of the ZnO samples deposited at room temperature (RT), 200 °C, and 300 °C.

3.3.2 SEM

The SEM was performed on ZnO samples grown on sapphire and textured p-Si substrates using JEOL USA SEM tool. The SEM images of samples grown at sapphire substrates at four different temperatures are illustrated in Fig. 3.3. The surface roughness reduced and crystal quality improved with increase in growth temperature. These trends are consistent with results reported by Wang et al. except they got different optimal temperature point probably because they used different technique for ZnO growth [49].

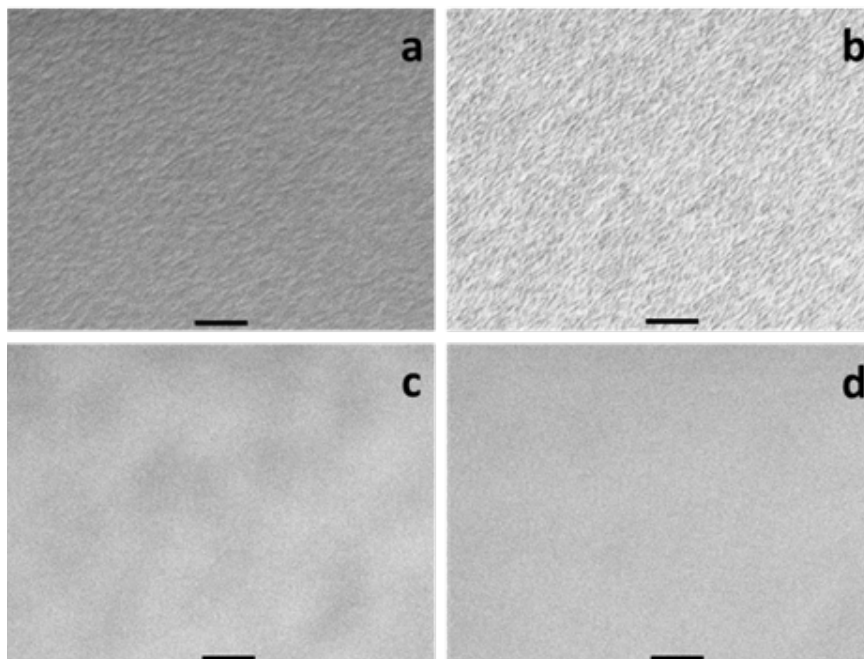


Fig. 3.3. SEM images of ZnO deposited at (a) RT (b) 100 °C (c) 200 °C (d) 300 °C. The scale bar is 2 μm in each figure.

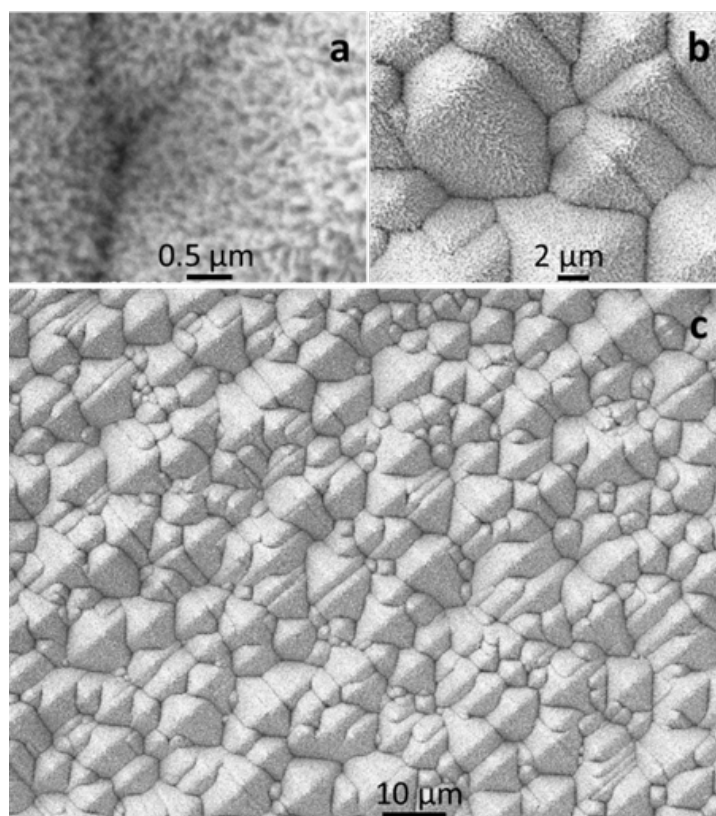


Fig. 3.4. SEM images of n-ZnO grown on textured p-Si at 300 °C with RF power of 180 W.

The SEM images of n-ZnO films grown on textured p-Si substrates are shown in Fig. 3.4. These samples were prepared using optimized parameters. But the surface roughness and crystal quality degraded in case of textured Si substrate as depicted in Fig. 3.4(b).

One of reasons is larger lattice mismatch between Si and ZnO. Another possible reason of degradation in crystal quality is textured surface of the substrate causing uneven crystal growth orientation. There are few reports related to thick ZnO films deposition on textured-Si but not enough data is available about ZnO thin film grown on textured Si substrates. Therefore, more experimental study is required to understand the degradation in crystal quality of ZnO grown on textured-Si.

3.3.3 AFM

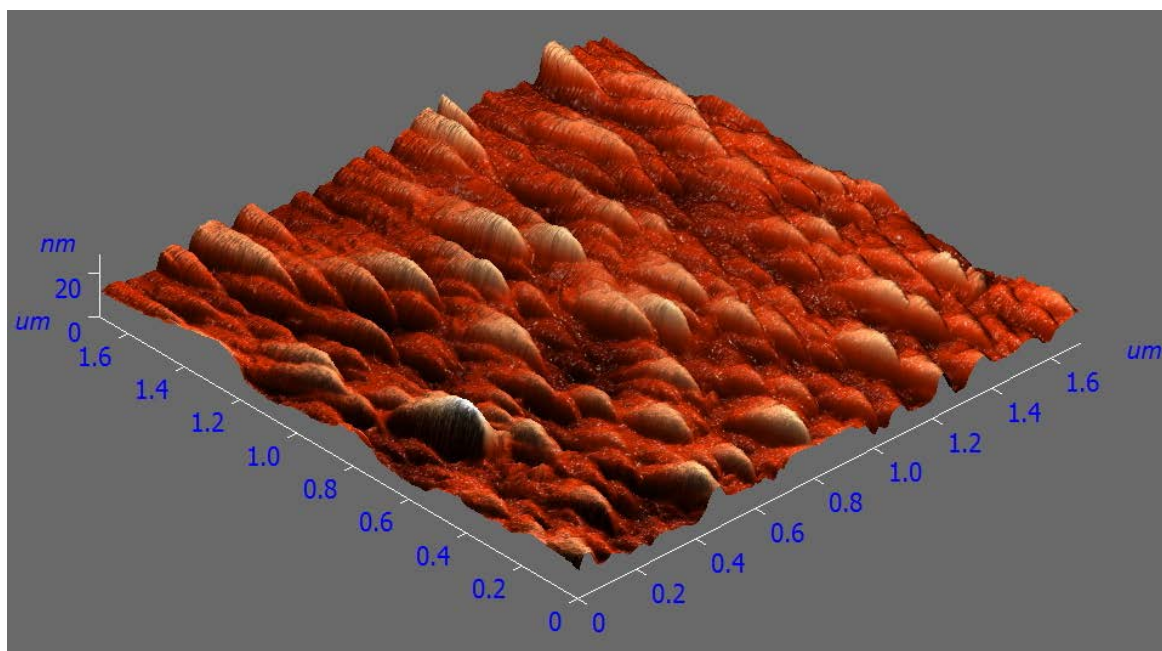


Fig. 3.5. AFM image of n-ZnO grown on sapphire substrate using magnetron sputtering at 300 °C with RF power of 180 W.

TABLE 3.1. Summary of results obtained by image analysis of AFM images

	Size (μm)	Diameter (μm)
Average	0.100	0.113
Standard Deviation	0.036	0.041

The Fig. 3.5 depicts AFM image of ZnO thin film sputtered on sapphire substrate at a temperature of 300 °C and RF power of 180 W. The AFM measurement was carried out by NT-MDT AFM system by Spectrum Instruments and image data was processed and analyzed using the image analysis software provided by the same company. The table 2.1 shows summary of the results. The average grain size is ~100 nm which is consistent with the value calculated by Debye-Scherrer equation using XRD data.

3.4 Spatial Analysis of Sputtered ZnO Thin Films

3.4.1 Thickness Measurements by Spectral Reflectance

The thickness measurements were carried out by utilizing the Filmetrics F20-UV system that exploits spectral reflectance data to calculate thickness, optical constants, and roughness of the sample. The measurements performed at nine distinct points are plotted on a 3-D histogram as illustrated in Fig. 3.6.

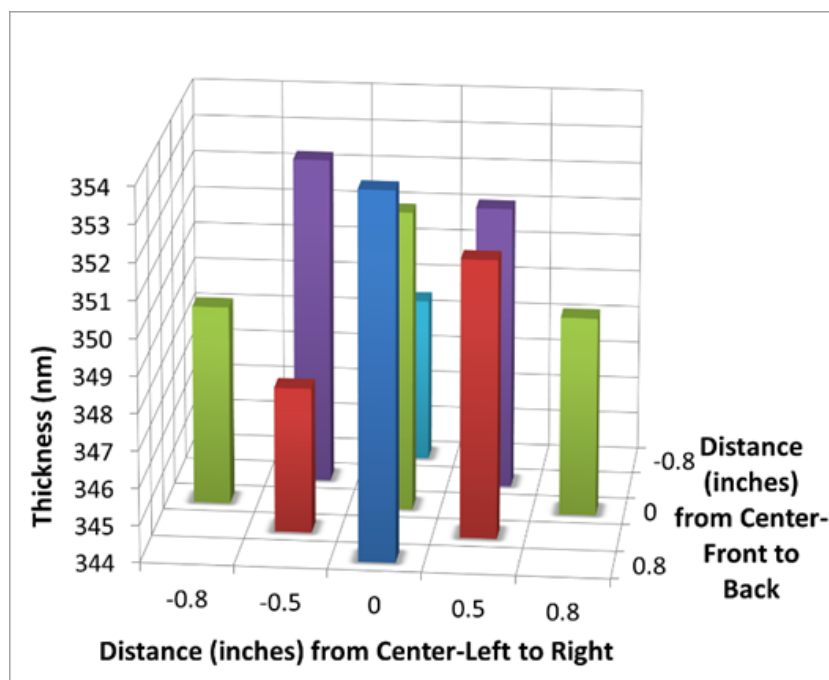


Fig. 3.6. Thickness measurements using spectral reflectance data at nine distinct points over the surface of ZnO thin film sputtered on sapphire substrate of diameter of 2 inches. The inset of Fig. 3 depicts the positions front, back, left, and right.

TABLE 3.2. Comparison of thickness uniformity over the surface of ZnO samples grown by sputtering and MOCVD.

Growth Method	Growth Temperature (°C)	Average Thickness (nm)	Standard Deviation (nm)
Sputtering	300	350.8	2.1
MOCVD	550	483.4	36.6

Overall, the thickness for the ZnO sample grown with sputtering technique is highly uniform. The mean value of thickness is 350.8 nm with a standard deviation of 2.1 nm and thicknesses over the surface are in the range of 347.9 to 353.9 nm. As mentioned in chapter 2, the samples grown by MOCVD had thickness measurements varied over a range of ~70 nm. Table 3.2 shows the average thicknesses and standard deviations for the ZnO samples grown by sputtering and MOCVD. Generally, it is well known that overall quality of thin films prepared by MOCVD is better than sputtering. The improved thickness uniformity for sputtered samples in our case might be due to the fact that the homemade MOCVD system we used was not a commercial quality system.

3.4.2 Photoluminescence

Fig. 3.7 (a) depicts the PL spectra at five different points of a sputtered ZnO thin film on a sapphire substrate. PL spectra show the usual emission occurs at an averaged peak wavelength of 380.2 nm that corresponds to a bandgap value of 3.261 eV. The PL intensity for the sputtered sample at 300 °C is higher compared to the previously reported samples grown by the homemade MOCVD system even at higher temperature (450 °C) [83]. The higher PL intensity represents better crystal quality of the film. The standard deviation between the peaks at different locations on the ZnO sample prepared by RF sputtering was found to be 1.5 nm. The average full width at half maximum (FWHM) was found to be 14.5 nm (or 0.125 eV). The standard deviation of the FWHM for the ZnO sample was

found to be 0.4 nm. The Table 3.3 shows the average FWHM for ZnO samples grown by sputtering and MOCVD as well as the standard deviation between the different measurement points. The lower value of FWHM relates to the higher crystal quality.

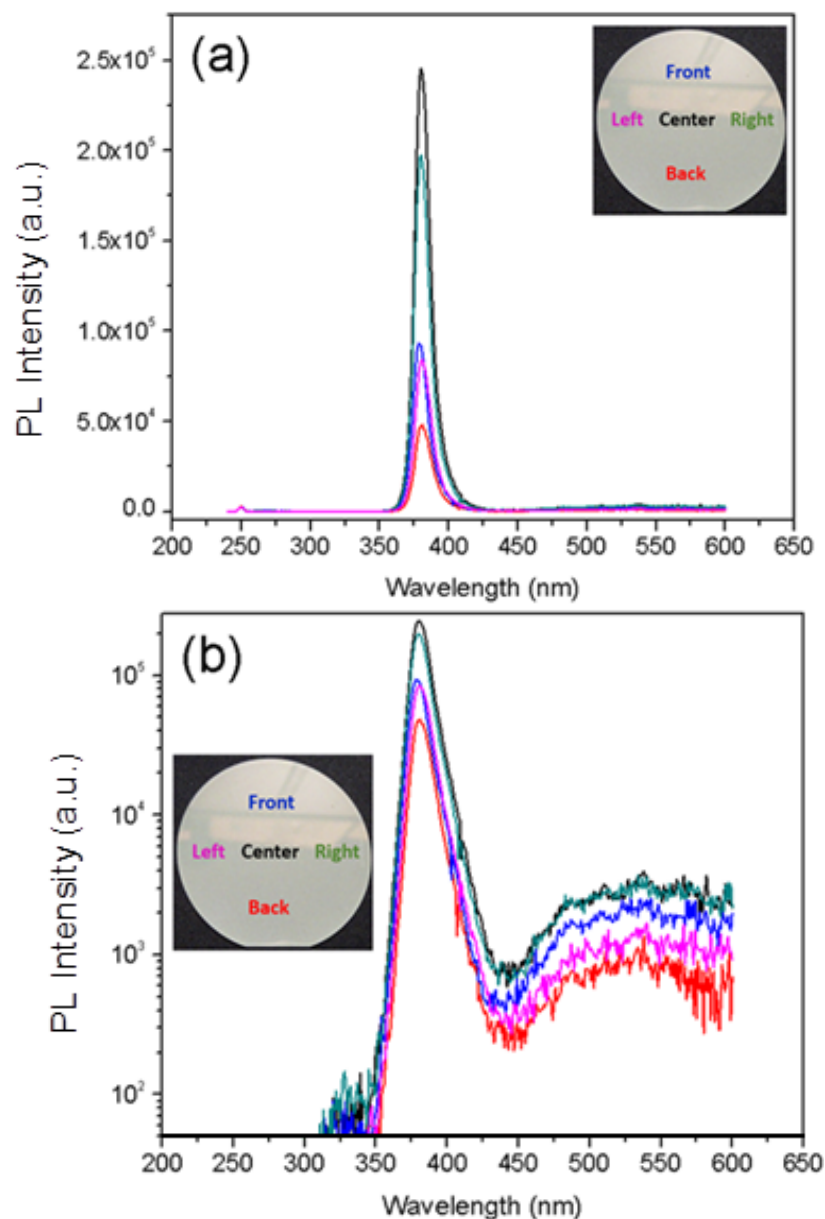


Fig. 3.7. Photoluminescence measurements taken at five different spatial points over the surface of ZnO thin films sputtered on sapphire substrate (a) linear scale (b) logarithmic scale.

TABLE 3.3. Comparison of PL-FWHM of ZnO samples grown by sputtering and MOCVD.

Growth Method	Growth Temperature (°C)	Average FWHM (nm)	Standard Deviation (nm)
Sputtering	300	14.53	0.44
MOCVD	550	15.40	1.80

Fig. 3.7 (b) shows the same PL spectra in logarithmic scale for analysis of low intensity signals. The weak green emission at 500 nm spanning up to 600 nm, known as deep-level emission, is caused by impurities such as oxygen vacancies and/or zinc interstitials. These defects and resulting deep level emission can be reduced by annealing samples in oxygen at 1200 °C [93].

3.4.3 Transmittance

ZnO, being a wide bandgap material has a number of potential applications where transparency of the film plays critical role; such as use transparent conducting oxides as transparent electrodes in liquid crystal displays [94], antireflection coating [95], and n-layer of ZnO/Si heterojunction solar cell [80]. Transmittance was measured in the same manner as for PL analysis at five different points of the sample using the same Filmetrics F-20 UV setup we used for thickness measurements. The halogen and deuterium lamps both were selected as the light sources to cover the entire wavelength range from deep-UV spanning into infrared.

The transmittance spectra for ZnO sample deposited at 300 °C are shown in Fig. 3.8. The value of bandgap obtained from transmittance data is consistent with the value obtained by PL measurements. The average transmittance recorded in the wavelengths ranging from 200 to 900 nm is about 80% which is the same as obtained for the samples grown at 300 °C by MOCVD [83]. The transmittance is expected to further enhance if the

substrate temperature is raised above 300 °C during sputtering because the crystallinity will improve as evident by Fig. 3.2.

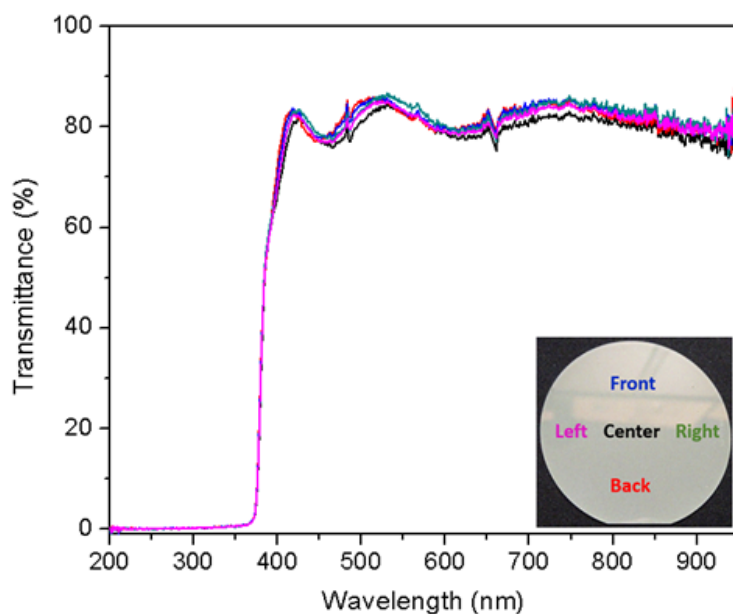


Fig. 4. Transmission measurements at five different points of the ZnO thin films sputtered on sapphire substrate.

3.4.4 Discussion on Spatial Analysis

Thickness uniformity of the film is an important parameter because thickness directly affects physical properties of the single- or multi-layer structure and thus performance of the device [96] [97]. Also, it plays important role in sample evaluation especially in electrical characterizations like Hall and 4-probe measurements because thickness is a key factor which is used to calculate carrier concentration, lifetime, resistivity, and mobility of the sample.

The thickness uniformity of the film prepared by magnetron sputtering is primarily dictated by the geometry of the target relative to substrate, applied electric power, gas temperature, and erosion zone of the target ends. The thickness uniformity and deposition rate both increase with the decrease in target-substrate distance as well as with increase in

power [98]. Jiang et al. have recently proposed a theoretical model to improve uniformity in thickness of the films grown on a large substrate by employing a step-moving target [99]. There were two critical parameters, the target stay time and the target moving step, that affect film thickness distribution in the model.

We have experimentally observed that uniformity in thickness distribution over the surface of ZnO films prepared by sputtering is better than the films produced by the available MOCVD system. The PL measurements revealed that crystal quality of the films sputtered at 300 °C is better than the films grown by MOCVD even grown at higher temperature on same substrate material. The high temperature processing of samples can degrade the quality of substrate and thus performance of the device. This is specifically applicable to ZnO/Si heterojunction solar cell because high temperature causes solar cell performance degradation mainly correlated with oxygen precipitation [100]. Also, there is a direct relation between spatial thickness uniformity and solar cell performance. The behavior of absorption of light has been linked to normalized standard deviation of thickness [101]. Karpov et al. in 2002, modeled non-uniformity effects in terms of the equivalent circuit of a system of many interacting random diodes [102]. The several weak diodes were associated with a non-uniform thickness which consumed most of the photogenerated current. The non-uniform thickness was believed to influence the optical and electrical properties of thin films.

There are some additional advantages associated with sputtering as compared to MOCVD. It is possible to implement shadow-mask lithography in sputtering if ZnO (or any other material) needs to be deposited on selected areas. Also, source vapors can

penetrate below the substrate in case of MOCVD causing unwanted growth of material on the back side of substrate where this is not possible in sputtering.

3.5 Summary

This chapter presented deposition of ZnO using RF magnetron sputtering and structural characterization using XRD, SEM, and AFM. Detailed optical characterization was also performed by PL, transmission, and spectral reflectance measurements. The growth temperature and RF power for ZnO crystal quality were optimized by iterative experiments. Also, spatial thickness uniformity and optical quality were evaluated and compared with the ZnO samples prepared by the available MOCVD system in our Lab. The results confirmed that the ZnO thin films produced by magnetron sputtering are more uniform in spatial thickness distribution as compared to ZnO thin films grown on the same substrate by MOCVD. Based on our analysis, overall sputtered ZnO films exhibited better and an improved optical quality over the MOCVD films. These experimental findings helped us to select sputtering method for growth of ZnO to fabricate the solar cell.

CHAPTER 4: n-ZnO/p-Si HETEROJUNCTION SOLAR CELL MODELING AND SIMULATIONS

4.1 Introduction

This chapter presents modeling and simulations of potentially cost effective and high efficiency single heterojunction solar cells based on Si (rear region) and the II-VI material ZnO (front region). The simulations were performed using modified personal-computer-one-dimensional (PC1D) software taking practical constraints into account. Electrical and optical characteristics as well as internal and external quantum efficiencies were investigated by varying different key parameters. The measured absorption spectrum of the ZnO thin films grown in our Lab was used in PC1D simulations in order to get more realistic results of the model. The best conversion efficiency has been predicted as 19.0% with fill factor of 81%.

The ZnO grown on Si can work as an active n-layer as well as antireflection (AR) coating due to its close refractive index match with the ideal value. This prevents requirement of additional AR coating which can reduce fabrication cost and complexity. ZnO can be deposited at much lower temperature that can reduce degradation in carrier lifetime, a common problem in high temperature diffusion of phosphorous and ion implantation in the conventional Si pn junction solar cell. Furthermore, the work function of Ag (4.2 eV) is less than the electron affinity of ZnO (4.5 eV). Consequently, there is no barrier at Ag-ZnO interface and the contact at front surface will be ohmic which can further increase the device performance. Additionally, as compared to ITO which is commonly

used as AR coating, ZnO is more resistant to radiation damage because of its stable crystal structure which inhibits UV degradation and ensures longevity of the device.

Previously, various studies have been presented using texture-etched ZnO-coated glass substrates [103] [104] [105] or ZnO nanostructured transparent electrodes for high conversion efficiency solar cells [106] [107] [108] [109]. In this proposed model, front region of the solar cell which is directly exposed to solar radiation is composed of n-type ZnO. Therefore, transparency of the ZnO layer for visible and IR region is very important. In 2009, Nayak et al. [36] demonstrated Ga-doped ZnO transparent conducting thin films for optoelectronic device applications using sol-gel spin coating technique. The transparency of the films was more than 80% in the spectral range of 400 – 700 nm with resistivity as low as $3.3 \times 10^{-3} \Omega\text{cm}$ with 2 at% Ga. Contemporarily, Huang et al. [37] and Zhao et al. [38] reported highly transparent Ga doped ZnO thin films with low resistivity using MOCVD. Huang et al. achieved highest transparency of 85% in the same spectral range, mobility of $30.4 \text{ cm}^2\text{V}^{-1}\text{s}^{-1}$, and lowest resistivity of $3.6 \times 10^{-4} \Omega\text{cm}$.

4.2 Schematic and Modeling of n-ZnO/p-Si Solar Cell

Figure 4.1 illustrates schematic of the solar cell model proposed in this study. Thicknesses of the rear and front regions are optimized by PC1D simulations (explained in next section). The peak intensity of the solar spectrum is approximately at wavelength of 600 nm. The reflectivity (R) at this wavelength calculated by PC1D (personal computer 1-dimensional) semiconductor modeling program was 33% that is close to average value of ~37% for wavelengths 400-1100 given in literature [110]. The refractive index (n) of ZnO at the same wavelength was calculated using Fresnel equation for normal incidence in

which extinction coefficient is ignored due to negligible absorption. The reflectance is related to refractive index in this equation:

$$R = \left(\frac{n - 1}{n + 1} \right)^2. \quad (4.1)$$

The refractive index of air is assumed to be 1. Using simple algebraic manipulations, the refractive index can be found as

$$n = \frac{r + \sqrt{r^2 - 4}}{2} \quad (4.2)$$

where $r = 2(I+R)/(I-R)$. The refractive index of silicon at wavelength of 600 nm came out to be 3.95. The reflection is minimized if the refractive index of the AR coating (ZnO layer in our case) is the geometrical mean of the two surrounding indices. Assuming air at one side and Si at other side, optimum refractive index (n_{AR}) of the AR coating is

$$n_{AR} = \sqrt{n_{air} \times n}. \quad (4.3)$$

Assuming air index as 1, optimum value of refractive index of AR coating should be 1.99 at wavelength having peak intensity. The refractive index of ZnO at 600 nm is ≈ 2 which is very close to the ideal value. Required thickness of ZnO layer to act as perfect AR coating can be calculated as

$$d = \frac{\lambda}{4n_{AR}}. \quad (4.4)$$

The optimum thickness of the ZnO layer is 75 nm for $\lambda = 600$ nm. But PC1D simulations revealed that conversion efficiency does not change significantly up to 100 nm thickness of ZnO layer (the dependence is rather weak).

The optimized modeled thickness of ~ 0.1 μm for minimum reflection can be detrimental to electrical performance of the device because the sheet resistance of the ZnO film can be very high and will require very close gridline spacing resulting in increased

shadowing. Increased shadowing decreases the short circuit current and hence the efficiency. To improve the sheet resistance, thicker ZnO films can be used that will still significantly reduce reflection (especially if textured Si is used) as compared to bare silicon. The simulations revealed that increasing ZnO film thickness from 0.1 to 0.5 μm reduces the efficiency from 19.4% to 19%. This drop in efficiency is not significant as compared to losses due to high sheet resistance and shadowing effects because of close gridline spacing. Since absorption coefficient of ZnO above bandgap is on the order of 10^5 cm^{-1} , the absorption length is around 100 nm. Therefore, most of the UV portion of solar radiation would be absorbed in $>100 \text{ nm}$ thick ZnO layer. The electron affinity of ZnO is 4.5 eV where the work function of Ag is 4.2 eV. Therefore, there is no Schottky barrier at the interface and the Ag-ZnO contact at the front surface is ohmic which further enhances the device performance. The electron affinity of ITO, commonly used as AR coating for solar cells, is $\sim 4.7 \text{ eV}$ [111].

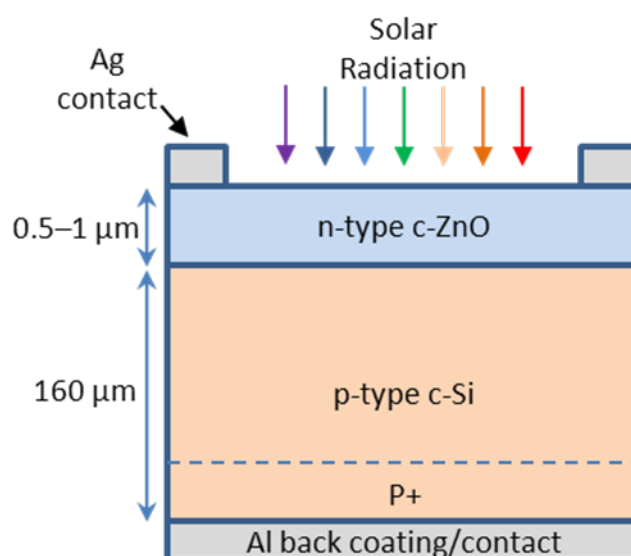


Fig. 4.1. Schematic showing single heterojunction solar cell based on crystalline n-ZnO and p-Si.

4.3 Simulations

4.3.1 PC1D Software

A large amount of time, effort, and resources can be saved if simulations are effectively incorporated in employing appropriate theoretical models in device designs. In the PV community, PC1D is the most popular software package to simulate optical and electrical behavior of the solar cell devices. This software was originally developed in 1980's by Paul Basore's group at the Iowa State University. Additional features including light trapping-model were introduced in PC1D by Paul Basore at Sandia National Labs [112]. The software was converted for use with windows in 1990's at University of New South Wales. The software has been continuously improved alongside progress in experimental work and theoretical models [113]. Over the decades, this software has played an important role in improvement of existing devices and development of new ones. The main features of PC1D are its free availability, precision, speed, convenience, and open source code. The program numerically solves the coupled nonlinear equations for carrier generation, recombination and transport of electrons and holes in crystalline semiconductor devices. It can be used for device performance simulation as well as to understand the fundamental physical phenomena of solar cells. A few researchers have reported modifications in PC1D to make it further user friendly or to employ it for new materials [114]. There are several other reports presenting characterization studies and improvements in Si, GaAs, and other heterostructure solar cells [115] [116] [117].

4.3.2 Quantum Efficiency

There are several adjustable parameters in PC1D which can be altered to find an optimized window for solar cell fabrication. Since we are using ZnO only for the front

region, the parameters associated with the rear region are almost same as already optimized for Al-BSF Si by the solar cells community. We have used absorption spectrum for ZnO which was measured in our lab for film thickness around $0.5 \mu\text{m}$.

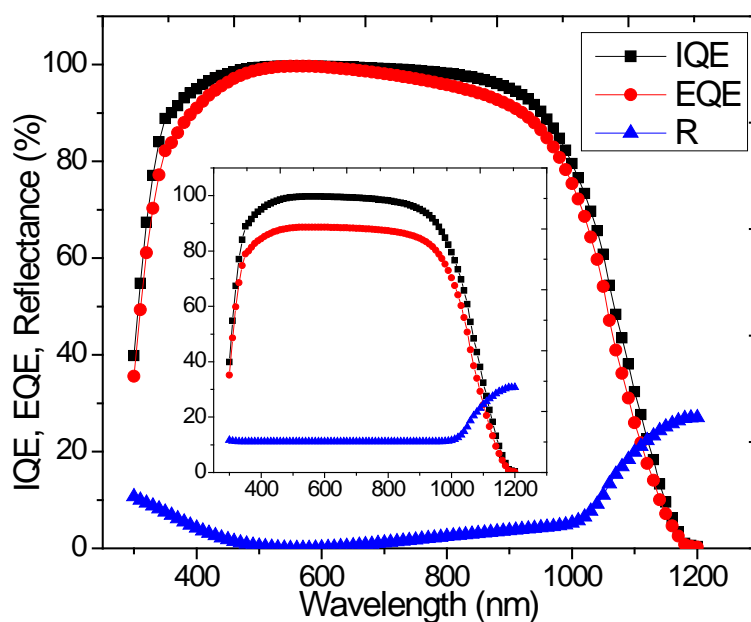


Fig. 4.2. Internal quantum efficiency (IQE), external quantum efficiency (EQE), and front surface reflection (R) of the solar cell device taking into account antireflection effects of the ZnO layer. The inset shows same parameters without antireflection effects.

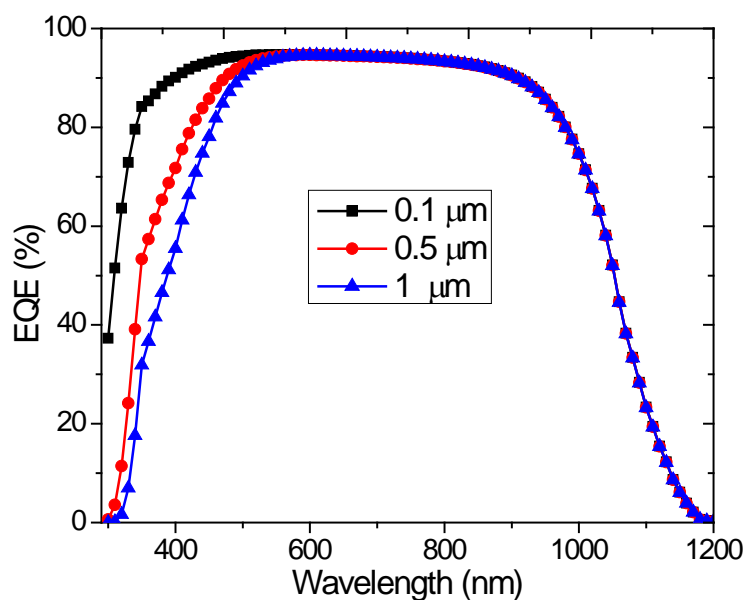


Fig. 4.3. External quantum efficiency (EQE) of the solar cell device for three different thicknesses of ZnO layer assuming 5% reflection from front surface.

Figure 4.2 illustrates internal quantum efficiency (IQE), external quantum efficiency (EQE), and front surface reflection of the solar cell device. The antireflection effects of the ZnO layer were included for this simulation. The reflectance and quantum efficiency without incorporating antireflection in device parameters are depicted in the inset of Fig. 4.2. It is obvious that absorption as well as EQE is significantly improved specially around wavelength of 600 nm (peak of solar spectrum). Without including antireflection effect, the conversion efficiency up to 17.6% with the fill factor around 81% was predicted. Incorporating antireflection effect in the simulation, the best conversion efficiency of 19% and a fill factor of 81.9% were anticipated. Figure 4.3 illustrates the external quantum efficiency (EQE) of the solar cell device for different thicknesses of ZnO layer. The absorption of high energy photons in ZnO is mainly responsible for poor EQE at short wavelengths.

4.3.3 Electrical Parameters and Efficiency

The impact of ZnO thickness on open circuit voltage (V_{OC}), short circuit current (I_{SC}), fill factor, and power conversion efficiency of the ZnO/Si solar cell are depicted in Fig. 4.4. The I_{SC} reduces monotonically with increased ZnO thickness because of significant decrease in number of available short-wavelength photons in space charge region as shown in Fig. 4.3. Since most of the space charge region lays in Si due to the large difference in doping levels in two materials, the photons reaching Si contribute most in carrier generation. Since I_{SC} is directly related to photo-generated carriers, absorption in thicker ZnO layer causes drop in I_{SC} . A slight decrease in V_{OC} with increase in ZnO thickness can be attributed to the same reason. For the optimized solar cell in terms of efficiency, we achieved a V_{OC} of 622 mV which is slightly lower than that of conventional Si based solar

cells (~630 mV). This is mainly due to the high surface recombination velocity posed by the hetero-junction of silicon and ZnO. This can also be explained by a Fermi level pinning phenomenon which is a strong function of the interface recombination velocity. A high interface recombination velocity in this model is inevitable due to the hetero-interface between Si and ZnO. The fill factor of the solar cell improves with increasing ZnO thickness as depicted in Fig. 4.4 (b). This is caused by decrease in the series resistance of the solar cell which is a dominant parameter effecting fill factor.

The optimum thickness computed by PC1D is around 0.1 μm which has sheet resistance of $\sim 500 \Omega/\text{sq}$. Such a high sheet resistance requires narrow finger spacing for the solar cell. Therefore, we recommend using thicker layer ($\sim 0.5 \mu\text{m}$) that will allow wider finger spacing and reduction in shadowing effect. Apparently, it seems that efficiency should largely reduce due to decrease in EQE (Fig. 4.3) if ZnO thickness is increased from 0.1 μm to 0.5 μm . But due to less contribution of energy in the solar spectrum at shorter wavelengths, efficiency does not reduce as significantly as it does in case of narrow finger spacing.

The effect of minority carrier life time on the solar cell efficiency is shown in Fig. 4.5. The collection probability of the solar cell chiefly depends on the carrier life time (or diffusion length) and strongly effects short circuit current of the solar cell. Front surface recombination velocity of Si (or ZnO/Si interface recombination velocity) is the most important parameter in this model that dictates efficiency of the solar cell. Figure 4.6 illustrates large effect of the interface recombination velocity on the solar cell performance. We have used interface recombination velocity of 10^6 cm/s in the simulations. The maximum achieved short circuit current, open circuit voltage, fill factor, and efficiency are

37.7 mA/cm², 0.622 V, 81%, and 19.0%, respectively. These results are very promising at this initial stage. The practical constraints are kept in mind using these values in simulations. The efficiency will further enhance if lower recombination velocity value is used as shown in Fig. 4.6.

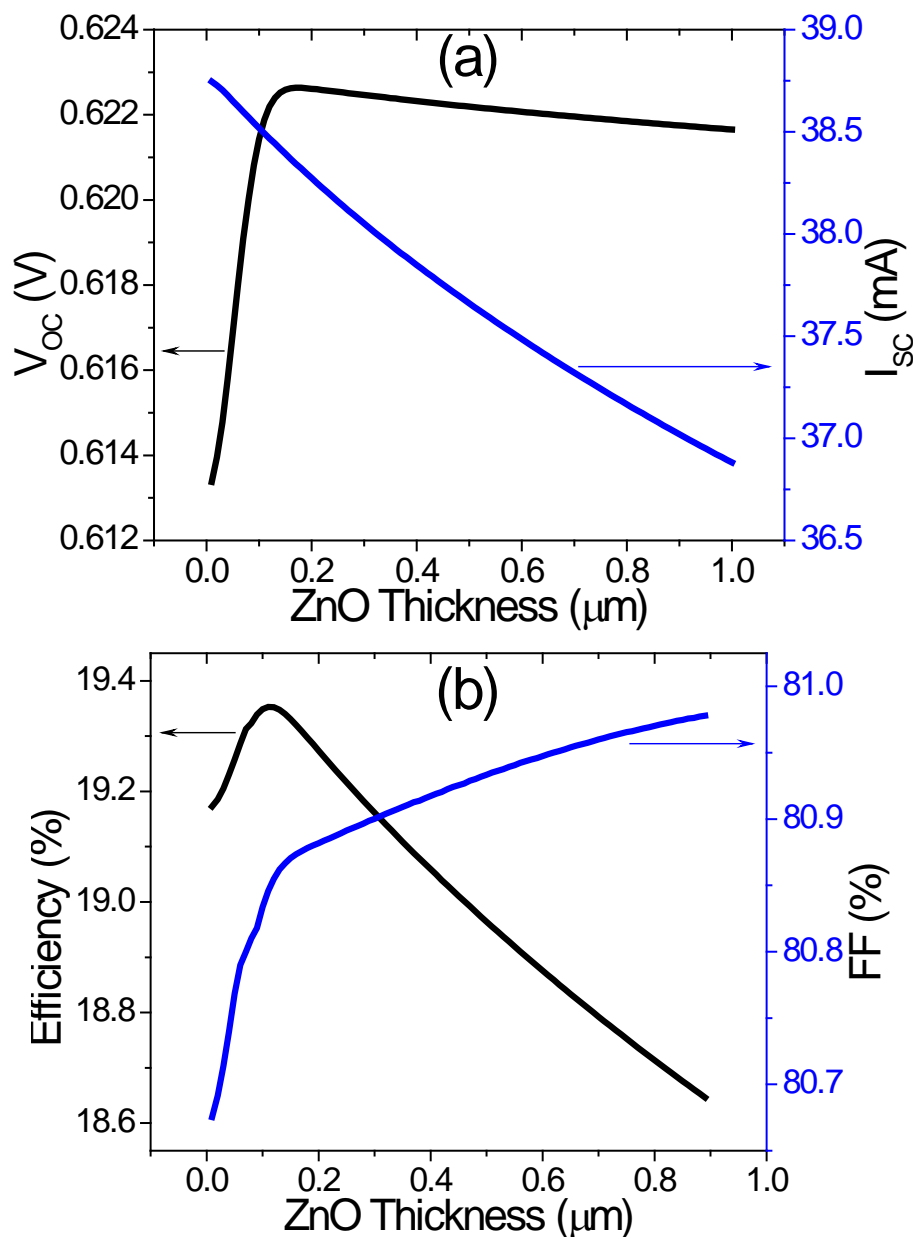


Fig. 4.4. Effect of ZnO thickness on (a) open circuit voltage and short circuit current (b) power conversion efficiency and fill factor of the Si-ZnO single heterojunction solar cell by simulations.

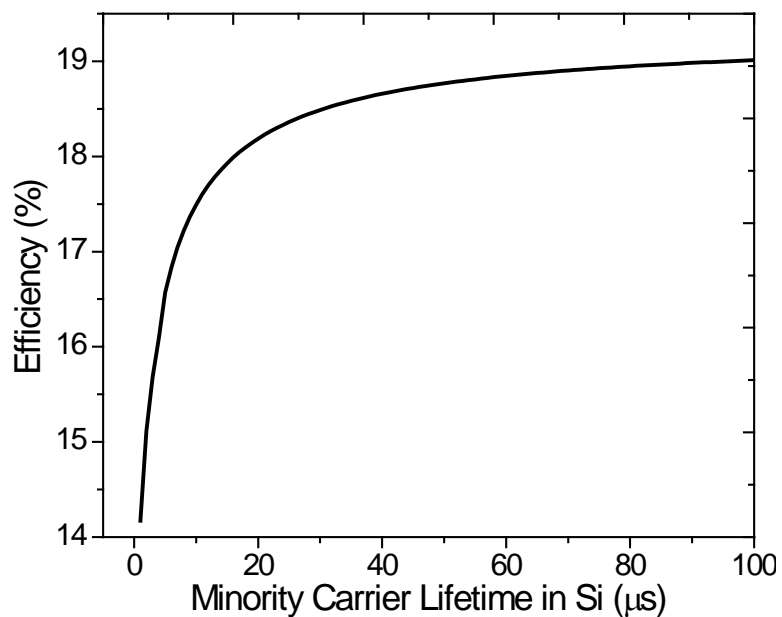


Fig. 4.5. Increase in the solar cell efficiency with increasing minority carrier life time in bulk Si.

The most of results mentioned above have been confirmed (not shown here) by another software Automat FOR Simulation of HETerostructures (AFORS-HET) [118] [119] and the results are consistent with those obtained by PC1D.

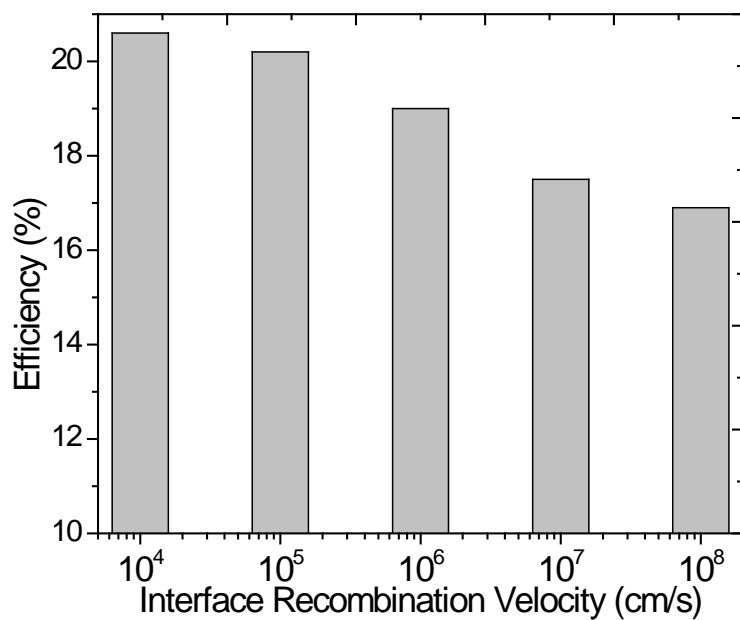


Fig. 4.6. Decrease in the solar cell efficiency with increase in ZnO/Si interface recombination velocity.

4.3.4 Effect of Doping Concentration

The doping concentration in ZnO has significant influence on the fill factor. The fill factor will be reduced significantly for concentrations lower than of order 10^{17} cm^{-3} as represented by Fig. 4.7. Change in ZnO doping concentration does not change I_{SC} and V_{OC} significantly. The doping concentration in Si does not alter fill factor and V_{OC} prominently but it changes I_{SC} significantly as illustrated in Fig. 4.8. It was also noticed that I_{SC} reduces with increasing p-doping concentration in Si. The current-voltage (I-V) and power characteristics of the device are shown in Fig. 4.9 for optimized parameters. The optimized values of the solar cell parameters and best achieved results are shown in Table 4.1.

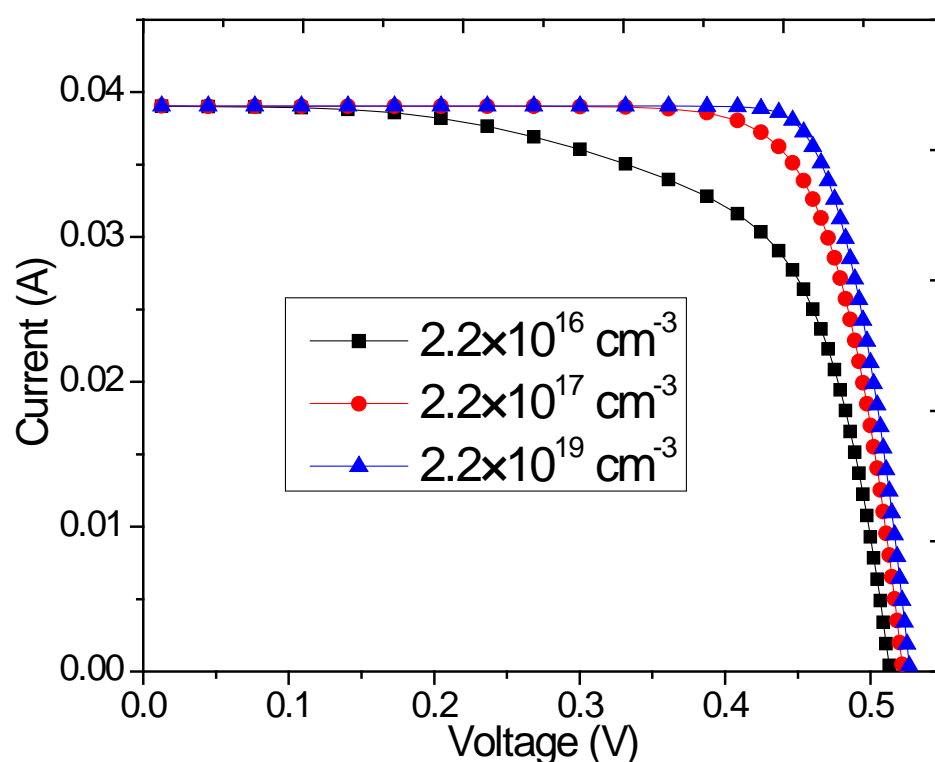


Fig. 4.7. Current voltage characteristics of the solar cell with different doping concentrations in n-ZnO, keeping p-Si doping concentration constant at $1 \times 10^{16} \text{ cm}^{-3}$.

Simulations results presented in this chapter suggest that ZnO can be used with Si to fabricate efficient, durable, and cost effective heterostructure solar cells. A comparison of

the processes involved in fabrication of a conventional Si solar cell and the n-ZnO/p-Si solar cell is presented in Table 4.2. Assuming front reflectance of 5%, PC1D simulations show that the conventional Si cell exhibits an efficiency of 20.8% using the same p-type Si base. The slightly lower efficiency (19%) of the n-ZnO/p-Si cell is due to (1) the non-ideal transmission of ZnO, leading to loss in I_{SC} , and (2) higher recombination velocity at the interface, causing loss in both I_{SC} and V_{OC} . It is important to note that the proposed device does not need p-type doping in ZnO which is a well-known issue with this material. But tremendous amount of research and experimental study is required to understand and overcome the problems associated with recombination at the hetero-interface.

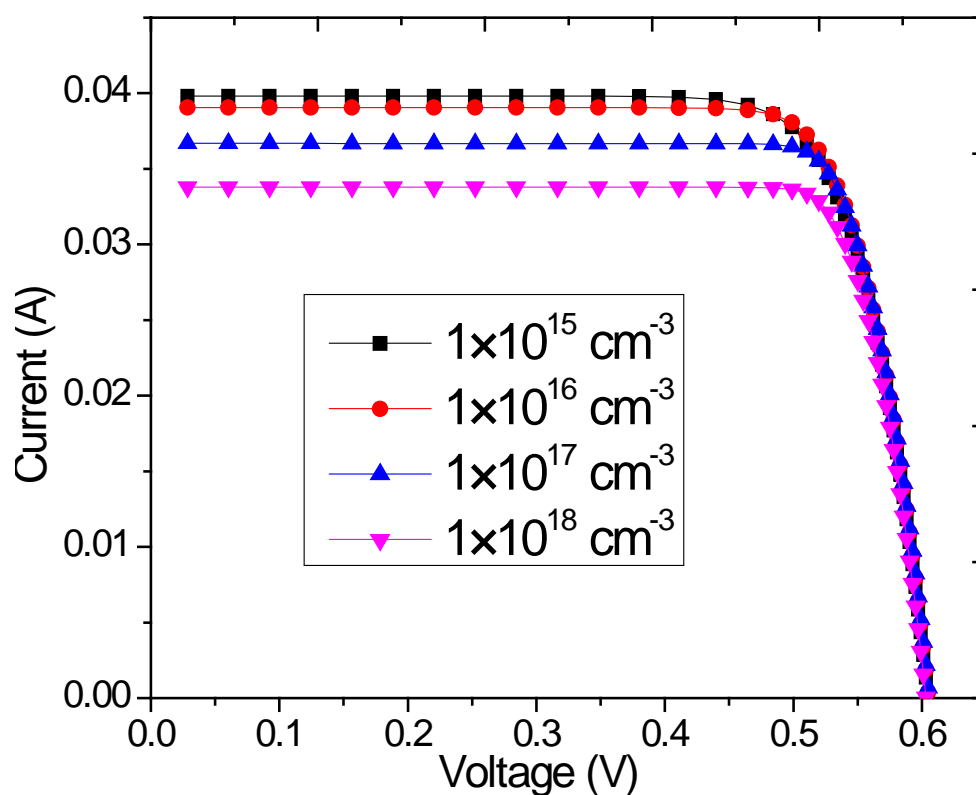


Fig. 4.8. Current voltage characteristics of the solar cell with different doping concentrations in p-Si, keeping n-ZnO doping concentration constant at $2.2 \times 10^{19} \text{ cm}^{-3}$.

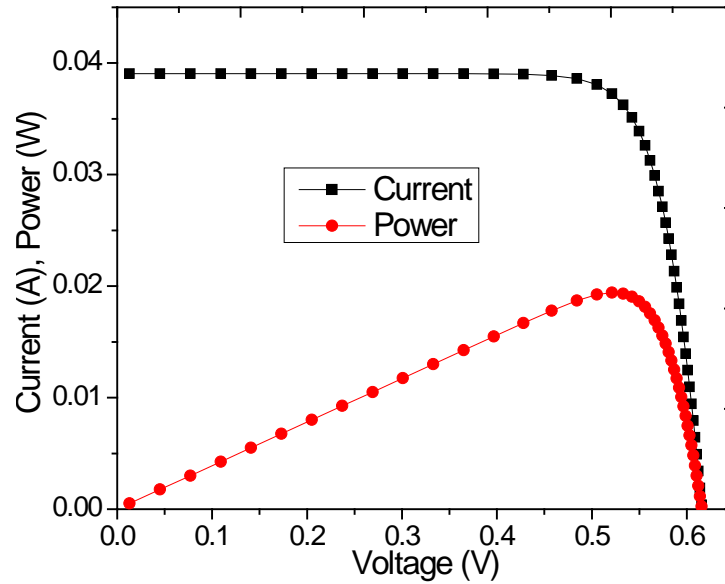


Fig. 4.9. Current, voltage, and power characteristics of the Si-ZnO single heterojunction solar cell with optimized parameters by simulations.

TABLE 4.1. Optimized Parameters for The Solar Cell

Varying Parameter	Value
Device Parameters	
Device Area	1 cm ²
Surface Texturing	None
Surface Charge	None
Front Reflectance (from ZnO)	5%
Internal Rear Reflectance	70%
Emitter Contact Resistance	10 ⁻⁶ Ω
Base Contact Resistance	0.4 Ω
Front Region (ZnO)	
Region Thickness	0.5 μm
Electron/Hole Mobility	50 cm ² /Vs
Dielectric Constant	8.66
Bandgap	3.27 eV
Refractive Index	2
n-type Background Doping	2.2×10 ¹⁹
Bulk Electron/Hole Recombination Time	1×10 ⁻⁶ μs
Electron/Hole Front Surface Recombination Velocity	1×10 ⁷ cm/s
Rear Region (Si)	
Region Thickness	160 μm

Carrier Mobilities	From Internal Model of PC1D
Dielectric Constant	11.9
Bandgap	1.124 eV
Intrinsic Concentration at 300 K	$1 \times 10^{10} \text{ cm}^{-3}$
p-Type Background Doping	$1 \times 10^{16} \text{ cm}^{-3}$
Peak Rear p-Type Doping	$3 \times 10^{18} \text{ cm}^{-3}$
Bulk Electron/Hole Recombination Time	100 μs
Electron/Hole Front Surface Recombination Velocity	$1 \times 10^6 \text{ cm/s}$
Electron/Hole Rear Surface Recombination Velocity	300 cm/s
Results: Short Circuit Current = 37.7 mA Open Circuit Voltage = 0.6221 V Maximum Output Power = 19.0 mW Conversion Efficiency = 19.0% Fill Factor = 81%	

TABLE 4.2. A comparison of the processes involved in fabrication of the conventional and the n-ZnO/p-Si solar cell

Si p-n junction solar cell	ZnO-Si solar cell
Wafer selection	Wafer selection
Saw damage etching	Saw damage etching
Texturing	Texturing
p-n junction formation High temperature (820 – 920 °C)	ZnO growth Low temperature (550 °C)
Edge isolation	Might be needed (depends on growth technique)
SiN deposition	–
Contact formation	Contact formation

4.4 Summary

This chapter included modeling and simulations of n-ZnO/p-Si single heterojunction solar cells. Internal and external quantum efficiencies as well as electrical characterization were simulated using modified PC1D software. Influence of doping concentrations on ZnO

and Si was investigated to find the optimized values of doping concentrations. Furthermore, importance of the n-ZnO/p-Si solar cell structure is highlighted in comparison with the conventional Si pn junction solar cell. The measured absorption spectrum of the ZnO thin films grown in our Lab was used in PC1D simulations in order to get more realistic results of the model. The best values of I_{SC} , V_{OC} , conversion efficiency, and fill factor has been predicted as 37.7 mA, 0.6221 V, 19.0% respectively. The simulation results prove that ZnO can be used with Si to fabricate efficient, durable, and cost effective heterostructure solar cells.

CHAPTER 5: n-ZnO/p-Si HETEROJUNCTION SOLAR CELL FABRICATION AND CHARACTERIZATION

5.1 Introduction

To fabricate n-ZnO/p-Si single heterojunction solar cell (SHJSC), ZnO was deposited on p-Si substrates using RF magnetron sputtering and then front and back metal contacts were made using handmade shadow masks. The electrical characterization of the n-ZnO thin films was carried out by Hall measurements which revealed that resistivity of the ZnO film is too high to measure current-voltage (I-V) characteristics. Therefore, suns- V_{OC} measurements were made to circumvent effects of series resistance. A summary of best results recently achieved by other researchers has been incorporated in this chapter. We have prepared several n-ZnO/p-Si SHJSC samples and performed suns- V_{OC} measurements to validate the experimental value of V_{OC} because there are discrepancies in the measured value of V_{OC} of n-ZnO/p-Si SHJSC in the literature. Previous work on n-ZnO/p-Si SHJSC has already been cited in Chapter 1 (section 1.4). We obtained a repeatable value of V_{OC} of 260 mV which is very close to the value reported in literature by other researchers. This value is much lower than theoretical value of >600 mV predicted by PC1D simulations based on band bending between n-ZnO and p-Si.

This chapter also presents a theoretical description of heterojunction formation between n-ZnO and p-Si based on Anderson energy-band model. At the end, a discussion is provided about the possible causes of lower experimental value of V_{OC} and the potential solutions to improve the device performance.

5.2 Heterojunction Formation

The energy band diagram of an ideal n-ZnO/p-Si heterojunction is depicted in Fig. 5.1 that seems like a type-II heterojunction. The features of the band alignment are determined based on the Anderson energy-band rule also known as electron affinity model. The conduction band offset (ΔE_C) and valence band offset (ΔE_V) according to Anderson's rule are given by

$$\Delta E_C = \chi_2 - \chi_1 \quad (5.1)$$

$$\Delta E_V = (\chi_2 + E_{g2}) - (\chi_1 + E_{g1}) \quad (5.2)$$

where χ is electron affinity, E_g is bandgap, and subscripts 1 and 2 correspond to Si and ZnO respectively in our case. The electron affinity and bandgap of Si are well known to be 4.05 and 1.12 eV respectively. These values vary significantly in literature for ZnO. The bandgap of ZnO films prepared in our Labs, using both MOCVD and sputtering, turned out to be 3.27 eV which coincides with the values reported by several researchers. Actually, the bandgap of ZnO can be tuned over a large range from 3 to 5 eV by alloying which is considered as one of the unique advantages of ZnO. Sundaram et al. has reported the electron affinity of ZnO around 4.5 eV which was calculated using I-V measurements and Shottky-Mott model [120]. Since the ZnO films are highly doped, their fermi level almost overlaps with the conduction band edge. Therefore, the work function of ZnO is considered same as electron affinity. These values result in ΔE_C and ΔE_V of ~ 0.4 and 2.55 eV respectively. Sundaram et al. has also considered a very thin (1-2 nm) oxide layer at the interface that is likely to develop due to high energy process like magnetron sputtering [121] [122]. The carrier flow across the junction is largely affected by oxide layer thickness that dictates the tunneling coefficient [123].

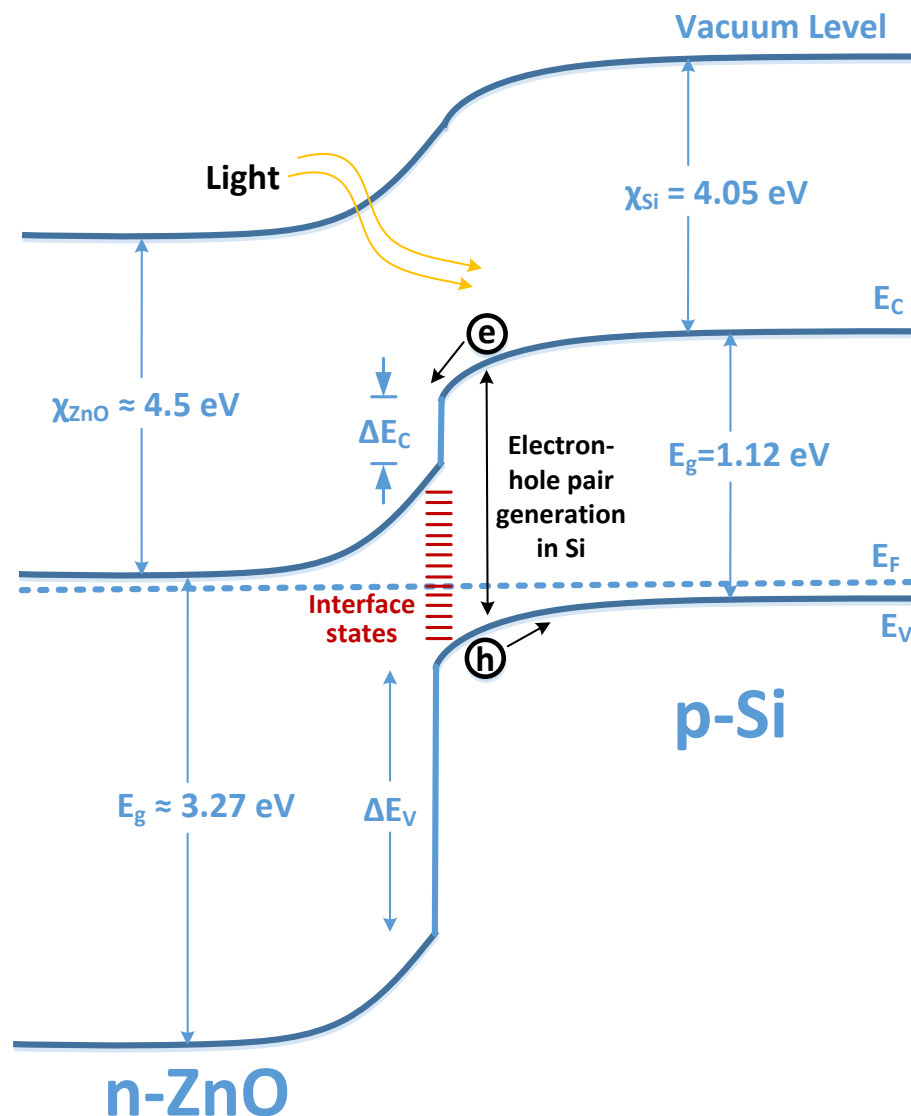


Fig. 5.1. Schematic diagram of n-ZnO/p-Si heterojunction band-bending.

There are two limitations of the Anderson's rule [124]. The first is that Anderson's rule neglects electron correlation effect. The correlation effect occurs when electron moves to the vacuum level (according to definition of electron affinity) and surrounding electrons rearrange themselves to reduce the total energy of the system. The magnitude of correlation effect is generally very small. The second drawback is the lack of consideration of lattice mismatch and interface defects. Dangling chemical bonds at the interface of two

semiconductors form interface states. Conduction and valence band discontinuities are affected by the dipole effects induced by electron transfer. Interestingly, the dipole effect is significantly reduced and becomes negligible if there is large lattice mismatch as is the case with ZnO/Si heterojunction [125]. Therefore, Anderson's rule is valid to determine band edge offsets of a highly mismatched ZnO/Si heterojunction.

5.3 n-ZnO/p-Si Solar Cell Device Fabrication

5.3.1 ZnO Deposition by RF Sputtering

A few samples were prepared by sputtering ZnO on Sapphire and Si substrates at a temperature of 300 °C using sputtering system by AJA International Inc. The rotation speed was approximately 20 rpm. The RF power was 180 W, frequency was 13.56 MHz, and sputtering time was 90 minutes. The pre-cleaning of substrates and optimization of growth conditions was discussed in chapter 3. The thickness of ZnO films was around 190 nm with sputtering rate of ~2 nm/min. The thickness of the sputtered ZnO film was measured by mechanical profilometer as well as filmetrics tool. Both methods gave almost same value of thickness. Although, the crystal quality was reasonable, it can be further improved by raising growth temperature beyond 300 °C which is the upper limit of our sputtering system. Optical characterization using photoluminescence, transmission and interferometric spectral reflectance, and structural characterization using XRD, SEM and AFM were presented in chapter 3.

5.3.2 Electrical Characterization

The hall measurements at room temperature were performed to determine the carrier concentration, mobility and resistivity of the samples. These three electrical measurements for a ZnO sample grown on Sapphire are graphed in Fig. 5.2 as a function of distance in

the sample. As expected, the ZnO film was inherently n-doped with carrier concentration around $1.8 \times 10^{18} \text{ cm}^{-3}$. The sample has good uniformity in electrical characteristics over the surface. Unintentional n-type doping can be attributed to oxygen vacancies or zinc interstitials. But it is also argued that hydrogen and other impurities are more responsible for this behavior [56] [57]. As compared to p-type doping, it is easy to achieve n-doped ZnO layers with a desired carrier concentration using different techniques. It is possible to grow n-doped ZnO thin films by incorporating Mg, In, Al, Ga and their combinations. But it is still a challenge to obtain reproducible, consistent, reliable and highly conductive p-type ZnO thin films and nanostructures.

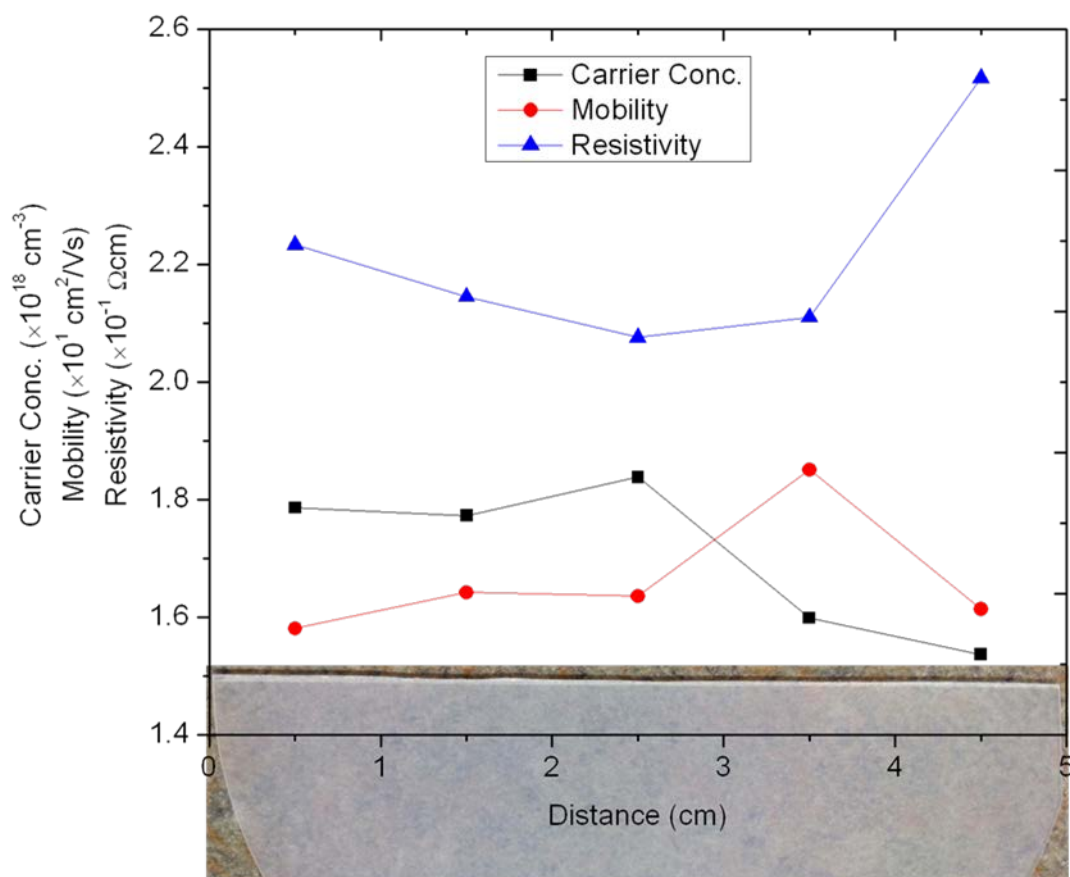
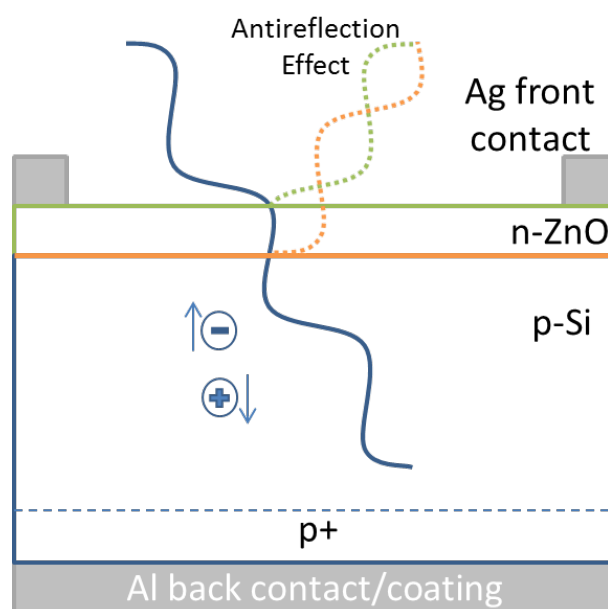


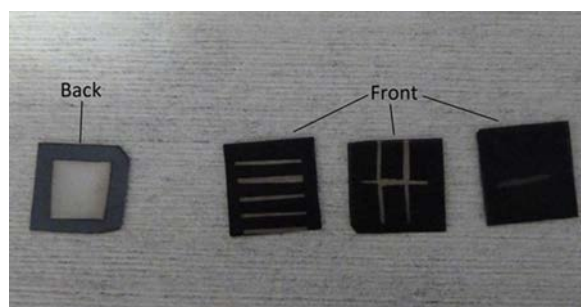
Fig. 5.2. Unintentional n-type carrier concentration, mobility, and resistivity of a ZnO thin film as a function of distance from the edge of the sample. The film was grown on sapphire substrate for convenience in Hall measurements.

The samples prepared by MOCVD had similar electrical characteristics as sputtered samples. Fortunately, the carrier concentration optimized by PCID (section 4.3.4) for our proposed model is very close to the value measured for the samples prepared by MOCVD and sputtering in our labs. Therefore, for initial device fabrication, doping arrangements are not required and the first solar cell can be made using available facilities.

5.3.3 *Contacts Formation by E-Beam Evaporation*



(a)



(b)

Fig. 5.3. Solar cell device using ZnO as an active n-layer and AR coating (a) schematic (b) contact formation on device with 1 cm^2 area using handmade shadow mask.

The samples were again cleaned with acetone in ultrasonic bath before contact deposition using e-beam evaporation. The front Ag-contact and back Al-contact were

deposited by Kurt J. Lesker system using handmade shadow masks. A few samples with different number of fingers were prepared to examine the effect of finger spacing. The edges were isolated during contact deposition. Figure 5.3 (a) depicts schematic of the n-ZnO/p-Si solar cell device where ZnO is acting as electrically active n-layer as well as AR coating saving fabrication complexity and cost. Figure 5.3 (b) is a photograph of a few n-ZnO/p-Si SHJSC devices fabricated in the first trial of experiments.

5.4 Effect of Series Resistance on I-V Measurements

An ideal solar cell can be modeled by a current source (representing photocurrent) in parallel with a diode. But practically, every solar cell has a shunt resistance (R_{SH}) and a series resistance (R_S) as shown in Fig. 5.4 (a). Usually, the shunt resistance is very high and can be considered as open for specific purposes. Under dark conditions, omitting current source and neglecting R_S , the circuit simplifies as shown in Fig. 5.4 (b) for I-V measurement.

The mathematical description of I-V characteristics for ideal diode are given by

$$I = I_L - I_0 \left(e^{\frac{qV}{nkT}} - 1 \right). \quad (5.3)$$

The exponential term inside brackets is usually much larger than 1. Also $I_L = 0$ under dark so the equation simplifies to

$$I = -I_0 \left(e^{\frac{qV}{nkT}} \right) \quad (5.4)$$

which can be written in form of proportionality expression as

$$I \propto e^{\frac{qV}{nkT}} \quad (5.5)$$

The proportionality expression is valid for an ideal diode. In case of series resistance as shown in Fig. 5.4b, the expression modifies to

$$I \propto e^{\frac{q(V-IR_S)}{nkT}} \quad (5.6)$$

The expression (5.6) is numerically solved in MATLAB qualitatively to evaluate the effect of series resistance on the curvature on I-V curve as shown in Fig. 5.5.

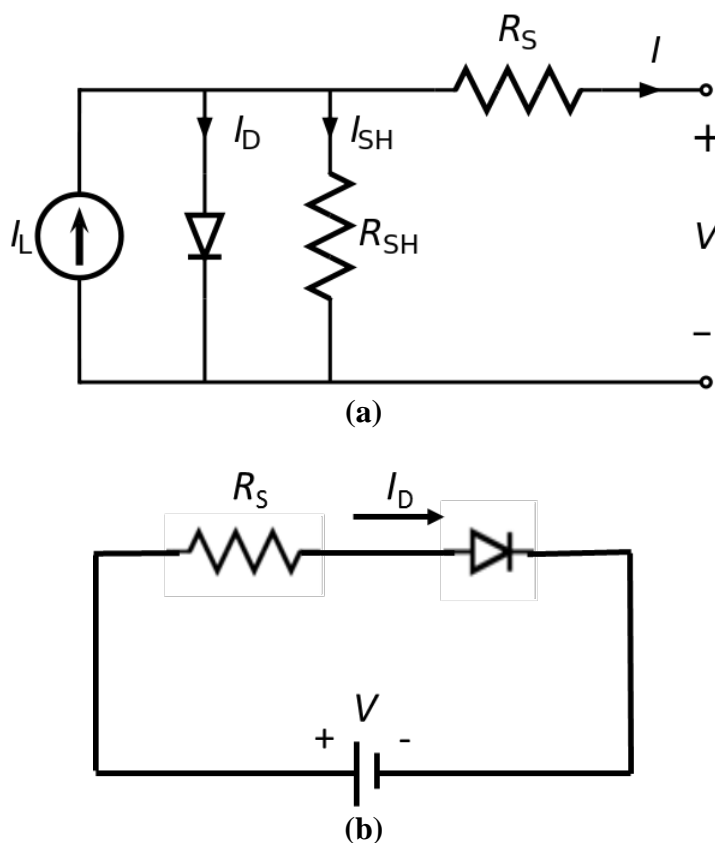


Fig. 5.4. Equivalent circuit of a practical solar cell (a) practical solar cell (b) under dark condition considering shunt resistance as open.

The ZnO films grown in our lab have a resistivity larger than $0.2 \Omega\text{cm}$ as shown in Fig. 5.2 where the resistivity should be at least 20 times less than this value to get reasonable current [81] which is possible by doping ZnO with Al or Mg. This whole discussion about effect of R_S on I-V measurements proves that direct I-V measurements are valid for solar cells having very low value of R_S . Otherwise, the I-V curve will show ohmic-like behavior making determination of V_{OC} value impossible. Therefore, we have employed suns- V_{OC}

measurements, that circumvent series resistance, to quantify actual V_{OC} value of the n-ZnO/p-Si SHJSC in which undoped ZnO is deposited which inherently turns out to be n-type.

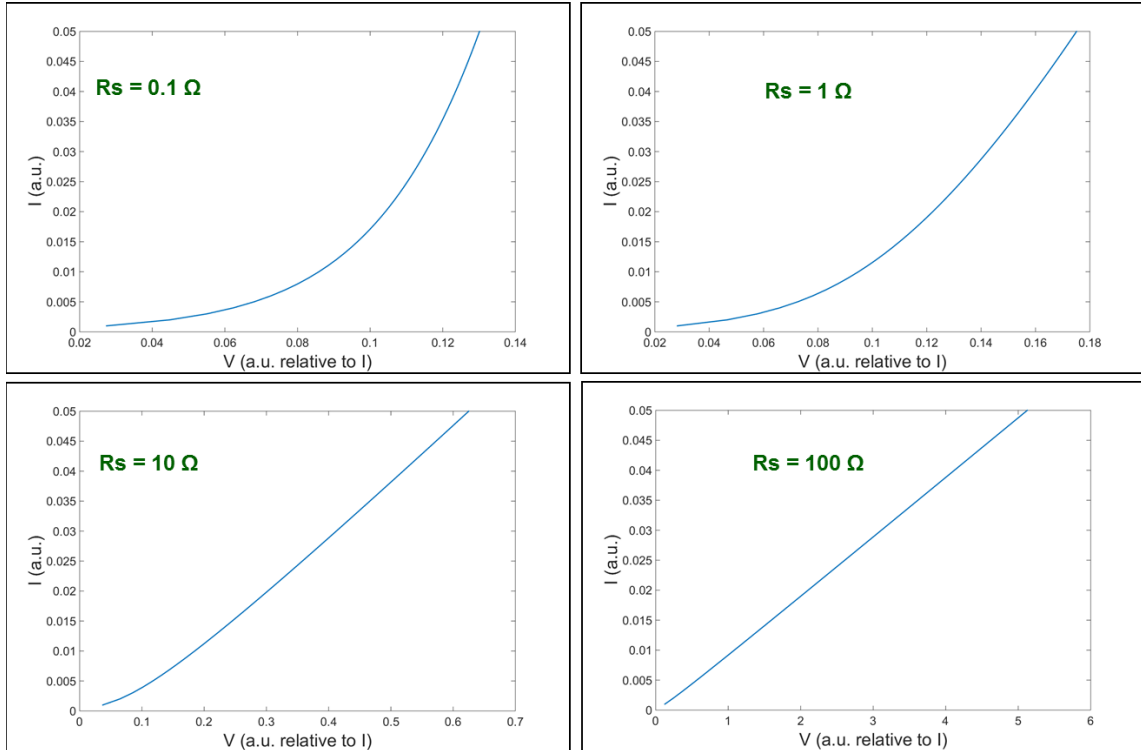


Fig. 5.5. Effects of series resistance on I-V characteristic measurements.

5.5 Suns- V_{OC} Measurements

Suns- V_{OC} measurement is a relatively new technique, in which a flash lamp is used to produce monotonically varying illumination and resultant time dependent photoconductance of the sample is measured. Proper analysis requires use of the continuity equation for the excess minority carrier density. For the case of low injection, the continuity equation for the excess minority carriers in a semiconductor reduces to [126]

$$\frac{\partial \Delta n(x, t)}{\partial t} = G(x, t) - \frac{\Delta n(x, t)}{\tau_{bulk}} + D_n \frac{\partial^2 \Delta n(x, t)}{\partial x^2} \quad (5.7)$$

where Δn , G , τ , and D_n are excess minority carrier density, generation rate, lifetime and diffusion coefficient respectively. The minority carriers' loss due to surface recombination at the wafer of thickness W is given by the boundary conditions

$$D_n \left. \frac{\partial \Delta n(x, t)}{\partial x} \right|_{x=0} = S_{front} \Delta n(0, t) \quad \& \quad -D_n \left. \frac{\partial \Delta n(x, t)}{\partial x} \right|_{x=W} = S_{back} \Delta n(W, t) \quad (5.8)$$

where S is the surface recombination velocity. Integrating Eq. (5.7) over the wafer width gives

$$\begin{aligned} & \frac{\partial}{\partial t} \int_0^W \Delta n(x, t) dx \\ &= \int_0^W G(x, t) dx - \frac{1}{\tau_{bulk}} \int_0^W \Delta n(x, t) dx + D_n \left. \frac{\partial \Delta n(x, t)}{\partial x} \right|_{x=W} - D_n \left. \frac{\partial \Delta n(x, t)}{\partial x} \right|_{x=0} \end{aligned} \quad (5.9)$$

Dividing the whole equation by the wafer width W , and using the boundary conditions from Eq. (5.8), the expression reduces to

$$\frac{d\Delta n_{av}(t)}{dt} = G_{av}(t) - \frac{\Delta n_{av}(t)}{\tau_{eff}(\Delta n_{av})} \quad (5.10)$$

where

$$\Delta n_{av}(t) = \frac{1}{W} \int_0^W \Delta n(x, t) dx \quad (5.11)$$

$$G_{av}(t) = \frac{1}{W} \int_0^W G(x, t) dx \quad (5.12)$$

$$\frac{\Delta n_{av}(t)}{\tau_{eff}(\Delta n_{av})} = \frac{\Delta n_{av}(t)}{\tau_{bulk}(\Delta n_{av})} + \frac{1}{W} S_{front} \Delta n(0, t) + \frac{1}{W} S_{back} \Delta n(W, t) \quad (5.13)$$

The Sinton Instruments tool measures the illuminated power, $G_{av}(t)$, using a calibrated solar cell and the conductivity of the sample using an inductive coil. Using measured data in numerical simulations, the control program computes the average value of excess minority carrier density, $\Delta n_{av}(t)$, bulk and effective lifetimes, and front/back recombination

velocities. Then the actual illumination level can be plotted against an implied V_{OC} using the relationship [127]

$$np \approx \Delta n(0)[N_A + \Delta n(0)] = n_i^2 \exp\left(\frac{qV_{OC}}{kT}\right) \quad (5.14)$$

where N_A is the doping concentration in p-Si wafer.

The initially fabricated devices, a few of them shown in Fig. 5.3 (b), were tested by suns- V_{OC} measurements using Sinton Instruments tool. The results for one of the fabricated device are depicted in Fig. 5.6 which confirms junction formation between n-ZnO and p-Si. The pseudo light IV curve is obtained by using basic diode current-voltage relation given in Eq. (5.3) and then plotting the IV curve in the first quadrant as shown in Fig. 5.6 (b). This IV curve is quantitatively not valid because (1) the photogenerated current I_L is calculated assuming 100% EQE and (2) the series resistance is assumed as zero. The best values of V_{OC} , ideality factor (n), J_{01} , J_{02} , and shunt resistance we obtained are 0.260 V, 1.97, 1.2×10^{-12} A/cm², 1.0×10^{-11} A/cm², and 150×10^3 Ω -cm² respectively. The value of J_{02} was more than two orders larger than J_{01} in most of devices which shows recombination in bulk is more dominant than that at the interface. The low value of V_{OC} is because of (1) the recombination due to defects introduced at the interface and (2) the low crystal quality of the Si substrate. Also, a thin layer of SiO₂ is expected to form at the interface during ZnO growth. If this layer is too thick, it can reduce the tunneling coefficient which results in recombination of the photo-generated carriers in the conduction band in Si through interface states and thus reducing the photocurrent and V_{OC} . The formation of SiO₂ layer at the interface can be prevented by introducing a buffer layer of aluminum nitride (AlN) or titanium nitride (TiN) to compensate the lattice mismatch. The buffer layer will have an extra advantage of reducing reverse saturation current resulting in increased V_{OC} .

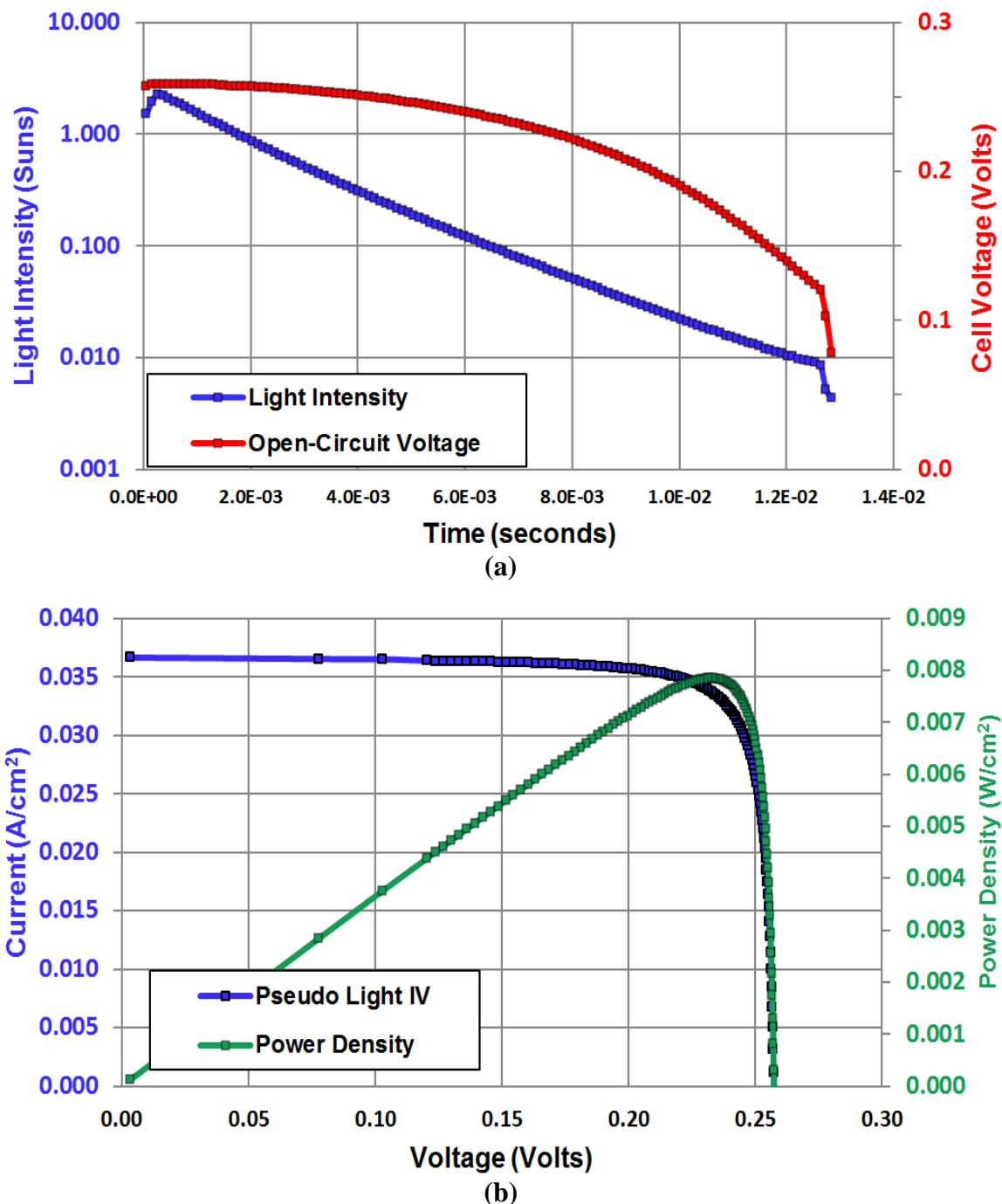


Fig. 5.6. Suns- V_{OC} measurements (a) illumination and test cell V_{OC} (b) pseudo light IV curve without effect of series resistance.

5.6 Contribution by Other Researchers

In 2015, we reported feasibility of n-ZnO/p-Si SHJSC by theoretical analysis, PC1D based simulations, and preliminary experimentation highlighting the feasibility of ZnO as

an electrically active n-layer as well as AR coating [80]. This triggered some researchers to fabricate n-ZnO/p-Si SHJSC and to use ZnO as AR coating [128] [81] [129]. The best experimental efficiency of 7.1% for n-ZnO/p-Si HJSC is reported by Pietruszka et al. using atomic layer deposition (ALD) [81]. Utilizing the model proposed by Knutsen et al. [78], they have incorporated Mg in ZnO to reduce conduction band offset between ZnO and Si that resulted in higher conversion efficiency. Pietruszka et al. prepared four samples named A, B, C and D with different percentages of Mg incorporation in ZnO as shown in Table 5.1.

TABLE 5.1. Photovoltaic parameters of the n-ZnO/p-Si SHJSC prepared by different percentages of Mg alloying in ZnO. The values of Mg percentage, R_S and R_{SH} have different level of uncertainties not shown here for simplicity. The data has been tabulated here after consultation and consent from Pietruszka et al. [81].

Sample	Mg (%)	R_S (Ω)	R_{SH} (Ω)	J_{SC} (mA/cm ²)	V_{OC} (mV)	FF (%)	Eff. (%)
A	0	17	$\sim 10^6$	30.3	257	48	3.7
B	0.7	21	$\sim 10^6$	33.1	307	55	5.6
C	1.6	12	$\sim 10^4$	34.0	304	58	6.0
D	3.8	120	$\sim 10^3$	26.4	268	29	2.1

The current density vs voltage (J-V) characteristics are plotted in Fig. 5.7 for samples A – D measured under standard one sun illumination. The parameters R_{SH} , J_{SC} , V_{OC} and fill factor (FF) were extracted by using the *IV Curve Fitter* software. The efficiency (Eff) was calculated using relation

$$Eff = \frac{J_{SC} V_{OC} FF}{P_{in}} \quad (5.16)$$

where P_{in} is the solar simulator power density having value of 100 mW/cm² for the sample having area of 1 cm².

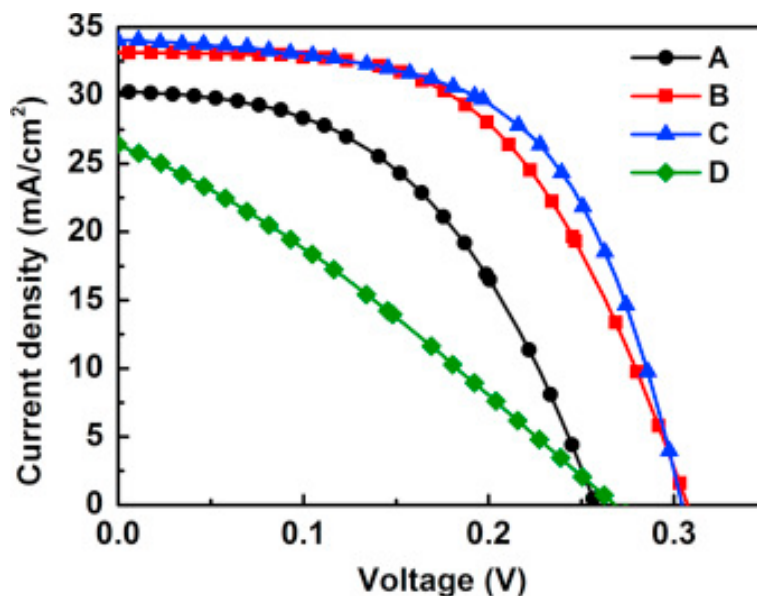


Fig. 5.7. J-V characteristics of the samples A–D prepared with different Mg concentrations in ZnO measured under one sun illumination [81].

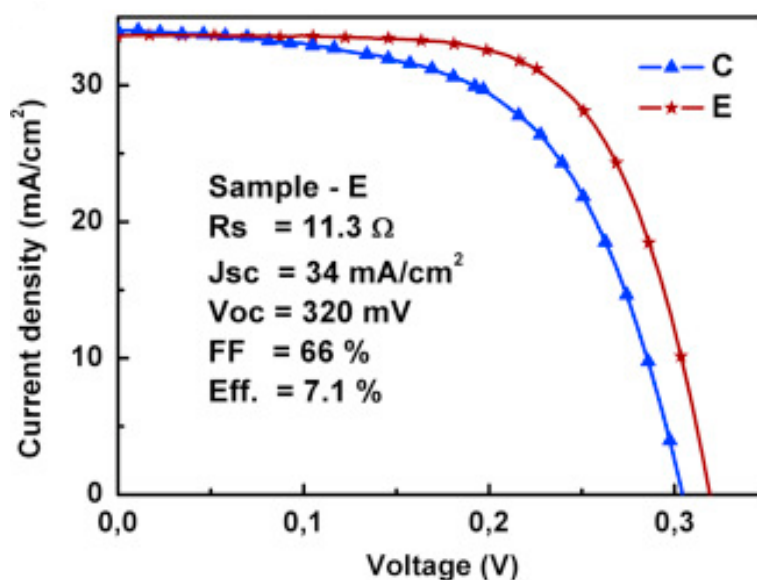


Fig. 5.8. Comparison between the J-V response of the sample C with ZnO deposited at 160 °C and sample E with ZnO deposited at 300 °C [81].

It can be noticed that J-V characteristic curve of sample D, that has $R_S > 100 \Omega$, follows the same trend as predicted by simulations shown in Fig. 5.5. Another sample named ‘E’ was prepared by growing ZnO films at elevated temperature of 300 °C. the J-V curve of the sample measured under 1 sun illumination is shown in Fig. 5.8 with comparison of

sample C. the most significant difference is the values of FF and R_{SH} . The FF value increased from 58% to 66% and R_{SH} improved from $\sim 10^3$ to $\sim 10^6 \Omega$ causing $\sim 1.1\%$ increase in the efficiency due to improvement in crystal quality of ZnO.

5.7 Issues at the Interface of ZnO/Si Heterojunction

The lower experimental value of V_{OC} of n-ZnO/p-Si SHJSC is attributed to Fermi level pinning at the hetero-interface causing high interface recombination velocity [130]. The main reason of high recombination velocity at the heterostructure interface is the defects introduced due to lattice mismatch between the crystal structures of the two materials. The c/a ratio of lattice parameters ($a=3.25 \text{ \AA}$, $c=5.21 \text{ \AA}$) of ZnO wurtzite structure is 1.603 which is very close to the ideal ratio of 1.633 for highly stable structure. This makes ZnO very resistant to UV radiation and harsh environments making it ideal candidate as a front layer of solar cell. However, the drawback is that it has a large mismatch with Si lattice structure. The most common solution to lattice mismatch problem is the use of a buffer (transition) layer between the two materials, though, it can increase the process complexity and fabrication cost. Jin et al. have developed epitaxial ZnO thin films on Si (111) using aluminum nitride (AlN) and magnesium oxide (MgO)/titanium nitride (TiN) buffer layers [131]. AlN has a wurtzite structure similar to that of ZnO with close lattice parameters $a=3.11 \text{ \AA}$ and $c=4.98 \text{ \AA}$ ($\sim 4\%$ mismatch). In epitaxial growth of AlN on Si, integral multiples of the major lattice planes of the film and substrate match across the interface [132]. This can induce some strain in the crystal but has negligible effects for very thin layers. High quality ZnO crystal can be grown on AlN due to close lattice match. TiN and MgO can be grown on each other since both have very close lattice parameters with each other as well as with ZnO. By means of transmission electron microscopy, x-ray

diffraction, and photoluminescence, Jin et al. concluded that both ZnO/AlN/Si and ZnO/MgO/TiN/Si films demonstrate excellent structural, optical, and electrical properties. It is noteworthy that increase in buffer layer thickness raises diode ideality factor; therefore, the buffer layer thickness is of considerable importance for the recombination process [27]. The nanostructures of n-ZnO have also been grown directly on p-Si by chemical vapor deposition to study photoluminescence and electroluminescence properties [133].

A thin layer of SiO₂ is expected to form at the interface during ZnO growth which can significantly influence the solar cell performance. If the SiO₂ layer is too thick, it can reduce the tunneling coefficient resulting in recombination of photo-generated holes with electrons in the conduction band in Si via interface states consequently suppressing the photocurrent. If a buffer layer of AlN or TiN is used to compensate lattice mismatch (as explained earlier), it will have an additional advantage of preventing formation of SiO₂ layer at the interface. Also, the presence of a thin insulating layer can reduce the reverse saturation current causing increase in V_{oc} .

5.8 Gallium Alloying in ZnO to Increase Bandgap

Our undoped ZnO samples have a bandgap around 3.27 eV (~380 nm). According to ASTM G-173 spectra provided by NREL, around 10% “intensity” of solar spectrum lies below this wavelength. Since absorption coefficient of ZnO is on the order of 10⁵ cm⁻¹, the absorption length is around 100 nm. Therefore, most of the UV portion of solar radiation would be absorbed in the 100 nm thick ZnO layer. This is undesired because the photons absorbed before the heterojunction are less likely to contribute in photogenerated current due to absence of high electric field in the depletion region because the built-in voltage of our heterostructure is mostly on the low-bandgap (Si) side. Fortunately, the bandgap of

ZnO can be increased to up to 5 eV by incorporating high ratio of gallium (Ga) content [38]. It improves transmission and electrical characteristics of the film as well [47] [60]. Therefore, we have grown Ga rich ZnO:Ga films using MOCVD to examine the bandgap tuning. Trimethylgallium was used as the Ga source. The doped films were grown with the same optimized temperature and other conditions as explained in chapter 2 for pure ZnO growth. The PL spectra of both ZnO and ZnO:Ga were dominated by the near band edge (NBE) emission as depicted in Fig. 5.9. The spectra are normalized to their maximum values. The bandgap is blue-shifted by about 105 meV (12 nm). These PL spectra should not be confused with those presented in Fig. 2.3. These films are much thicker ($\sim 5 \mu\text{m}$); therefore, PL spectra shown here are much broader. The molar ratio of Ga was around 50% during our growth process which lead to a bandgap around 3.35 eV (370 nm). This is in accordance with the model reported by Zhao et al. [38]. We attribute this increase in bandgap to well-known Burstein-Moss effect in which effective bandgap of a heavily doped semiconductor is increased as the absorption edge in conduction band moves to higher energies because all states close to the conduction band edge are filled. It is important to note that Burstein-Moss shift will reduce by decreasing temperature and will eventually disappear at cryogenic temperatures.

The intensity of NBE emission decreases with Ga incorporation which can be analyzed by difference in laser (used for excitation) related peak at 250 nm illustrated in Fig. 5.9. This implies that Ga-doping produces local strain around Ga atoms creating non-radiative channels. This causes annihilation of the exciton radiative transition and thus limiting the radiative efficiency of NBE emission [134]. Similar results have been reported by other researchers for Ga-doped ZnO prepared by MOCVD [135] and spin coating [36]

techniques. However, linewidth (FWHM) of NBE emission does not increase in our Ga-doped ZnO films contradicting the results reported by Ye et al. [39]. They have developed a reasonable argument attributing the linewidth increase to unavoidable inconsistency of doping concentration giving rise to tail states resulting in broadening of luminescence linewidth. Further study is required to understand the mechanism behind the broadening of NBE emission observed by Ye et al. but not witnessed in our samples.

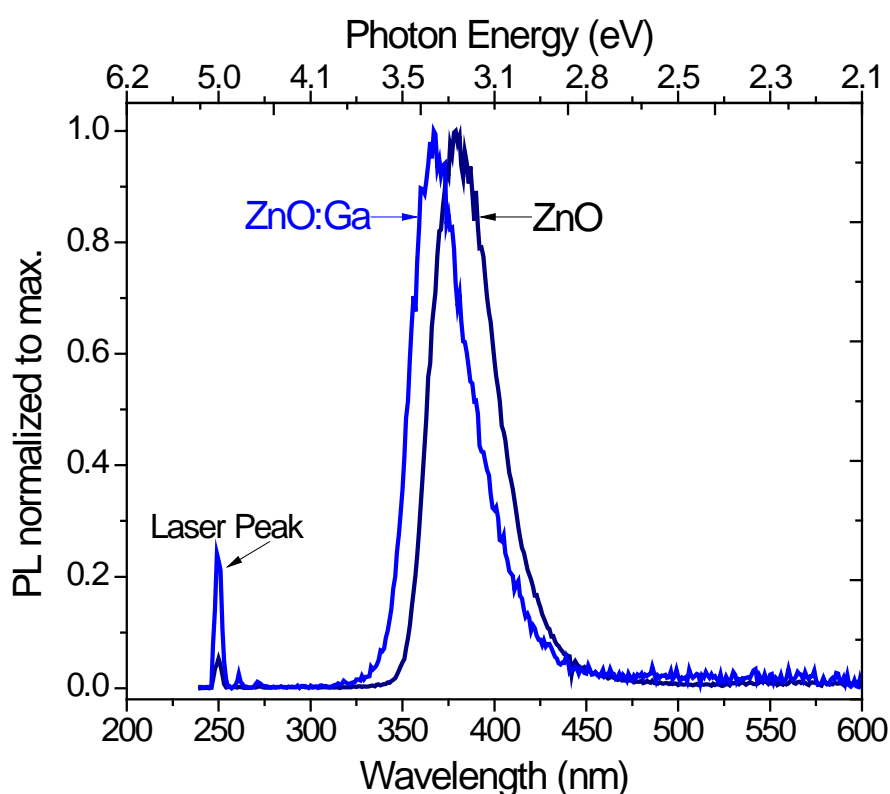


Fig. 5.9. PL spectra of pristine ZnO and Ga-rich ZnO:Ga showing increase in bandgap due to Burstein-Moss shift suitable for ZnO use as a front layer of solar cell.

In case of heavy Ga-doping in ZnO and resulting Burstein-Moss shift, the film will most probably be degenerate and behave like a metallic electrode. Then, the heterostructure is expected to act like a Schottky diode instead of p-n junction. This can greatly modify the device performance and cell parameters. In this scenario, again, the insulating buffer layer

can play a vital role because diode ideality factor and barrier height are highly dependent on buffer layer thickness in Schottky solar cells [136]. Graphene based Schottky diode solar cells have been reported exhibiting reasonable efficiency but a tradeoff is required in conductivity and transparency of the graphene sheets to optimize the performance [137] [138]. Where the Ga-doping in ZnO not only increases electrical conductivity but also transparency of the films.

Experimental results presented in this chapter and in literature suggest that ZnO can be used with Si to fabricate efficient, durable, and cost effective heterostructure solar cells. The proposed device does not need p-type doping in ZnO which is a well-known issue with this material. But tremendous amount of research and experimental study is required to understand and overcome the problems associated with recombination at the hetero-interface. Study concerning the band offset and the Fermi level position at the interface is also necessary, since charge transfer and recombination activity depend on these factors [14].

5.9 Summary

In this chapter, theoretical analysis of type-II n-ZnO/p-Si heterojunction formation was provided with the help of band-bending diagram and Anderson's rule. Then the different processing steps involved in the fabrication of n-ZnO/p-Si SHJSC device were explained. Electrical characterization using Hall measurement showed that inherent doping level of n-ZnO films is fortunately close to the value ($\sim 10^{18} \text{ cm}^{-3}$) optimized for the solar cell by PC1D modeling, but the resistivity of the films is too high to evaluate samples using I-V characterization. Therefore, suns- V_{OC} measurements were used to quantify V_{OC} of the solar cells. We obtained a repeatable value of V_{OC} of 260 mV which is very close to the value

reported in literature by other researchers. This value was much lower than theoretical value of >600 mV predicted by PC1D simulations based on band bending between n-ZnO and p-Si. The possible reasons and potential solutions of the lower experimental value of V_{OC} were discussed. Furthermore, Ga-doped ZnO films were prepared to study bandgap tuning of ZnO to utilize maximum possible energy of the solar spectrum.

CHAPTER 6: IMPROVEMENT IN OPEN CIRCUIT VOLTAGE OF n-ZnO/p-Si SOLAR CELL BY USING AMORPHOUS-ZnO AT THE INTERFACE

6.1 Introduction

The main reason behind the difference between theoretically predicted and practically achieved conversion efficiency of n-ZnO/p-Si HJSC is that experimental open circuit voltage (V_{OC}) is much lower than the predicted value of V_{OC} (~650 mV) based on band-bending between n-ZnO and p-Si. Most of the researchers attribute this lower value of V_{OC} to the interface states because of lattice mismatch between ZnO and Si. As explained in previous chapter, we have demonstrated the experimental value of V_{OC} as 260 mV after preparing several samples of n-ZnO/p-Si HJSC by depositing intrinsic ZnO on p-Si wafers by RF magnetron sputtering.

In this chapter, we report >20% improvement in V_{OC} of n-ZnO/p-Si HJSC by simply depositing amorphous-ZnO (a-ZnO) at the interface between crystalline ZnO (c-ZnO) and Si. Two other materials, amorphous-Si (a-Si) and aluminum nitride (AlN) were also deposited as a buffer layer (BL) between c-ZnO and Si-wafer. But the best V_{OC} was achieved for the device having a-ZnO at the interface. The improvement in V_{OC} is probably due to elimination/reduction in SiO_x formation at the interface of c-ZnO and Si-wafer, and/or reduction in the interface states. Additionally, we demonstrate significant decrease in reflection from front surface of the solar cell when ZnO is used as the front n-layer.

6.2 Materials and Methods

Solar cells were fabricated using three types of Si wafers: (type-1) boron-doped p-type (100) wafers with resistivity 1.5 Ωcm and thickness 90 μm , (type-2) boron-doped p-type (100) wafers with resistivity 0.7–5 Ωcm and thickness 500 μm , and (type-3) boron-doped p-type (111) textured wafers with resistivity 2 Ωcm and thickness 190 μm . The Si wafers were cut into $1\times 1\text{ cm}^2$ pieces and then cleaned in three stages. (i) The wafers were subsequently placed in acetone container on to a hot plate at 55 $^{\circ}\text{C}$ for 10 minutes, in methanol at room temperature for 5 minutes, rinsed with deionized (DI) water, and dried with nitrogen. (ii) To remove the organic residues, Si wafers were placed in $\text{H}_2\text{O}_2/\text{H}_2\text{SO}_4$ solution of 2:3 ratio for 20 minutes and then rinsed with DI water. (iii) To etch the SiO_x layer at the surface, the wafers were dipped in 10% hydrofluoric (HF) solution for 10 seconds (proper procedure should be adopted while using this dangerous acid). Then the wafers were again rinsed with DI water and dried in nitrogen. After the HF-solution dip, the Si wafers are supposed to have hydrogen-terminated surface and less likely to develop SiO_x at room temperature.

Three types of n-ZnO/BL/p-Si solar cell samples were prepared each with different type of buffer layer (BL); AlN, a-Si, or a-ZnO. AlN BL of thickness $\sim 5\text{ nm}$ was deposited by RF sputtering using CVC AST-601 tool with RF power and rotation speed of 150 W and 10 rpm respectively. Before depositing AlN as BL, the growth rate of 1.67 nm/min of AlN was calibrated by preparing a few samples of different thicknesses. The a-Si BL of thickness $\sim 5\text{ nm}$ was deposited using Kurt J. Lesker e-beam evaporation system. The growth rate of a-Si was calibrated as well. The a-ZnO BL and c-ZnO n-layer were deposited by AJA International Inc. sputtering system. The sputtering pressure was 3×10^{-3} torr in

argon gas environment and the susceptor rotation speed was set to 20 rpm. The RF power and frequency used for ZnO sputtering were 180 W and 13.56 MHz respectively. ZnO does not crystallize if sputtered at room temperature. Therefore, during a-ZnO BL deposition, temperature was kept at 20 °C. The thickness of a-ZnO layer is estimated to be 8–10 nm based on growth rate of 2.5 nm/min and deposition time of 4 minutes. The temperature was raised to 300 °C to deposit c-ZnO n-layer. The front and back Al contacts were made by using shadow mask in Kurt J. Lesker e-beam evaporation system. The samples were again cleaned with acetone in ultrasonic bath before contact deposition. The edges were isolated during contact deposition. The Fig. 6.1 shows schematic and optical pictures of the final solar cell device.

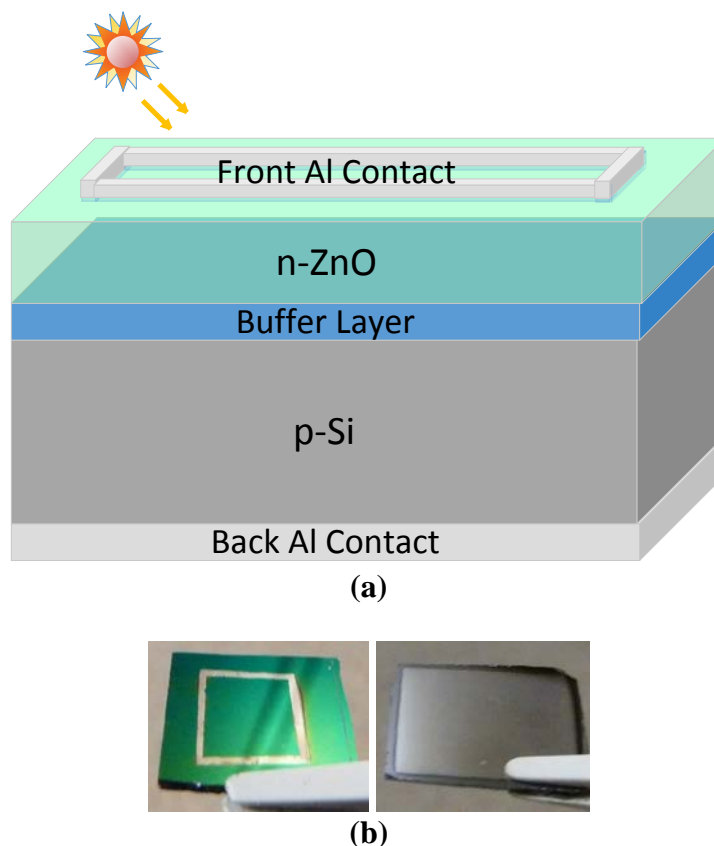


Fig. 6.1. (a) Schematic of the n-ZnO/BL/p-Si solar cell (b) Optical pictures of the front (left) and back (right) of an n-ZnO/BL/p-Si solar cell of size 1cm×1cm.

Crystallinity of the ZnO films was characterized by PANalytical X-ray diffractometer. Scanning electron microscopy (SEM) images were obtained using SEM column part of the Raith 150 e-beam lithography system. The thickness measurements were carried out by Filmetrics F20-UV system that exploits spectral reflectance data to calculate thickness, optical constants, and roughness of the sample. The photoluminescence (PL) measurements were performed by MiniPL-5.0 system by Photon Systems Inc. that has a built-in laser with a wavelength of 250 nm. The V_{OC} measurements were made by Suns- V_{OC} measurement system by Sinton Instruments. The absolute specular reflection measurements were conducted by Ocean Optics system using integrated sphere. All the characterization measurements were performed at ambient temperature.

6.3 Characterization Results and Analysis

6.3.1 Effects of Type of Wafer on the Crystallinity of ZnO

The crystal orientation and texturing of the Si wafer also showed significant effect on the crystallinity of ZnO films. The Figs. 6.2 (a) and 6.2 (b) show SEM micrographs of ZnO films deposited on type-1 and type-3 Si wafers respectively. Both samples were prepared under same conditions at 300 °C but the surface roughness is much poor in case of the textured Si substrate. One possible reason of degradation in crystal quality in the type-3 sample is uneven crystal growth orientation due to the textured surface. There are a few reports about ZnO thick films grown on non-textured Si but not enough data is available related to the quality of ZnO thin films deposited on textured Si substrates. Therefore, further experimental study is needed to understand the degradation in crystal quality of ZnO deposited on textured Si wafers.

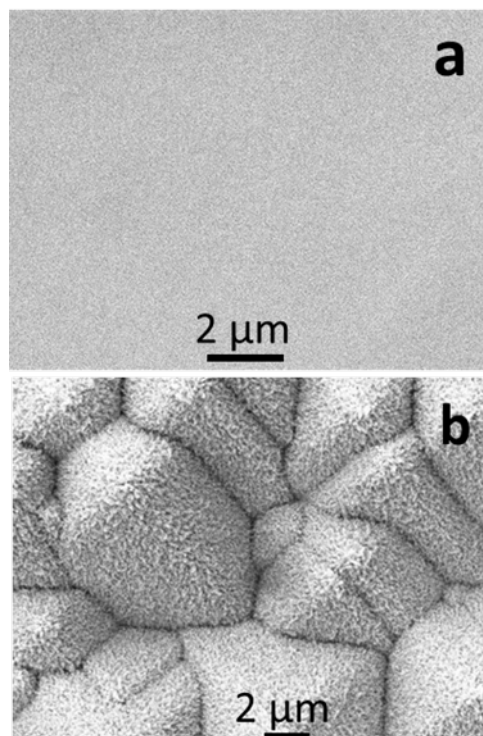


Fig. 6.2. SEM images of ZnO deposited at 300 C by sputtering on (a) type-1 and (b) type-3 Si wafer.

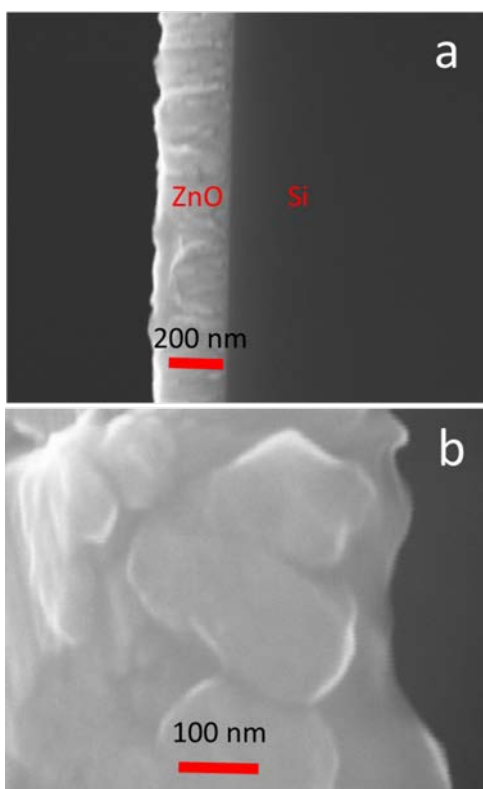


Fig. 6.3. (a) SEM image of the cross-section of the n-ZnO/a-ZnO/p-Si structure (b) Higher resolution SEM image of n-ZnO/AlN/p-Si structure showing grain size more than 100 nm.

The Fig. 6.3 (a) shows SEM image of the cross-section of the n-ZnO/a-ZnO/p-Si structure. The thickness of ZnO layer is ~250 nm which is very close to value measured by spectral reflectance technique. A high resolution SEM image of n-ZnO/AlN/p-Si structure is depicted in Fig. 6.3 (b). It can be noted that the grain size is on the order of 100 nm which is consistent with the grain size value calculated using XRD data. Transmission electron microscopy (TEM) of the cross-section could provide more useful information about the interface morphology.

6.3.2 *Suns- V_{OC} Measurements*

The description of suns- V_{OC} measurement technique and its usefulness has been explained in section 5.5 in the previous chapter. Fig. 6.4 shows time-varying illumination light intensity and corresponding inferred V_{OC} of one of our best n-ZnO/a-ZnO/p-Si solar cell samples. The value of V_{OC} at 1-sun is 359 mV. Fig. 6.5 demonstrates power density curves plotted by suns- V_{OC} system for the best samples related to the three structures of n-ZnO/BL/p-Si solar cell as well as a simple n-ZnO/p-Si structure without the buffer layer. The ranges of the V_{OC} values for the several samples of each of the structures are listed in Table 6.1. We attribute improvement in V_{OC} to reduction in SiO_x formation and suppression in the interface states due to a-ZnO buffer layer. SiO_x layer is more likely to develop at higher temperatures. Since the a-ZnO layer is deposited at room temperature; therefore, it inhibits oxidation of Si. Once a-ZnO covers the Si wafer surface, it prevents oxidation even when c-ZnO is deposited at 300 °C as the next processing step. It probably suppresses interface states and consequential electron-hole recombination rate as well due to reduction in surface dangling bonds as a-Si does in case of HIT heterojunction Si solar

cell. Further experimental study is required to understand the effects of a-ZnO buffer layer on the interface states.

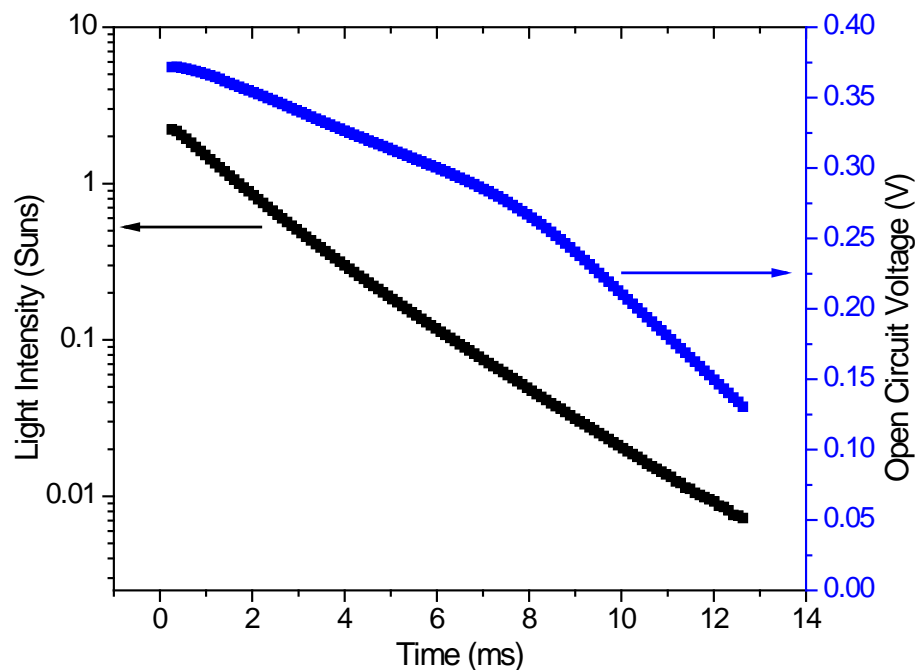


Fig. 6.4. Time-varying illumination light intensity and corresponding inferred V_{OC} of one of our best n-ZnO/a-ZnO/p-Si solar cell samples. The value of V_{OC} at 1-sun is 359 mV.

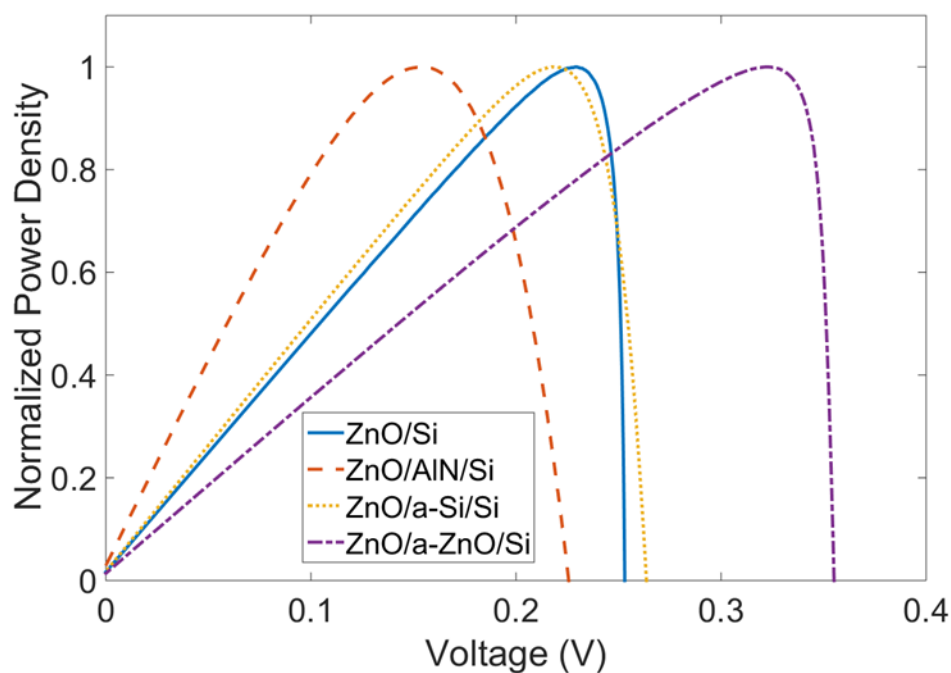


Fig. 6.5. Power density curves plotted by suns- V_{OC} system for best samples related to the three structures of n-ZnO/BL/p-Si solar cell as well as a simple n-ZnO/p-Si structure without buffer layer.

TABLE 6.1. V_{oc} values measured for several samples of the four structures.

Structure	Range of V_{oc} values (mV)
n-ZnO/p-Si	235 – 260
n-ZnO/AlN/p-Si	211 – 231
n-ZnO/a-Si/p-Si	224 – 267
n-ZnO/a-ZnO/p-Si	338 – 359

6.3.3 Antireflection Effect of ZnO

Besides the other advantages of ZnO, its refractive index is very close to the value required for an antireflection (AR) coating of Si. Therefore, ZnO can work as an n-type layer of the solar cell as well as the AR coating reducing device fabrication complexity and cost. We have deposited ZnO layers having different thicknesses on Si wafers to experimentally evaluate the AR effect. Fig. 6.6 shows reflection spectra measured from bare Si and ZnO/Si structure for four different thicknesses of ZnO film. It can be clearly observed that reflection significantly reduces for all the thicknesses of ZnO as compared to the bare Si. The optimized value of ZnO film thickness was previously mentioned in chapter 4 (section 4.2) as 75 nm. It can be seen that the minimum reflection corresponds to the ZnO film of thickness ~ 72 nm. The thickness of ZnO films was measured by spectral reflectance that was giving a variation of $\sim \pm 2$ nm in thickness measurements. It is noteworthy that reflection considerably increases for the thickness value of 82 nm. Therefore, precision in thickness control of ZnO films plays an important role in the solar cell performance. Hence another advantage of sputtering technique is that it provides better control on the thickness of ZnO during deposition. As discussed earlier, spatial thickness uniformity is also better for the films prepared by sputtering as compared to MOCVD. It can also be noticed that in Fig. 6.6 reflection reduces for thicker films (181 nm and 249 nm) as well. This is important because the relatively high sheet resistance of the thin ZnO

layer imposes a requirement of close grid line spacing for the front contacts resulting in increased shadowing effect and decreased solar cell performance. Thicker ZnO films can be used to reduce the sheet resistance that will still significantly reduce the reflection as compared to bare Si. The reflection will further decrease if ZnO with good structural quality can be grown on textured Si wafers, although thicker ZnO will reduce the transmission. Reflection is still high for the 600-400 nm region with the best thickness. Another AR coating can be added to achieve a broad range reduction in reflection.

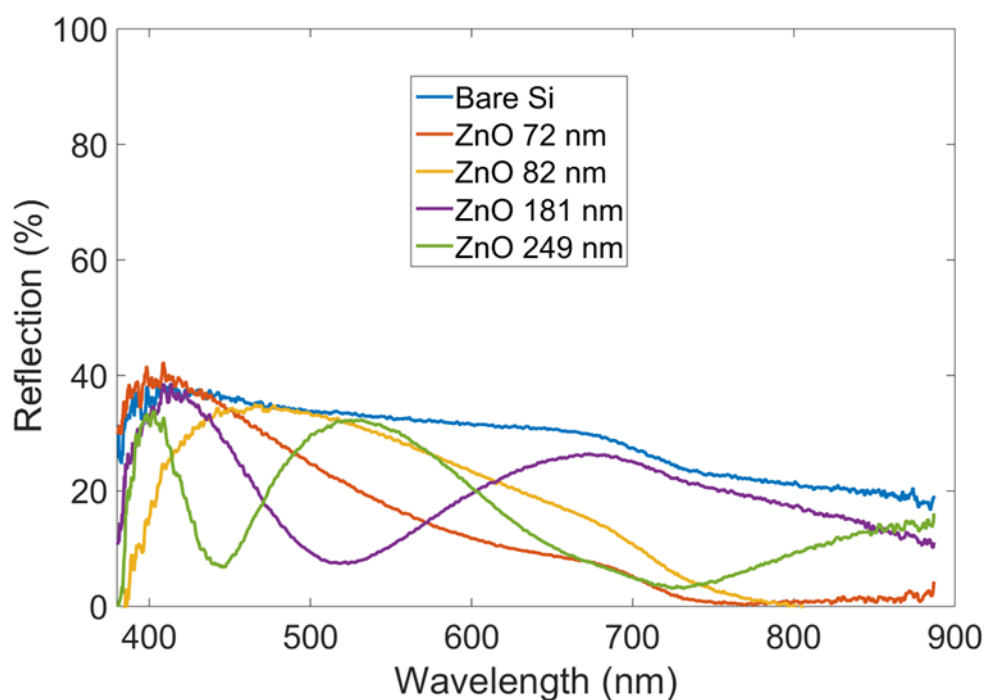


Fig. 6.6. Reflection spectra measured from bare Si and ZnO/Si structure for four different thicknesses of ZnO film. The reflection is significantly less than that of bare Si for all the thicknesses of ZnO proving additional antireflection effect of ZnO film.

6.4 Discussion

6.4.1 Importance of Buffer Layer

The most common solution to the lattice mismatch problem is the use of a buffer (transition) layer between the two materials. AlN has a wurtzite structure similar to that of

ZnO with close lattice parameters $a=3.11 \text{ \AA}$ and $c=4.98 \text{ \AA}$ (~4% mismatch). In epitaxial growth of AlN on Si, integral multiples of the major lattice planes of the film and substrate match across the interface. This can still induce some strain in the crystal but has negligible effects for very thin layers. We have deposited AlN buffer layer using a separate sputtering system (CVC AST-601) that can sputter at room temperature only resulting in poor crystal quality. Also, we note that thickness control for films having thickness below 50 nm is very difficult to achieve with this tool. It is noteworthy that increase in buffer layer thickness raises diode ideality factor; therefore, the buffer layer thickness is of considerable importance for the recombination process [27]. We attribute lower V_{OC} of n-ZnO/AlN/p-Si solar cell (see Fig. 6.6) to low crystal quality and uncertain thickness of the AlN layer.

We have borrowed the idea of a-Si as buffer layer from HIT solar cell in which a-Si passivates the c-Si surface very well reducing surface dangling bond density and reducing effective recombination velocity down to 10 cm/s resulting in increased V_{OC} [139]. Our solar cell structure is different than HIT solar cell because there is c-ZnO at one side instead of doped a-Si. Therefore, the passivation is not expected to be as effective at this side. But the recombination is more likely to happen at the interface towards c-Si because the electric field drives the minority carriers towards the barrier. The carriers pile up to a certain level while waiting to tunnel through the buffer layer (see Fig. 6.7) and are more prone to be recombined. We obtained slight improvement in V_{OC} for a few n-ZnO/a-Si/p-Si solar cell samples but the results are not repeatable and some samples have even worse V_{OC} (see Table 6.1). This is probably due to poor passivation at the interface towards ZnO side. Also, the oxidation cannot be prevented using a-Si as buffer layer because SiO_x can develop on top of a-Si layer while depositing ZnO at higher temperature.

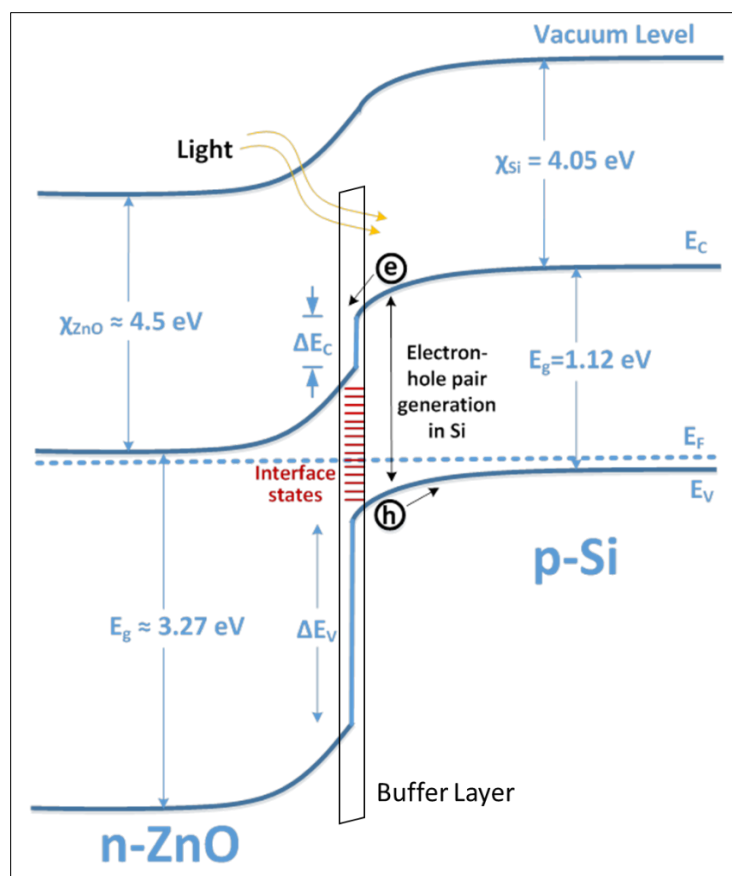


Fig. 6.7. Band-bending diagram of n-ZnO/p-Si heterostructure with a buffer layer at the interface.

The use of a-ZnO as buffer layer showed the best results as can be seen in Fig. 6.6. We attribute this improvement in V_{OC} to two reasons. The a-ZnO is probably passivating both c-Si and c-ZnO surfaces effectively resulting in reduced dangling bonds and improved V_{OC} . Secondly, the a-ZnO is deposited at room temperature therefore SiO_x is less likely to develop on the Si wafer surface. Once the a-ZnO layer is deposited, it prevents formation of SiO_x even at higher temperature when the c-ZnO is deposited as a next fabrication step. Another advantage of a-ZnO buffer layer is that it can be deposited using the same target in the sputtering tool just by keeping the substrate at room temperature during buffer layer deposition. Further experimental study is required to optimize the thickness of a-ZnO buffer layer.

Study concerning the band offset and the Fermi level position at the interface of ZnO/Si is also necessary, since charge transfer and recombination activity depend on these factors [14]. Jaramillo et al. have recently related conductive oxide/Si interface with metal/Si Schottky junction in terms of Fermi level pinning [130]. Using electronic transport and atom-probe tomography, they have demonstrated that the Fermi level is pinned in the lower half of the Si bandgap at ZnO:Al/SiO₂/Si Schottky junction. The carrier concentration in the ZnO:Al layers was varied by 2 orders but the Schottky barrier height remained constant. It is hypothesized that the observed Fermi level pinning is linked with the insulator-metal transition in doped ZnO, and ZnO/Si barrier height could be tuned by employing kinetic and/or electrostatic control of the interface during ZnO:Al growth to overcome the thermodynamic driving force for segregation of Al.

Etching of the surface oxide of Si in aqueous HF solution has a pivotal role in fabrication of solar cell and many other devices. Although, HF etching of the Si surface is known to produce H-terminated surface but H-termination on chemical reaction of HF with SiO_x is not intuitive. Silicon oxide removal by HF leads to F-Si bond formation which is one of the strongest bond (~6 eV) known in chemistry [140]. Michalak et al. showed that it is possible to prepare F-Si surface with up to 30% F monolayer by controlling the immersion time in HF [141]. Similarly, they achieved ~30% OH-Si termination by immersion of F-Si surface in water without oxidation of the underlying Si wafer. They proved that the availability of OH-Si sites without an underlying oxide helps in atomically smooth junction formation between Si and other materials. When we immersed the Si wafers in HF for several minutes (instead of 10 seconds) and then rinsed with DI water, it improved the V_{OC} by 4–7 mV of, not all but, several samples. The experimental study of

surface chemistry during HF removal of surface oxide can also improve the n-ZnO/p-Si solar cell performance.

6.4.2 Effect of Buffer Layer Thickness

In chapter 1, it was mathematically proved that the recombination at the hetero-interface depends mainly on the interface recombination velocity of holes (Eq. 1.1), and the ideality factor (A) depends on material parameters (Eq. 1.3). In order to have ideality factor small and V_{OC} large, n-doping concentration in ZnO must be much larger than p-doping concentration in Si. The thickness of the buffer layer also impacts the solar cell parameters specially ideality factor and activation energy (E_A). The direct influence of buffer layer thickness (d_b) on A and E_A is given as [27]

$$\frac{1}{A} = 1 - d_b \left(d_b^2 + \frac{\varepsilon_b N_{D,b} d_b^2}{\varepsilon_a N_{A,a}} + \frac{2\varepsilon_b^2}{q\varepsilon_a N_{A,a}} (V_{bi} - V_{OC}) \right)^{-\frac{1}{2}} \quad (6.1)$$

$$\begin{aligned} E_A &= A(E_{g,a} + \Delta E_C^{a,b} + \Delta E_C^{b,w} - qV_{OC} + \frac{q^2 N_{D,b} d_b^2}{2\varepsilon_b} + \frac{q^2 \varepsilon_a N_{A,a} d_b^2}{\varepsilon_b^2} \\ &\quad - \frac{q^2 \varepsilon_a N_{A,a} d_b}{\varepsilon_b^2} \sqrt{d_b^2 + \frac{\varepsilon_b N_{D,b} d_b^2}{\varepsilon_a N_{A,a}} + \frac{2\varepsilon_b^2}{q\varepsilon_a N_{A,a}} (V_{bi} - V_{OC}) + qV_{OC}} \\ &= \frac{E_{g,a} + \Delta E_C^{a,b} + \Delta E_C^{b,w} - qV_{OC} + \frac{q^2 N_{D,b} d_b^2}{2\varepsilon_b} + \frac{q^2 \varepsilon_a N_{A,a} d_b^2}{\varepsilon_b^2}}{1 - d_b \left(d_b^2 + \frac{\varepsilon_b N_{D,b} d_b^2}{\varepsilon_a N_{A,a}} + \frac{2\varepsilon_b^2}{q\varepsilon_a N_{A,a}} (V_{bi} - V_{OC}) \right)^{-\frac{1}{2}}} \\ &\quad - \frac{q^2 \varepsilon_a N_{A,a} d_b}{\varepsilon_b^2} \frac{d_b^2 + \frac{\varepsilon_b N_{D,b} d_b^2}{\varepsilon_a N_{A,a}} + \frac{2\varepsilon_b^2}{q\varepsilon_a N_{A,a}} (V_{bi} - V_{OC})}{\left(\sqrt{d_b^2 + \frac{\varepsilon_b N_{D,b} d_b^2}{\varepsilon_a N_{A,a}} + \frac{2\varepsilon_b^2}{q\varepsilon_a N_{A,a}} (V_{bi} - V_{OC})} \right) - d_b} + qV_{OC}. \end{aligned} \quad (6.2)$$

Where the subscripts a , b and w represent absorber, buffer layer and window respectively. Absorber and window are Si and ZnO in our case. The q is elementary charge and ε is the permittivity of material which includes the relative permittivity and electric permittivity of free space. N_D , N_A , V_{bi} and E_g represent n-type doping density, p-type doping density, built-in voltage and bandgap of Si, respectively.

Once A and E_A are known, the saturation current density J_0 and reference current density $J_{0,r}$ can be determined as

$$J_0 = qS_p N_{V,a} e^{\left(\frac{E_{n,w}}{kT} - \frac{E_A}{AkT}\right)} \quad (6.3)$$

$$J_{0,r} = qS_p N_{V,a} e^{\left(\frac{E_{n,w}}{kT}\right)} \quad (6.4)$$

After experimental determination of V_{OC} , additional information about the device characteristics can be obtained by means of analytically determined equations for the recombination parameters A and E_A .

6.5 Summary

We have prepared n-ZnO/p-Si heterojunction solar cells using three different materials (AlN, a-Si and a-ZnO) at the interface as the buffer layer to reduce recombination velocity as well as avoid oxide formation during ZnO deposition at higher temperature. The use of a-ZnO at the interface produced best V_{OC} up to 359 mV under 1-sun measured by suns- V_{OC} system to avoid the effects of series resistance. It was found that wafer selection and surface treatment of the wafer also significantly affected the performance of the finally fabricated device. Furthermore, the additional advantage of ZnO as an antireflection coating was experimentally verified for different thicknesses of ZnO film. Also, the influence of buffer layer thickness on the solar cell parameters was mathematically described. Fermi level pinning is still the main challenge to be addressed to improve the

V_{OC} and efficiency of n-ZnO/p-Si heterojunction solar cells. Once this problem is solved, it will considerably help to fabricate practically feasible ZnO/Si heterojunction solar cells and also to improve the performance of other electronic and optoelectronic devices based on the heterojunction between ZnO and Si.

CHAPTER 7: FURTHER SIMULATIONS FOR POTENTIAL IMPROVEMENT IN THE SOLAR CELL PERFORMANCE

7.1 Introduction

In this chapter, we present the influence of bandgap and/or electron affinity tuning of zinc oxide on the performance of n-ZnO/p-Si single heterojunction photovoltaic cell. The effects of valence-band and conduction-band off-set engineering on the V_{OC} , J_{SC} , FF, and overall conversion efficiency (η) have been investigated using PC1D software. The simulations reveal that the open circuit voltage and fill factor can be improved significantly by optimizing valence-band and conduction-band off-sets by engineering bandgap and electron affinity of zinc oxide. The overall conversion efficiency of more than 20.3% can be achieved without additional cost or any change in device structure. It has been found that the improvement in efficiency is mainly due to increased band bending resulting in higher open circuit voltage.

Bifacial solar cells offer the advantage of harvesting the sunlight more effectively. In this chapter, simulation is performed to critically investigate the potential of n-ZnO/p-Si structure as a bifacial solar cell. Simulation results indicate that the bifacial n-ZnO/p-Si solar cells are insensitive to the emitter layer thickness up to $1\mu\text{m}$ whereas Si solar cell performance severely degrades. Further, emitter doping concentration of ZnO in Si solar cells shows stable efficiency up to 10^{19} cm^{-3} and drops rapidly for higher doping concentration. In addition to this, simulation of ZnO/Si solar cells with doped back surface field (BSF) and charge passivated BSF is explored. For solar cell thickness of $140\ \mu\text{m}$ for

both types of solar cells, efficiency is almost same. But with higher carrier lifetime wafers, efficiency of charge passivated n-ZnO/p-Si solar cells leads. Similarly, higher V_{OC} and J_{SC} are observed. For charge passivated BSF solar cells, charge density of 10^{12} cm^{-2} is required for higher efficiency and V_{OC} is almost 15 mV higher than doped BSF ZnO/Si solar cell with carrier lifetime of 100 μs .

7.2 Optimization of Bandgap and Electron Affinity of Zinc Oxide for n-ZnO/p-Si Heterojunction Solar Cell

7.2.1 Background

Apart from several other properties which make ZnO a unique wide bandgap material, its bandgap and electron affinity can be tuned over a large range by doping or alloying. Recently, nickel (Ni) doped ZnO thin films were prepared by spray pyrolysis and an optical bandgap decrease from 3.47 eV for the undoped ZnO film to 2.87 eV for 15% Ni doping was achieved [142]. In 2010, Mayer et al. demonstrated that the bandgap of ZnO prepared by pulsed laser deposition can be narrowed down to 2 eV by Se incorporation [143]. Later, the same research group reported effects of growth parameters on electron affinity of ZnO [144]. Also, there are reports available demonstrating significant reduction in conduction band offset (or electron affinity) by incorporating magnesium (Mg) in ZnO [81]. In chapter 4, it was anticipated that the overall conversion efficiency of 19% and fill factor of 81% can be achieved using the n-ZnO/p-Si SHJSC. Here, we predict that the overall conversion efficiency of more than 20.3% can be achieved by optimizing conduction and valence band offsets without additional cost or any change in device structure.

We have prepared ZnO thin films by RF sputtering and have performed detailed characterization. The experimental details were given in chapter 3. The photoluminescence and absorption measurements performed in our labs showed bandgap value of 3.27 eV

which was used in the simulation. The most common value of electron affinity (4.5 eV) provided in literature was used initially. The absorption spectrum of ZnO of thickness ~ 0.5 μm measured in our lab was used in the simulation to investigate the effect of electron affinity. The details of the n-ZnO/p-Si solar cell modeling, structure schematic, and other optimized parameters for PC1D were included in chapter 4.

7.2.2 Results and Analysis

Figure 7.1 illustrates improvement in efficiency with reduction in electron affinity of ZnO. It is obvious that the conversion efficiency exceeds 20% by lowering electron affinity to 4.3 eV. The simple reason behind this phenomenon is reduction in conduction band offset (see Fig. 5.1) that leads to a decrease in the dark current. In other words, when a barrier for majority carrier electrons is formed by conduction band offset, it increases the probability of recombination via interface defects by Shottky-Read-Hall (SRH) mechanism. The maximum efficiency of 20.34% can be achieved with ZnO having bandgap of 3.27 eV and electron affinity of ~ 4.1 eV. Further reduction in electron affinity deteriorates the cell efficiency. This can be theoretically confirmed by band-bending diagram of ZnO/Si junction as shown in Fig. 7.2. Since the electron affinity of Si is ~ 4.05 eV, the electron affinity of ZnO below this value results in formation of a spike in the conduction band of n-ZnO region. This spike acts as a potential barrier and blocks electron flow from p-Si to n-ZnO region. Therefore, it is difficult for p-Si region to contribute in the photocurrent. This reasoning is supported by Fig. 7.3 that depicts significant increase in V_{OC} with reduction in electron affinity. A negligible increase in J_{SC} can be attributed to the same reason.

The efficiency of the solar cell alters by modifying the bandgap as well. Change in conversion efficiency with bandgap value of ZnO is shown in Fig. 7.4 for three different values of electron affinity. The absorption spectrum was altered for values of bandgap other than 3.27 eV to get realistic results. The efficiency increases by decreasing the bandgap (or valence-band off-set). This improvement in efficiency cannot be explained by band-bending diagram based on the famous Anderson's rule which ignores the effects of chemical bonding. The chemical bonding or electrical polarization due to interface states can alter the band bending significantly. Figure 7.4 also illustrates that the efficiency reduces significantly below a certain bandgap value. It is predictable because a considerable part of solar spectrum gets absorbed in ZnO for such a small bandgap value. The ZnO layer is much thinner ($0.5\ \mu\text{m}$) than Si ($160\ \mu\text{m}$) but it has a higher absorption coefficient due to direct bandgap of ZnO.

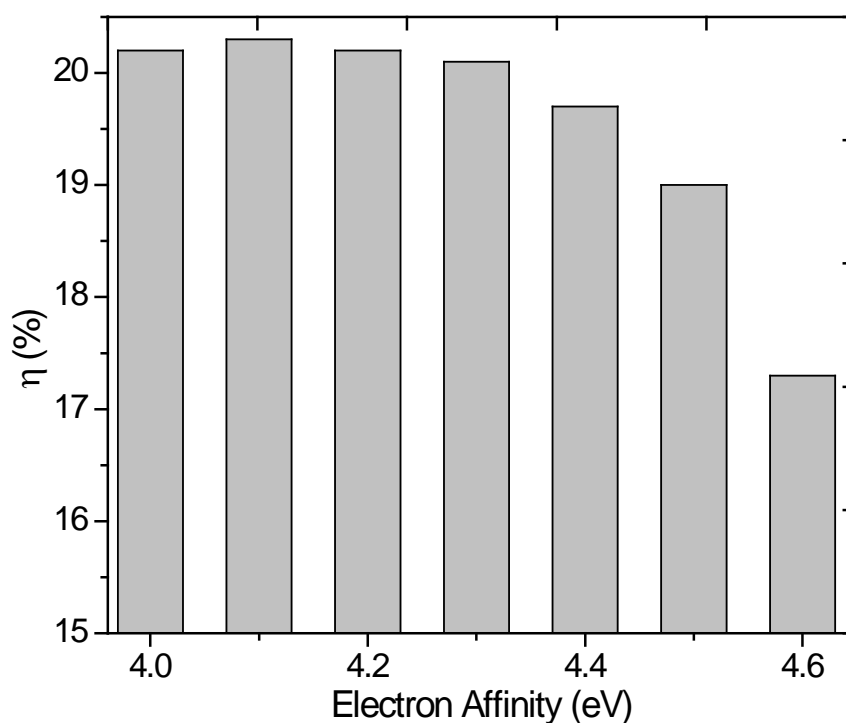


Fig. 7.1. Influence of electron affinity of ZnO (bandgap: 3.27 eV) on the efficiency of n-ZnO/p-Si heterojunction solar cell.

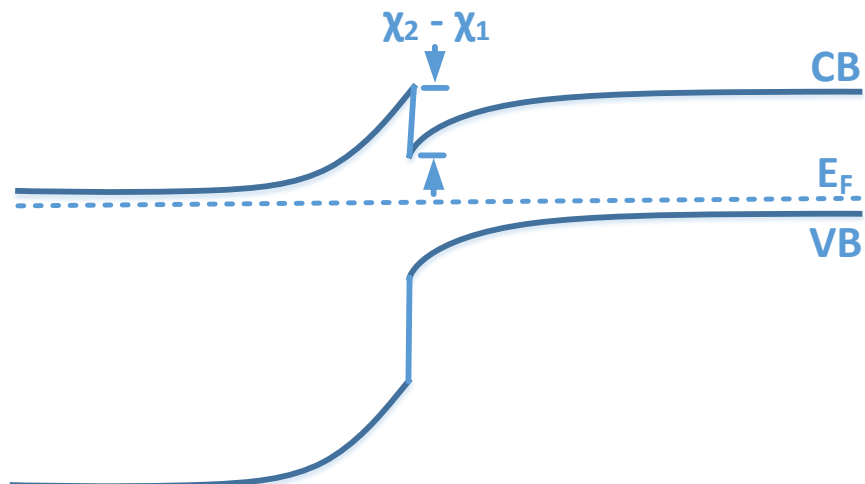


Fig. 7.2. Schematic of the band-bending when electron affinity of ZnO (χ_1), at left, is lower than that of Si (χ_2), at right. CB: conduction band, VB: valence band, E_F : fermi level.

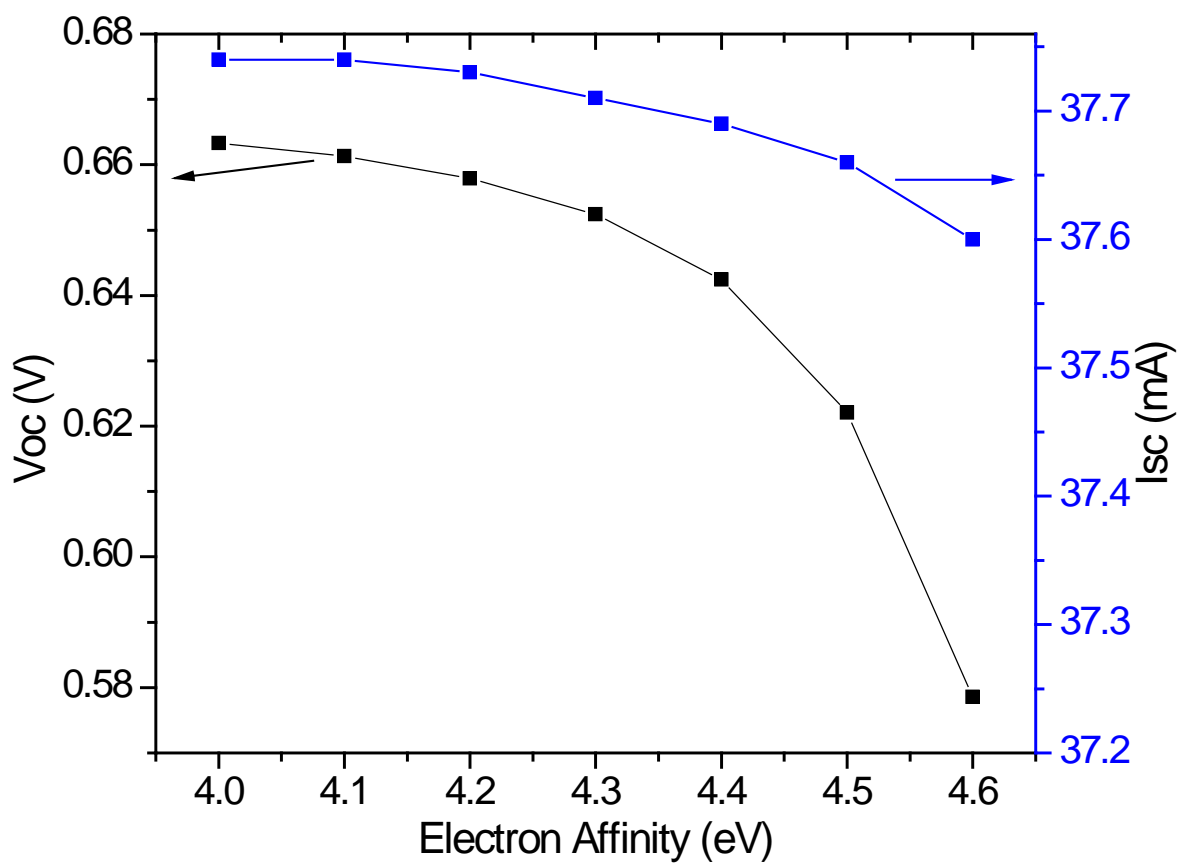


Fig. 7.3. Effect of electron affinity of ZnO (bandgap: 3.27 eV) on the V_{oc} and I_{sc} of n-ZnO/p-Si solar cell.

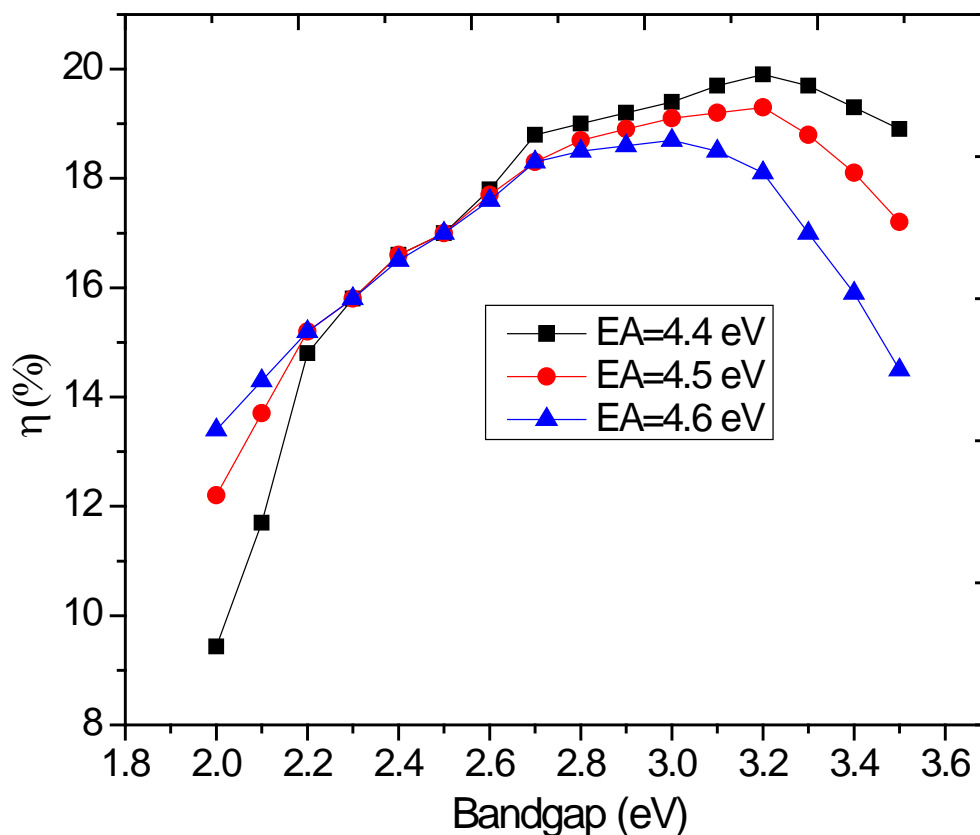


Fig. 7.4. Change in overall conversion efficiency of n-ZnO/p-Si solar cell with modification of bandgap value of ZnO for three different values of electron affinity (EA). Few data points have been interpolated because numerical solution was not converging for those points in PC1D.

It is evident from the simulation results that the open circuit voltage of n-ZnO/p-Si single heterojunction solar cell can be significantly improved by tuning bandgap and/or electron affinity of ZnO by doping or alloying. The major reason of improvement in the solar cell efficiency is enhanced band-bending due to decrease in conduction-band offset which increases built-in voltage. The best values achieved for open circuit voltage, short circuit current density, fill factor, and conversion efficiency are 0.662 V, 37.7 mA/cm², 0.815, and 20.34%, respectively, for ZnO having a bandgap of 3.27 eV and electron affinity of 4.1 eV.

7.3 Bifacial n-ZnO/p-Si Single Heterojunction Solar Cells

7.3.1 Simulation Procedure

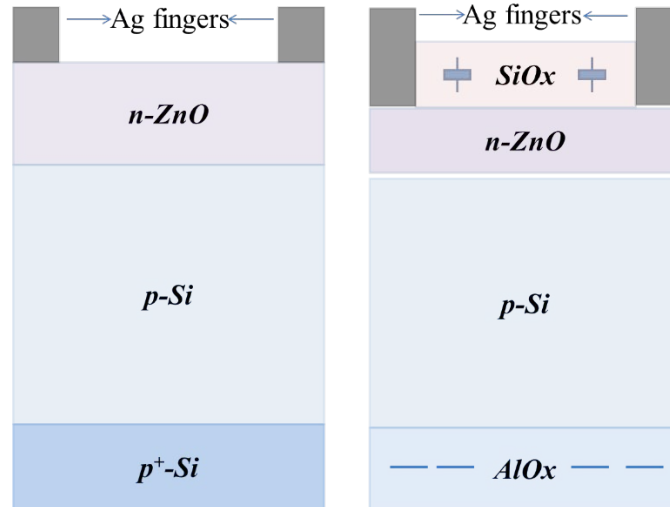


Fig. 7.5. The schematic of two different structures of solar cells using ZnO as emitter layer; doped BSF (left) and front and rear surface charge passivated BSF (right).

TABLE 7.1. List of various parameters used in PC1D simulations.

Material properties	ZnO	Si
Thickness (μm)	0.1 – 1	5 – 150
Doping concentration (cm^{-3})	10^{16} - 10^{20}	1×10^{16}
Carrier lifetime (μs)	10^{-3}	100 - 1000
Back surface field (BSF) thickness (μm)	-	3
BSF doping concentration (cm^{-3})	-	2×10^{19}
Series resistance (Ω)	0.3	
Front and rear surface charge density (cm^2)	$10^6 - 10^{12}$	
Back illumination intensity (mW/cm^2)	30	

In all the simulations, thickness of Si and ZnO are 150 and 0.5 μm respectively. Figure 7.5 displays the schematic of two different structures of solar cells using ZnO as emitter layer; doped BSF (left) and front and rear surface charge passivated BSF (right). A comparison between these two solar cell designs is also explored alongside the advantages of using ZnO as front window layer. Table 7.1 enlists various parameters used in the PC1D

for the simulation of these solar cells. In all the simulations, light is simultaneously shone from the front and rear side and the rear light intensity is kept at 30% of the front illumination (30 mW/cm^2).

7.3.2 Results and Discussion

Figure 7.6 provides the comparison between the ZnO/Si and conventional Si solar cells for varying emitter thicknesses. With increasing emitter thickness, Si solar cells efficiency decreases linearly from $\sim 31\%$ to 26% for emitter thickness of 0.1 to $1 \mu\text{m}$. Whereas, ZnO/Si solar cell efficiency is not a strong function of emitter thickness and efficiency drops only by 1% for the same range of thickness of ZnO emitter as shown in Fig. 7.6 (a). Similarly, V_{OC} of Si solar cells reduces rapidly by 30 mV with emitter thickness as depicted in Fig. 7.6 (b) whereas for ZnO emitter solar cell V_{OC} almost stays constant. Figure 7.7 illustrates the J_{SC} as function of emitter depth. ZnO/Si solar cell shows a drop of 2 mA/cm^2 in J_{SC} whereas in Si solar cell this drop is 6 mA/cm^2 .

The doping concentration of emitters is very crucial apart from thickness. Si solar cells heavily rely on the doping concentration to enhance the light absorption (blue response) and to achieve low contact resistance also depends on emitter doping concentration (N_D). Figure 7.8 illustrates the effect of N_D on ZnO/Si solar cell. To understand the impact of doping concentration on the performance of ZnO based solar cells, simulation is performed over a broad range of N_D : $1 \times 10^{16} - 10^{20} \text{ cm}^{-3}$. It is found that ZnO emitter solar cell efficiency is not prone to the N_D in the range of $10^{16} - 10^{19} \text{ cm}^{-3}$ but efficiency drop is very steep for $N_D > 2 \times 10^{20} \text{ cm}^{-3}$. We attribute this to the fact that ZnO behaves like a metal for such a heavy doping and majority carrier current component becomes very large that degrades the device performance.

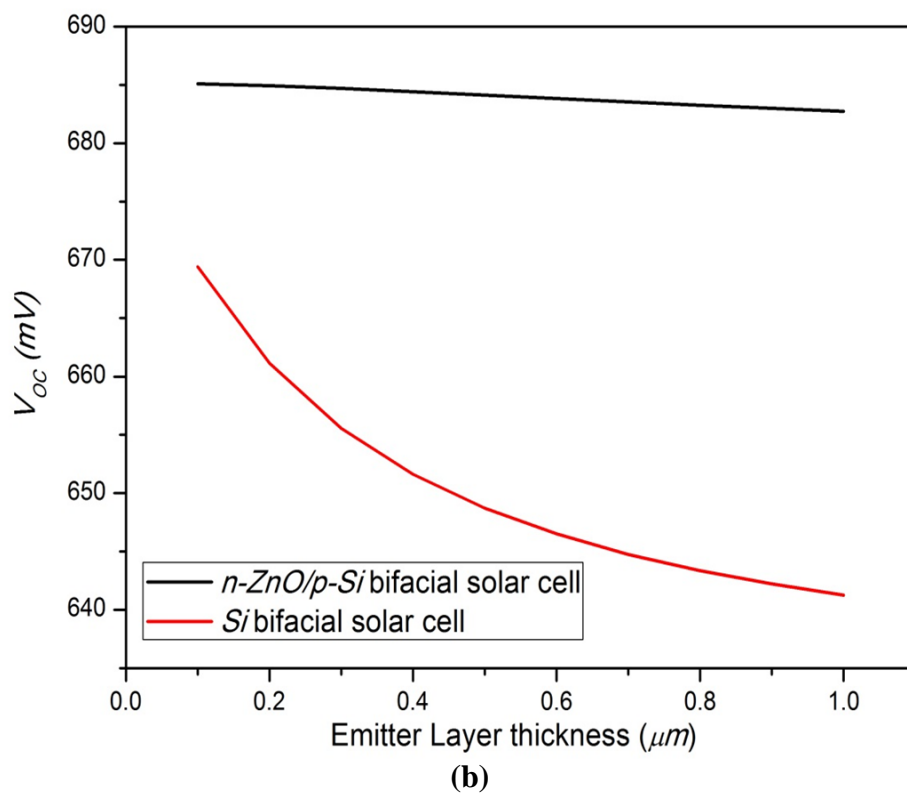
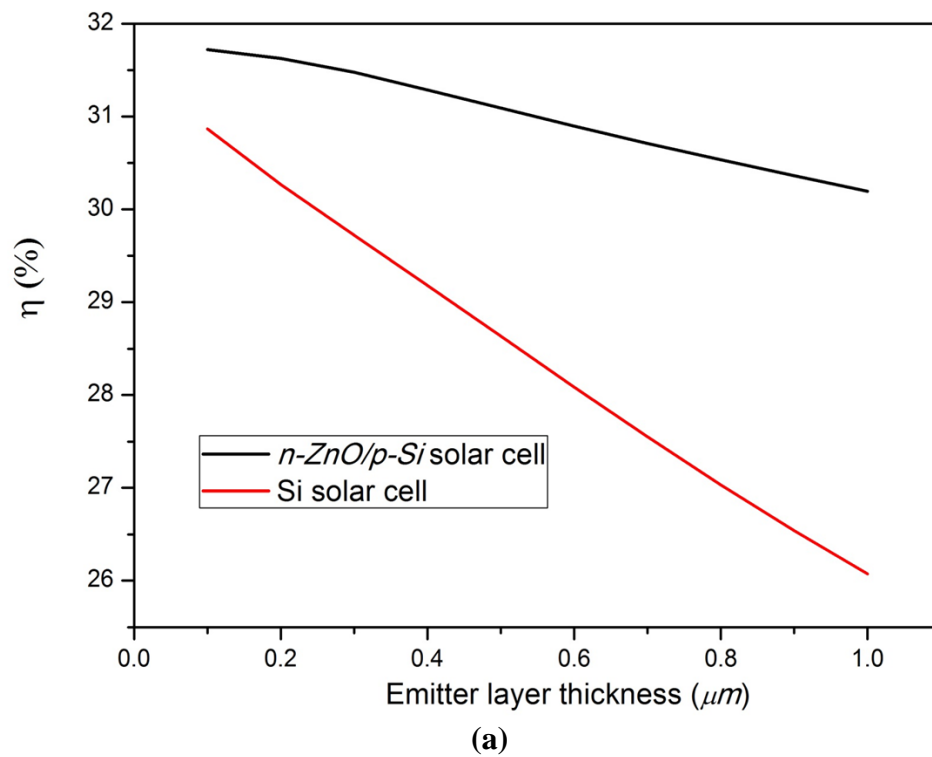


Fig. 7.6. Effect of emitter layer thickness on ZnO/Si and Si based solar cells; (a) efficiency and (b) V_{OC} .

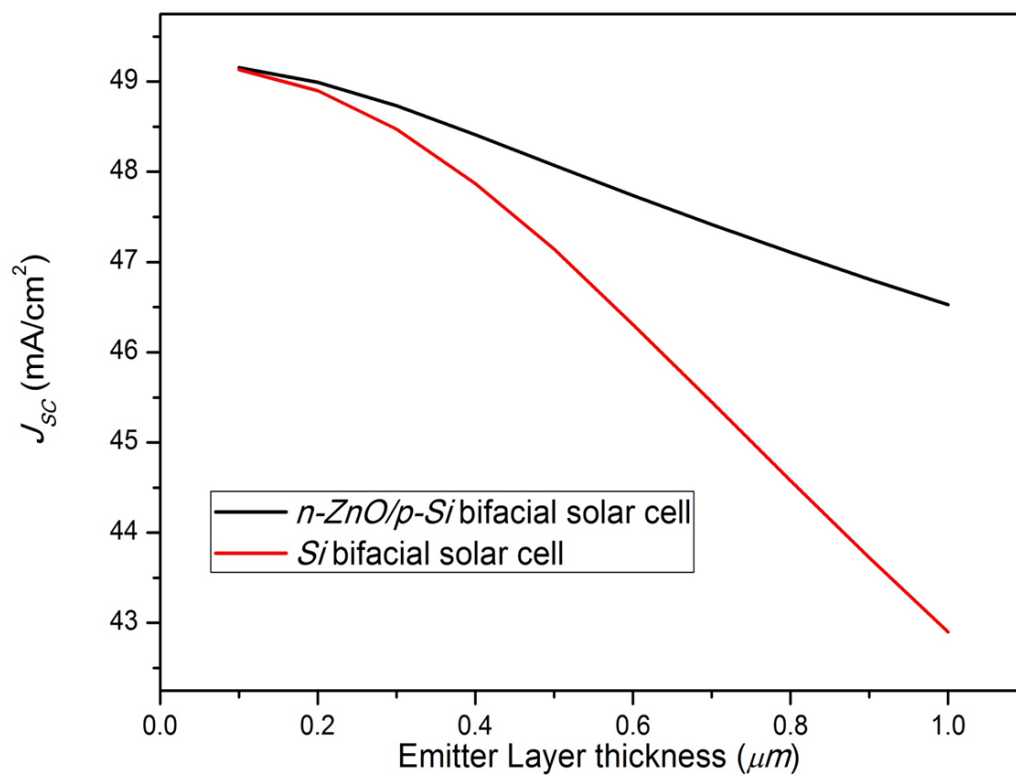


Fig. 7.7. Comparison of J_{sc} as a function of emitter thickness for ZnO/Si and Si solar cells.

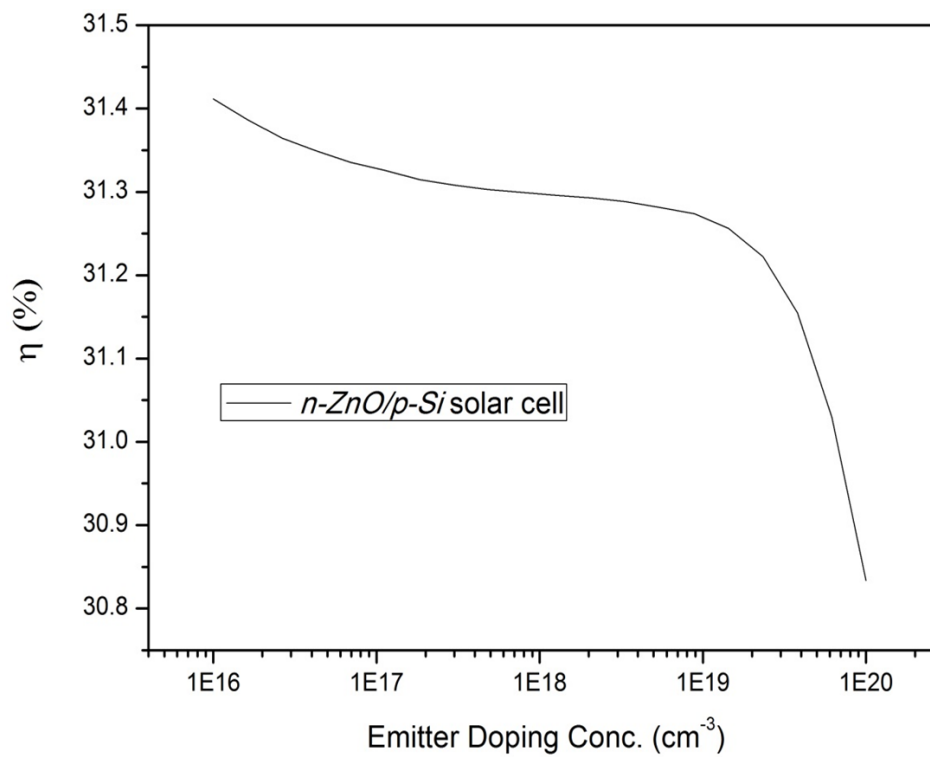


Fig. 7.8. Impact of ZnO doping concentration on the efficiency of bifacial ZnO/Si solar cell.

The BSF formation in current silicon solar cells is accomplished by boron doping or aluminum deposition with subsequent annealing to form few micrometer thick BSF layer that acts as electron reflector and enhances the V_{OC} and efficiency of the Si solar cells. Here we have explored the effect of BSF (doped and charge passivated) coupled with ZnO emitter for the charge passivated BSF. Figure 7.9 displays efficiency as a function of lifetime in front and rear surface passivated BSF ZnO/Si solar cell. The charge density is varied from 10^6 to 10^{12} cm^2 . It can be observed that the efficiency considerably increases with the use of charge passivated BSF specially in the charge density range of 10^{11} – 10^{12} cm^2 .

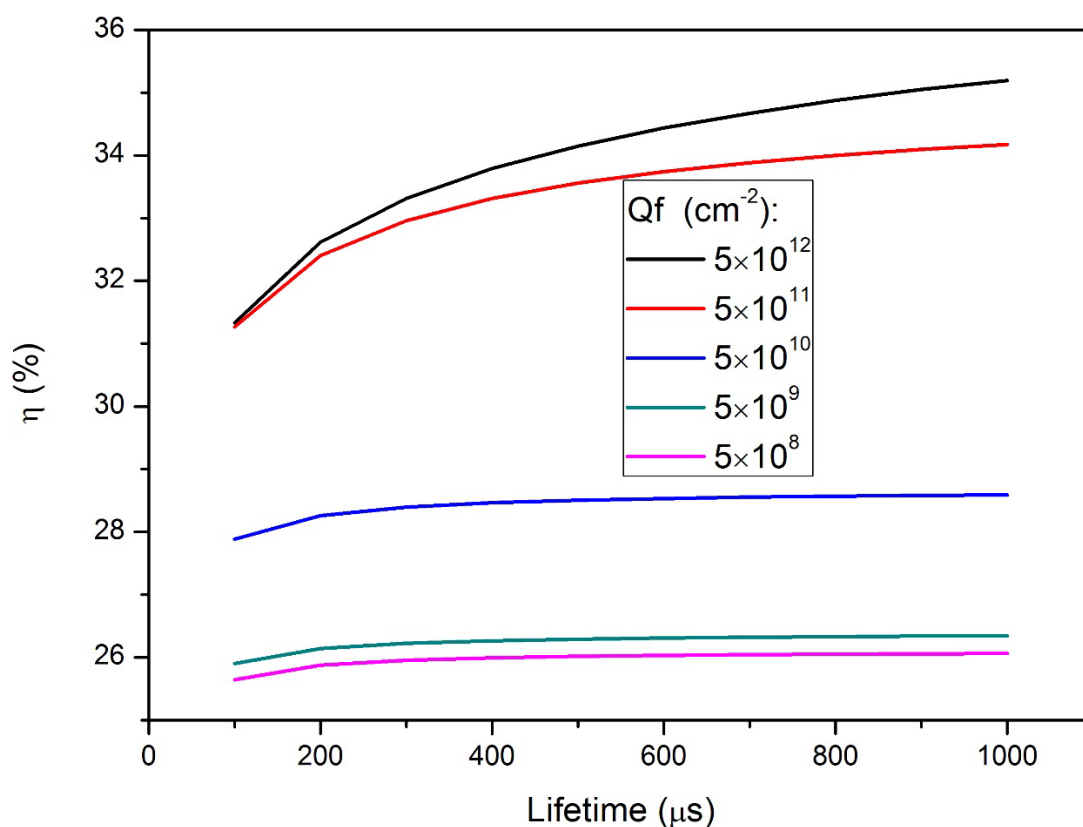


Fig 7.9. Efficiency of charge passivated BSF ZnO/Si solar cell as a function of lifetime.

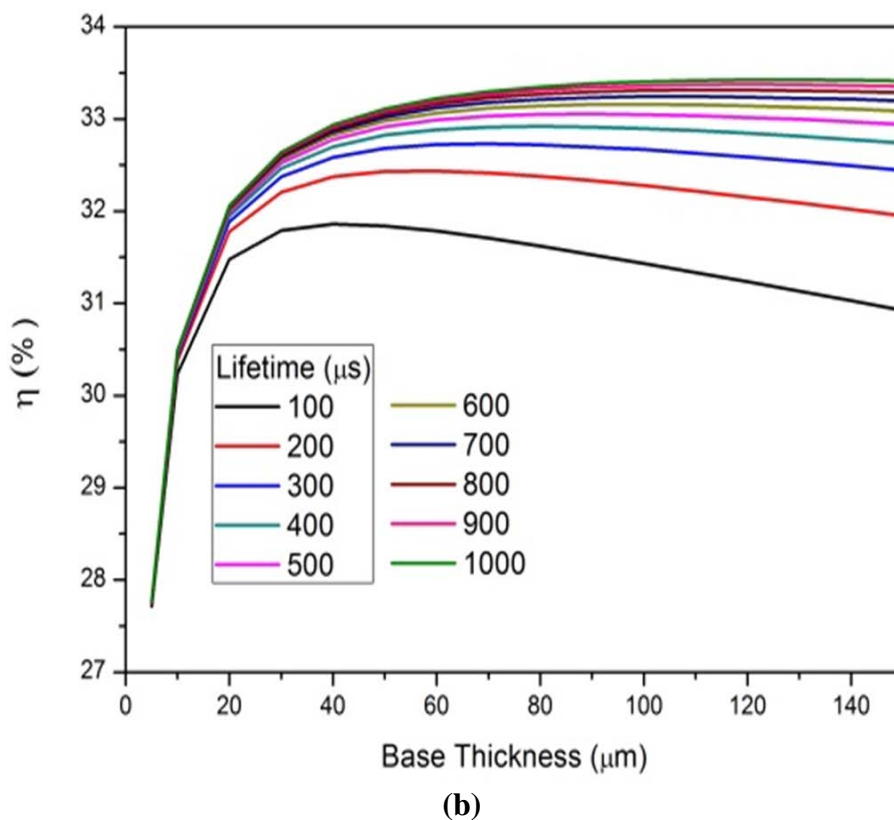
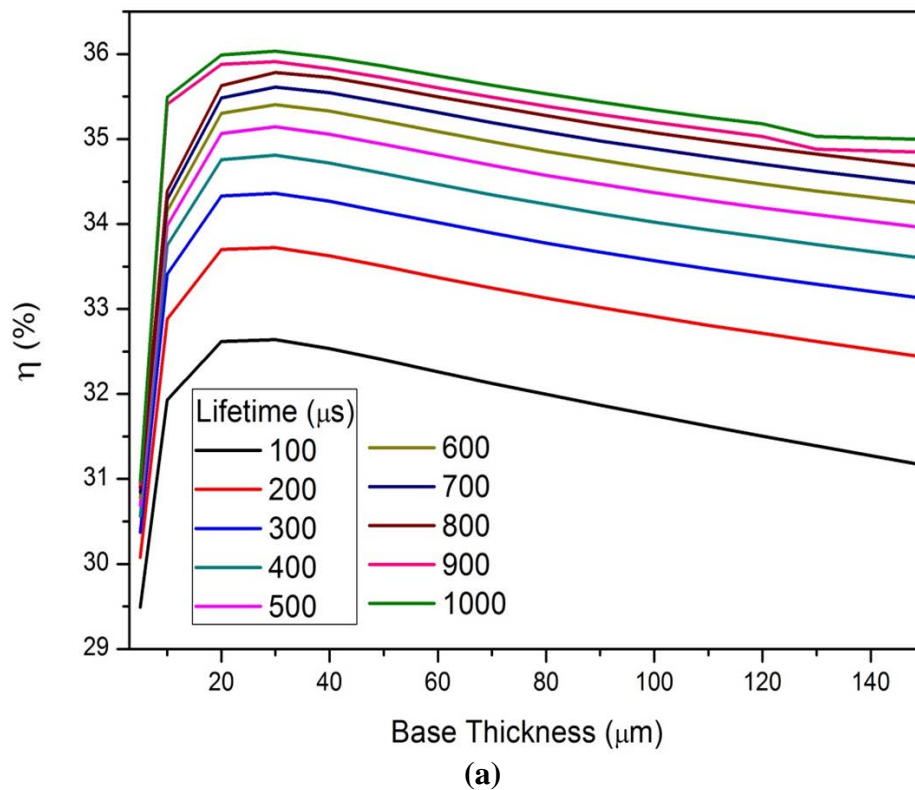


Fig. 7.10. Efficiency of ZnO/Si solar cell with changing base thickness for different lifetimes (a) charge passivated BSF and (b) with doped BSF.

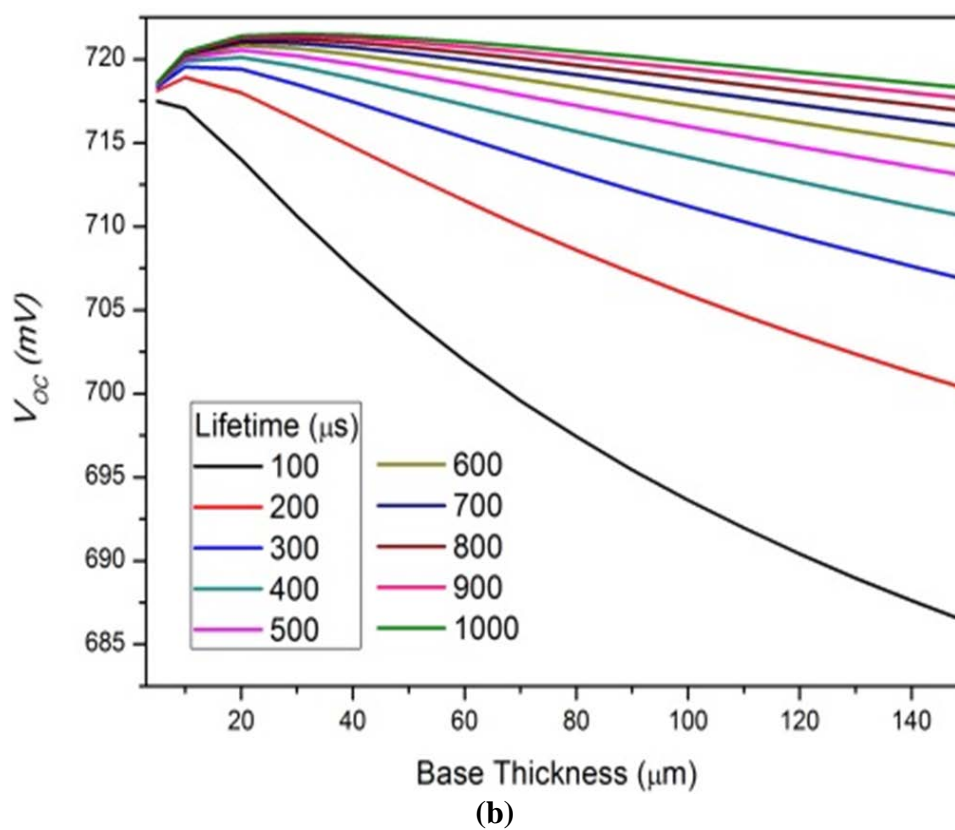
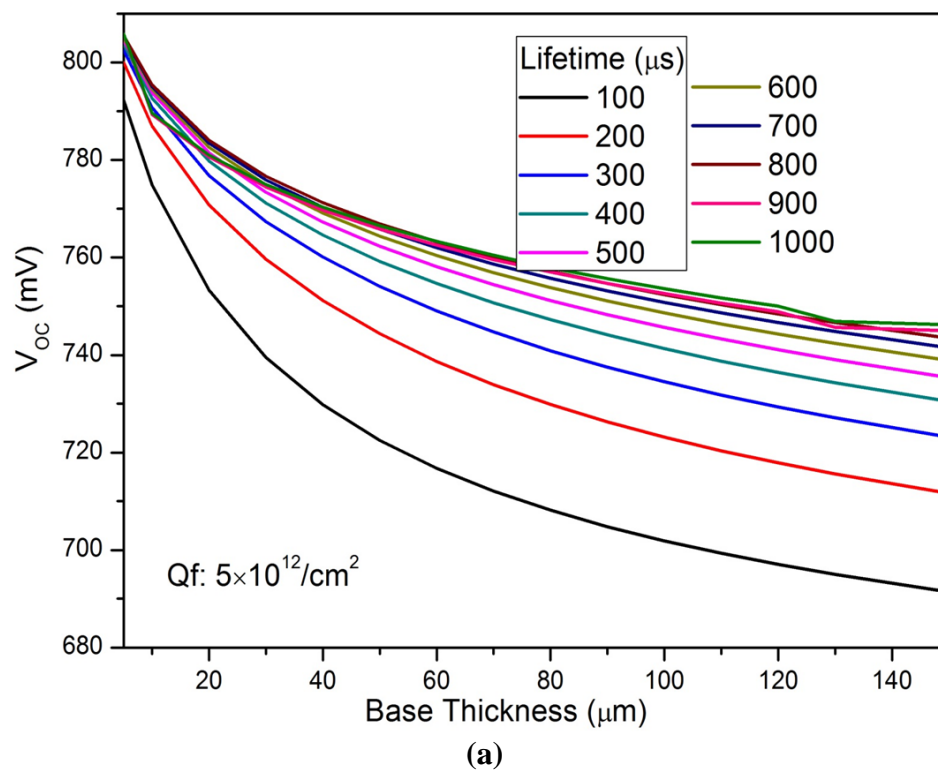


Fig. 7.11. V_{OC} of ZnO/Si solar cell with (a) charge passivated BSF and (b) doped BSF with different lifetimes.

Figure 7.10 provides a comparison in efficiency with thickness for doped and charge passivated BSF for different lifetimes. For low carrier lifetime ($100 \mu\text{s}$) of base materials, efficiency is $\sim 31\%$ for both ZnO/Si solar cells. For higher lifetime base materials, the difference in efficiency becomes appreciable and charge passivated BSF ZnO/Si solar cells dominate in performance. This provides an option that low lifetime materials can be used for the fabrication of solar cells that provides equivalent efficiency to Al-BSF solar cells. The difference in efficiency between these two different BSF solar cells with thickness of $140 \mu\text{m}$ is $\sim 1.5\%$. In addition, for a small thickness of $20 \mu\text{m}$, the efficiency is close to 36% . This shows that the bulk recombination is dominant in this solar cell structure. The efficiency higher than the Shockley-Queisser limit is due to the bifacial structure. Figure 7.11 demonstrates the V_{OC} of doped BSF and charge passivated BSF ZnO/Si solar cells for different lifetimes. For solar cell thickness of $140 \mu\text{m}$ with carrier lifetime $100\mu\text{s}$, V_{OC} difference is 5 mV , but for wafers with higher lifetime, this difference increases to 13 mV .

7.4 Summary

In this chapter, we presented simulations based optimization of bandgap and electron affinity of ZnO to enhance the conversion efficiency of ZnO/Si single heterojunction solar cell. The effects of valence-band and conduction-band off-set engineering on the open circuit voltage, short circuit current density, fill factor, and overall conversion efficiency have been investigated using PC1D software. It is ascertained that the open circuit voltage of n-ZnO/p-Si single heterojunction solar cell can be significantly improved by tuning bandgap and/or electron affinity of ZnO by doping or alloying. The major reason of improvement in the solar cell efficiency is enhanced band-bending due to decrease in conduction-band offset which increases built-in voltage. The best values achieved for open

circuit voltage, short circuit current density, fill factor, and conversion efficiency are 0.662 V, 37.7 mA/cm², 0.815, and 20.34%, respectively, for ZnO having a bandgap of 3.27 eV and electron affinity of 4.1 eV.

Furthermore, PC1D simulations were performed to evaluate the potential of n-ZnO/p-Si bifacial solar cells. Two different structures of ZnO/Si solar cell are simulated one with doped BSF and other with charge passivated BSF. ZnO emitter/Si solar cells showed insensitivity to emitter thickness which is quite influential to the performance of conventional Si solar cells. Charge passivated BSF ZnO/Si solar cells showed higher efficiency for high carrier lifetime base materials in comparison to doped BSF and for low lifetime base materials, charge passivated BSF cells are equivalent in efficiency to doped BSF ZnO/Si solar cells.

CHAPTER 8: CONCLUSIONS

In this dissertation, I have documented the work related to study and development of n-ZnO/p-Si single heterojunction solar cell (SHJSC) as a potential viable substitute of the conventional pn homojunction Si solar cell. The heterojunction solar cell seems to be one of the few practical applications of ZnO because of well-known p-doping issue with this material. ZnO can be deposited at much lower temperature that can reduce degradation in carrier lifetimes, a common problem in high temperature diffusion of phosphorous using POCl₃ or implantation. The front n-type ZnO layer of the p-n junction acts as antireflection coating due to its close refractive index match with the ideal value. This prevents requirement of additional antireflection coating which can reduce fabrication cost. Furthermore, the work function of Ag is less than electron affinity of ZnO. Consequently, there is no barrier at Ag-ZnO interface and the contact at front surface will be ohmic which can further increase the device performance. Additionally, ZnO is more resistant to radiation damage as compared to indium tin oxide (a commonly used material for AR coating) because of its stable crystal structure which inhibits UV degradation and ensures longevity of the device.

The first chapter of this dissertation discussed background of heterojunction solar cells, importance of ZnO and previous work reported on n-ZnO/p-Si SHJSC. The chapters 4 and 7 dealt with modeling and simulation based results related to design and optimization of n-ZnO/p-Si SHJSC. The chapters 2 and 3 included experimental details related to growth and characterization of ZnO using MOCVD and sputtering, and optimization of parameters. In

chapters 5 and 6, discussion of fabrication and characterization of n-ZnO/p-Si SHJSC device with and without a buffer layer was provided.

The performance of every type of electronic or optoelectronic device including photovoltaic cell primarily depends on the progress in material technology related to the device. The n-ZnO/p-Si SHJSC involves two semiconducting materials Si and ZnO. The Si is already a well-established material with optimized growth techniques and well-known parameters. The ZnO growth techniques still lack precise optimization with reference to specific applications. Therefore, we have prepared numerous ZnO thin film samples using two popular semiconductor film growth techniques MOCVD and sputtering. Iterative growth and characterization of ZnO thin films were carried out to optimize the growth parameters using both deposition techniques. The samples were evaluated by structural characterization using XRD, SEM and AFM, optical characterization using PL, transmission and interferometric spectral reflectance, and electrical characterization using Hall and 4-probe measurements. It was concluded that MOCVD based ZnO thin films grown at a temperature of 550 °C, rotation of 800 rpm, and VI/II ration of 330 demonstrate the best crystal quality. Similarly, the optimized RF power and deposition temperature for sputtered samples were 180 W and >300 °C respectively.

Thickness uniformity of the film is an important parameter because thickness directly affects physical properties of the single- or multi-layer structure and thus performance of the device. Also, it plays an important role in sample evaluation especially in electrical characterizations like Hall and 4-probe measurements because thickness is a fundamental factor which is used to calculate carrier concentration, lifetime, resistivity, and mobility of the sample. We have experimentally observed that uniformity in thickness distribution over

the surface of ZnO films prepared by sputtering is better than the films produced by the homemade MOCVD system available in our Lab. The PL measurements revealed that crystal quality of the films sputtered at 300 °C is better than the films grown by MOCVD even grown at higher temperature on same substrate material. The high temperature processing of samples can degrade the quality of substrate and thus performance of the device. This is specifically applicable to ZnO/Si heterojunction solar cell because high temperature causes solar cell performance degradation mainly correlated with oxygen precipitation. Also, there is a direct relation between spatial thickness uniformity and solar cell performance. There are some additional advantages associated with sputtering as compared to MOCVD. It is possible to implement shadow-mask lithography in sputtering if ZnO (or any other material) needs to be deposited on selected areas. Also, source vapors can penetrate below the substrate in case of MOCVD causing unwanted growth of material at back side of substrate where this is not possible in sputtering. Although, it is well known that MOCVD produces thin films exhibiting overall better quality than sputtered samples but this is not the case in our experimental observations probably because our MOCVD system is not a well calibrated commercial unit. These experimental finding helped us to select sputtering as main growth technique for ZnO growth.

Mathematical modeling was used to prove the feasibility of ZnO as electrically active n-layer as well as antireflection coating and to find the optimized thickness of ZnO layer to reduce the reflection to minimum level. The simulations were performed using modified PC1D software taking practical constraints into account. Electrical and optical characteristics as well as internal and external quantum efficiencies were investigated by varying different key parameters. The measured absorption spectrum of the ZnO thin films

grown in our Lab was used in PC1D simulations in order to get more realistic results of the model. The optimum thickness computed by PC1D was around $0.1 \mu\text{m}$ which has sheet resistance of $\sim 500 \Omega/\text{sq}$. Such a high sheet resistance requires narrow finger spacing for the solar cell. Therefore, we recommend using thicker layer ($\sim 0.5 \mu\text{m}$) that will allow wider finger spacing and reduction in shadowing effect. It will still reduce the reflection significantly due to interference effect after reflection from front and back face of ZnO film. The thickness of the ZnO film should be precisely controlled in this case to make back-face-reflected light able to destructively interfere with front-face-reflected light. The best values of I_{SC} , V_{OC} , conversion efficiency, and fill factor were predicted as 37.7 mA, 0.6221 V, 19.0% respectively for n-ZnO/p-Si solar cell without optimizing conduction and valence band offsets. The simulation results proved that ZnO can be used with Si to fabricate efficient, durable, and cost effective heterostructure solar cells.

Initial n-ZnO/p-Si SHJSC device was fabricated by depositing ZnO on p-Si substrates using RF magnetron sputtering and making front and back metal contacts by e-beam evaporation using handmade shadow masks. The electrical characterization of the n-ZnO thin films was carried out by Hall measurements which revealed that inherent doping level of n-ZnO films is fortunately close to the value ($\sim 10^{18} \text{cm}^{-3}$) optimized for the solar cell by PC1D modeling, but the resistivity of the films is too high to evaluate samples using I-V characterization. Therefore, suns- V_{OC} measurements were made to circumvent effects of series resistance. Several samples were fabricated and measured to validate the experimental value of V_{OC} because there are discrepancies in the measured value of V_{OC} of n-ZnO/p-Si SHJSC in the literature. We obtained a repeatable value of V_{OC} of 260 mV which is very close to the value reported in literature by other researchers. This value is

much lower than theoretical value of $>600\text{mV}$ predicted by PC1D simulations based on band bending between n-ZnO and p-Si. The possible reasons and potential solutions of the lower experimental value of V_{OC} were discussed.

Our undoped ZnO samples have a bandgap around 3.27 eV ($\sim 380\text{ nm}$). According to ASTM G-173 spectra provided by NREL, around 10% “intensity” of solar spectrum lies below this wavelength. Since absorption coefficient of ZnO is on the order of 10^5 cm^{-1} , the absorption length is around 100 nm . Therefore, most of the UV portion of solar radiation would be absorbed in 100 nm thick ZnO layer without contributing in photogeneration current. Therefore, Ga-doped ZnO films were prepared to study bandgap tuning of ZnO to utilize maximum possible energy of the solar spectrum. The bandgap was blue-shifted by about 105 meV (12 nm) due to Burstein-Moss effect in which effective bandgap of a heavily doped semiconductor is increased as the absorption edge in conduction band moves to higher energies because all states close to the conduction band edge are filled.

The main reason behind the difference between theoretically predicted and practically achieved conversion efficiency of n-ZnO/p-Si HJSC is that experimental V_{OC} is much lower than the predicted value of V_{OC} ($\sim 650\text{ mV}$) based on band-bending between n-ZnO and p-Si. This lower value of V_{OC} is attributed to fermi level pinning at the hetero-interface due to interface states probably resulting from lattice mismatch between ZnO and Si. The use of a thin buffer layer at the interface is proved to be one of the best solutions to reduce interface states and recombination velocity. We achieved $>20\%$ improvement in V_{OC} of n-ZnO/p-Si HJSC by simply depositing amorphous-ZnO (a-ZnO) at the interface of crystalline ZnO (c-ZnO) and Si. Two other materials, amorphous-Si (a-Si) and aluminum nitride (AlN) were also deposited as a buffer layer (BL) between c-ZnO and Si-wafer. But

the best V_{OC} was achieved for the device having a-ZnO at the interface. The improvement in V_{OC} is probably due to elimination/reduction in SiO_x formation at the interface of c-ZnO and Si-wafer, and/or reduction in the interface states. The best value of 359 mV of V_{OC} was achieved using n-ZnO/BL/p-Si solar cell structure under 1-sun. Also, it was found out that wafer selection and surface treatment of the wafer also significantly affect the performance of the finally fabricated device. Furthermore, additional advantage of ZnO as an antireflection coating was experimentally verified for different thicknesses of ZnO film. Also, the influence of buffer layer thickness on the solar cell parameters was mathematically described.

Finally, we presented the influence of bandgap and/or electron affinity tuning of zinc oxide on the performance of n-ZnO/p-Si single heterojunction photovoltaic cell. The effects of valence-band and conduction-band off-set engineering on the V_{OC} , J_{SC} , fill factor (FF), and overall conversion efficiency (η) were investigated using PC1D software. The simulations revealed that the open circuit voltage and fill factor can be improved significantly by optimizing valence-band and conduction-band off-sets by engineering bandgap and electron affinity of zinc oxide without additional cost or any change in device structure. It was found out that the improvement in efficiency is mainly due to decreased conduction band offset resulting in reduced recombination at the interface. The best values achieved for V_{OC} , I_{SC} , FF, and η are 0.662 V, 37.7 mA/cm², 0.815, and 20.34%, respectively, for ZnO having a bandgap of 3.27 eV and electron affinity of 4.1 eV. Furthermore, simulations were performed to evaluate the potential of n-ZnO/p-Si bifacial solar cells. Two different structures of ZnO/Si solar cell are simulated one with doped BSF and other with charge passivated BSF. ZnO emitter/Si solar cells showed insensitivity to

emitter thickness which is quite influential to the performance of conventional Si solar cells. Charge passivated BSF ZnO/Si solar cells showed higher efficiency for high carrier lifetime base materials in comparison to doped BSF and for low lifetime base materials, charge passivated BSF cells are equivalent in efficiency to doped BSF ZnO/Si solar cells.

Fermi level pinning is still the main challenge to address to improve the V_{OC} and efficiency of n-ZnO/p-Si heterojunction solar cells. Once this problem is solved, it will considerably help to fabricate practically feasible ZnO/Si heterojunction solar cell and also to improve the performance of other electronic and optoelectronic devices based on heterojunction between ZnO and Si. Besides, ZnO has many other applications in optoelectronics devices. It is a cheap and environmentally friendly material and can be used for coatings, transparent conducting oxides, UV emitters and detectors, high-speed and high-power electronics and many other devices. The progress in n-ZnO/p-Si SHJSC will produce useful knowledge about the hidden features and potential benefits of ZnO for other applications as well.

There is tremendous potential for research to overcome the problem of ZnO/Si interface. Once this problem is solved, it can lead to the emergence of a new solar cell technology that can significantly influence the solar cell industry. There are multiple potential solutions to improve the ZnO/Si interface. One possible solution is to find out the suitable material for quantum buffer layer (BL) between ZnO and Si to reduce the lattice mismatch. Titanium nitride (TiN) have a very close lattice match with both ZnO and Si so it can be used to make the solar cell device with improved performance. Magnesium oxide (MgO)/TiN buffer layers can also be incorporated at the interface since TiN has very close lattice match with Si and MgO conforms the ZnO lattice. Depositing amorphous-Si (a-Si)

intrinsic layer to passivate the crystalline-Si (c-Si) surface before deposition of ZnO resulted in improved V_{OC} . It can be useful to do detailed theoretical analysis of the effects of a-ZnO buffer layer at the interface of n-ZnO/p-Si SHJSC and to optimize the thickness of the buffer layer. Another potential solution to improve the hetero-interface could be using electrostatic control of the interface during ZnO growth that may enable the desired control of defect segregation and thereby improving the device performance. But this needs major modifications in the ZnO deposition system. It will also be interesting to use ZnO as front layer in concentrator solar cells. The ZnO front layer will prevent UV degradation of the device which is a common problem in concentrator solar cells.

REFERENCES

1. Gielen, D. *Energy technology perspectives 2008: scenarios and strategies to 2050*. in *IEEJ Workshop*. 2008. Tokyo: International Energy Agency.
2. Birol, F., *World Energy Outlook 2012*. 2012, International Energy Agency.
3. Wikipedia. Available at: (https://en.wikipedia.org/wiki/Growth_of_photovoltaics).
4. Tsokos, K.A., *Physics for the IB diploma*. 5th ed. 2012: Cambridge University Press.
5. Green, M.A., et al., *Solar cell efficiency tables (version 47)*. Progress in Photovoltaics: Research and Applications, 2016. **24**(1): p. 3-11.
6. Green, M.A., *The path to 25% silicon solar cell efficiency: History of silicon cell evolution*. Progress in Photovoltaics: Research and Applications, 2009. **17**(3): p. 183-189.
7. Ohl, R.S., *Light sensitive electric device*. 1941: USA.
8. Kingsbury, E.F. and R.S. Ohl, *Photoelectric properties of ionically bombarded silicon*. Bell System Technical Journal, 1952. **31**(4): p. 802-815.
9. Chapin, D.M., C.S. Fuller, and G.L. Pearson, *A new silicon p-n junction photocell for converting solar radiation into electrical power*. Journal of Applied Physics, 1954. **25**(5): p. 676-677.
10. Wolf, M. *Limitations and Possibilities for Improvement of Photovoltaic Solar Energy Converters: Part I: Considerations for Earth's Surface Operation*. in *IRE*. 1960. El Monte California.
11. Rittner, E.S. and R.A. Arndt, *Comparison of silicon solar cell efficiency for space and terrestrial use*. Journal of Applied Physics, 1976. **47**: p. 2999-3002.
12. Allison, J.F., R.A. Arndt, and A. Meulenberg, *A comparison of the COMSAT Violet and Non-reflective solar cells*. COMSAT Technical Review, 1975. **5**(2): p. 211-224.
13. Green, M.A., A.W. Blakers, and C.R. Osterwald, *Characterization of high-efficiency silicon solar cells*. Journal of Applied Physics, 1985. **58**(11): p. 4402-4408.
14. Schmidt, M., et al., *Physical aspects of a-Si:H/c-Si hetero-junction solar cells*. Thin Solid Films, 2007. **515**(19): p. 7475-7480.

15. De Wolf, S., et al., *High-efficiency Silicon Heterojunction Solar Cells: A Review*, in *green*. 2012. p. 7.
16. Yablonovitch, E., et al., *A 720 mV open circuit voltage SiO_x:c-Si:SiO_x double heterostructure solar cell*. Applied Physics Letters, 1985. **47**(11): p. 1211-1213.
17. Fuhs, W., K. Niemann, and J. Stuke. *Heterojunctions of amorphous silicon and silicon single crystals*. in *American Institute of Physics*. 1974.
18. Pankove, J.I. and M.L. Tarnag, *Amorphous silicon as a passivant for crystalline silicon*. Applied Physics Letters, 1979. **34**: p. 156-157.
19. Hamakawa, Y., et al., *New types of high efficiency solar cells based on a-Si*. Applied Physics Letters, 1983. **43**: p. 644-646.
20. Okuda, K., H. Okamoto, and Y. Hamakawa, *Amorphous Si/polycrystalline Si stacked solar cell having more than 12% conversion efficiency*. Japanese Journal of Applied Physics, 1983. **22**: p. L605-L607.
21. Matsuura, H., et al., *Electrical properties of n-amorphous/p-crystalline silicon heterojunctions*. Journal of Applied Physics, 1984. **55**: p. 1012-1019.
22. Matsuura, H., et al., *Metal-semiconductor junctions and amorphous-crystalline heterojunctions using B-doped hydrogenated amorphous silicon*. Applied Physics Letters, 1984. **45**: p. 433-435.
23. Taguchi, M., et al. *Improvement of the conversion efficiency of polycrystalline silicon thin film solar cell*. in *Tech. Digest 5th international Photovoltaic Science and Engineering Conference*. 1990. Kyoto, Japan.
24. Tanaka, M., et al., *Development of new a-Si/c-Si heterojunction solar cells: ACJ-HIT (artificially constructed junction-heterojunction with intrinsic thin-layer)*. Japanese Journal of Applied Physics, 1992. **31**(11R): p. 3518-3522.
25. Taguchi, M., et al., *HITTM cells—high-efficiency crystalline Si cells with novel structure*. Progress in Photovoltaics: Research and Applications, 2000. **8**: p. 503-513.
26. Kinoshita, T., et al. *The approaches for high efficiency HITTM solar cell with very thin (<100 μm) silicon wafer over 23%*. in *26th European Photovoltaic Solar Energy Conference and Exhibition*. 2011. Hamburg, Germany.
27. Wilhelm, H., H.-W. Schock, and R. Scheer, *Interface recombination in heterojunction solar cells: Influence of buffer layer thickness*. Journal of Applied Physics, 2011. **109**(8): p. 084514.
28. Scheer, R., *Activation energy of heterojunction diode currents in the limit of interface recombination*. Journal of Applied Physics, 2009. **105**(10): p. 104505.

29. Li, N.S.-Y., *GaN on ZnO: A new approach to solid state lighting*, in *Electrical and Computer Engineering*. 2009, Georgia Institute of Technology. p. 249.
30. Wang, Z.L., *Zinc oxide nanostructures: growth, properties and applications*. *Journal of Physics: Condensed Matter*, 2004. **16**(25): p. R829-R858.
31. Fortunato, E.M.C., et al., *High mobility indium free amorphous oxide thin film transistors*. *Applied Physics Letters*, 2008. **92**(22): p. 222103.
32. Fortunato, E., P. Barquinha, and R. Martins, *Oxide Semiconductor Thin-Film Transistors: A Review of Recent Advances*. *Advanced Materials*, 2012. **24**(22): p. 2945-2986.
33. Tsukazaki, A., et al., *High Electron Mobility Exceeding $10^4 \text{ cm}^2 \text{ V}^{-1} \text{ s}^{-1}$ in $\text{Mg}_x \text{Zn}_{1-x} \text{O}/\text{ZnO}$ Single Heterostructures Grown by Molecular Beam Epitaxy*. *Applied Physics Express*, 2008. **1**(5): p. 055004.
34. Tampo, H., et al., *Polarization-induced two-dimensional electron gases in ZnMgO/ZnO heterostructures*. *Applied Physics Letters*, 2008. **93**(20): p. 202104.
35. Remashan, K., et al., *High Performance MOCVD-Grown ZnO Thin-Film Transistor with a Thin MgZnO Layer at Channel/Gate Insulator Interface*. *Journal of The Electrochemical Society*, 2010. **157**(12): p. H1121-H1126.
36. Nayak, P.K., et al., *Spin-coated Ga-doped ZnO transparent conducting thin films for organic light-emitting diodes*. *Journal of Physics D: Applied Physics*, 2009. **42**(3): p. 035102.
37. Huang, Y.-C., et al., *Characterizations of gallium-doped ZnO films on glass substrate prepared by atmospheric pressure metal-organic chemical vapor deposition*. *Thin Solid Films*, 2009. **517**(18): p. 5537-5542.
38. Zhao, J., X.W. Sun, and S.T. Tan, *Bandgap-Engineered Ga-Rich GaZnO Thin Films for UV Transparent Electronics*. *IEEE Transactions on Electron Devices*, 2009. **56**(12): p. 2995-2999.
39. Ye, J.D., et al., *Gallium doping dependence of single-crystal n-type ZnO grown by metal organic chemical vapor deposition*. *Journal of Crystal Growth*, 2005. **283**(3-4): p. 279-285.
40. Hussain, B., et al. *Applications and synthesis of zinc oxide: An emerging wide bandgap material*. in *2013 High Capacity Optical Networks and Enabling Technologies*. 2013.
41. Hussain, B., et al. *Is ZnO as a universal semiconductor material an oxymoron?* 2014.

42. Assunção, V., et al., *Influence of the deposition pressure on the properties of transparent and conductive ZnO:Ga thin-film produced by r.f. sputtering at room temperature*. Thin Solid Films, 2003. **427**(1–2): p. 401-405.
43. Yu, X., et al., *Preparation and properties of ZnO:Ga films prepared by r.f. magnetron sputtering at low temperature*. Applied Surface Science, 2005. **239**(2): p. 222-226.
44. Liu, Z.F., et al., *Epitaxial growth and properties of Ga-doped ZnO films grown by pulsed laser deposition*. Journal of Crystal Growth, 2003. **259**(1–2): p. 130-136.
45. Henley, S.J., M.N.R. Ashfold, and D. Cherns, *The growth of transparent conducting ZnO films by pulsed laser ablation*. Surface and Coatings Technology, 2004. **177–178**: p. 271-276.
46. Yamada, T., et al., *Ingrain and grain boundary scattering effects on electron mobility of transparent conducting polycrystalline Ga-doped ZnO films*. Journal of Applied Physics, 2010. **107**(12): p. 123534.
47. Hahn, B., et al., *MOCVD layer growth of ZnO using DMZn and tertiary butanol*. Semiconductor Science and Technology, 1998. **13**(7): p. 788.
48. Vinodkumar, R., et al., *Structural, spectroscopic and electrical studies of nanostructured porous ZnO thin films prepared by pulsed laser deposition*. Spectrochimica Acta Part A: Molecular and Biomolecular Spectroscopy, 2014. **118**: p. 724-732.
49. Wang, J., et al., *Growth Parameters and Substrate Treatment for the MOCVD Growth of ZnO*. physica status solidi (a), 2005. **202**(10): p. 1967-1972.
50. Nicolay, S., S. Faÿ, and C. Ballif, *Growth Model of MOCVD Polycrystalline ZnO*. Crystal Growth & Design, 2009. **9**(11): p. 4957-4962.
51. Roro, K.T., et al., *Influence of metal organic chemical vapor deposition growth parameters on the luminescent properties of ZnO thin films deposited on glass substrates*. Journal of Applied Physics, 2008. **103**(5): p. 053516.
52. Choi, Y.S., et al., *Effect of VI/II Gas Ratio on the Epitaxial Growth of ZnO Films by Metalorganic Chemical Vapor Deposition*. Japanese Journal of Applied Physics, 2011. **50**(10R): p. 105502.
53. Kong, B.H., et al., *Influence of VI/II ratios on the growth of ZnO thin films on sapphire substrates by low temperature MOCVD*. Thin Solid Films, 2010. **518**(11): p. 2975-2979.
54. Pagni, O. and A.W.R. Leitch, *Influence of VI:II ratio on the properties of MOCVD-grown ZnO thin films*. physica status solidi (a), 2004. **201**(10): p. 2213-2218.

55. Ortiz, T., et al., *Thickness uniformity and optical evaluation of RF sputtered ZnO thin films for device application*. To be submitted, 2017.
56. Janotti, A. and C.G. Van de Walle, *Oxygen vacancies in ZnO*. Applied Physics Letters, 2005. **87**(12): p. 122102.
57. Cuscó, R., et al., *Temperature dependence of Raman scattering in ZnO* . Physical Review B, 2007. **75**(16): p. 165202.
58. Biswal, R., et al., *Indium Doped Zinc Oxide Thin Films Deposited by Ultrasonic Chemical Spray Technique, Starting from Zinc Acetylacetonate and Indium Chloride*. Materials, 2014. **7**(7).
59. Maldonado, F. and A. Stashans, *Al-doped ZnO: Electronic, electrical and structural properties*. Journal of Physics and Chemistry of Solids, 2010. **71**(5): p. 784-787.
60. Hirata, G.A., et al., *Synthesis and optoelectronic characterization of gallium doped zinc oxide transparent electrodes*. Thin Solid Films, 1996. **288**(1-2): p. 29-31.
61. Aoki, T., Y. Hatanaka, and D.C. Look, *ZnO diode fabricated by excimer-laser doping*. Applied Physics Letters, 2000. **76**(22): p. 3257-3258.
62. Kim, K.-K., et al., *Realization of p-type ZnO thin films via phosphorus doping and thermal activation of the dopant*. Applied Physics Letters, 2003. **83**(1): p. 63-65.
63. Look, D.C. and B. Claflin, *P-type doping and devices based on ZnO*. physica status solidi (b), 2004. **241**(3): p. 624-630.
64. Ding, P., et al., *p-type non-polar m-plane ZnO films grown by plasma-assisted molecular beam epitaxy*. Journal of Crystal Growth, 2011. **331**(1): p. 15-17.
65. Ding, P., et al., *Growth of p-type a-plane ZnO thin films on r-plane sapphire substrates by plasma-assisted molecular beam epitaxy*. Materials Letters, 2012. **71**: p. 18-20.
66. Schirra, M., et al., *Stacking fault related 3.31-eV luminescence at 130-meV acceptors in zinc oxide*. Physical Review B, 2008. **77**(12): p. 125215.
67. Tainoff, D., et al., *Competition between exciton-phonon interaction and defects states in the 3.31 eV band in ZnO*. Physical Review B, 2010. **81**(11): p. 115304.
68. Koike, K., et al., *Piezoelectric Carrier Confinement by Lattice Mismatch at ZnO/Zn_{0.6}Mg_{0.4}O Heterointerface*. Japanese Journal of Applied Physics, 2004. **43**(10B): p. L1372.
69. Hoffman, R.L., B.J. Norris, and J.F. Wager, *ZnO-based transparent thin-film transistors*. Applied Physics Letters, 2003. **82**(5): p. 733-735.

70. Carcia, P.F., et al., *Transparent ZnO thin-film transistor fabricated by rf magnetron sputtering*. Applied Physics Letters, 2003. **82**(7): p. 1117-1119.
71. Bernal-Correa, R., et al., *Design of the TCO (ZnO:Al) thickness for glass/TCO/CdS/CIGS/Mo solar cells*. Journal of Physics D: Applied Physics, 2016. **49**(12): p. 125601.
72. Kobayashi, H., et al., *Increases in photovoltage of "indium tin oxide/silicon oxide/mat-textured n-silicon" junction solar cells by silicon preoxidation and annealing processes*. Journal of Applied Physics, 1993. **74**(7): p. 4756-4761.
73. Dietl, T., et al., *Zener Model Description of Ferromagnetism in Zinc-Blende Magnetic Semiconductors*. Science, 2000. **287**(5455): p. 1019.
74. Singh, R., G.F. Alapatt, and A. Lakhtakia, *Making Solar Cells a Reality in Every Home: Opportunities and Challenges for Photovoltaic Device Design*. IEEE Journal of the Electron Devices Society, 2013. **1**(6): p. 129-144.
75. Ibrahim, A.A. and A. Ashour, *ZnO/Si solar cell fabricated by spray pyrolysis technique*. Journal of Materials Science: Materials in Electronics, 2006. **17**(10): p. 835-839.
76. Zhang, W., et al., *Influence of growth conditions on photovoltaic effect of ZnO/Si heterojunction*. Solar Energy Materials and Solar Cells, 2008. **92**(8): p. 949-952.
77. Shen, L., et al., *Studies on fabrication and characterization of a ZnO/p-Si-based solar cell*. Superlattices and Microstructures, 2010. **48**(4): p. 426-433.
78. Knutsen, K.E., et al., *Prediction of high efficiency ZnMgO/Si solar cells suppressing carrier recombination by conduction band engineering*. physica status solidi (a), 2013. **210**(3): p. 585-588.
79. Baturay, S., Y.S. Ocak, and D. Kaya, *The effect of Gd doping on the electrical and photoelectrical properties of Gd:ZnO/p-Si heterojunctions*. Journal of Alloys and Compounds, 2015. **645**: p. 29-33.
80. Hussain, B., A. Ebong, and I. Ferguson, *Zinc oxide as an active n-layer and antireflection coating for silicon based heterojunction solar cell*. Solar Energy Materials and Solar Cells, 2015. **139**: p. 95-100.
81. Pietruszka, R., et al., *Improved efficiency of n-ZnO/p-Si based photovoltaic cells by band offset engineering*. Solar Energy Materials and Solar Cells, 2016. **147**: p. 164-170.
82. Hussain, B., et al. *On structural and electrical characterization of n-ZnO/p-Si single heterojunction solar cell*. in *2016 IEEE 43rd Photovoltaic Specialists Conference (PVSC)*. 2016.

83. Mishra, P., et al. *Temperature optimization for MOCVD-based growth of ZnO thin films*. in *2014 11th Annual High Capacity Optical Networks and Emerging/Enabling Technologies (Photonics for Energy)*. 2014.
84. Wu, C.C., et al., *Effects of Growth Conditions on Structural Properties of ZnO Nanostructures on Sapphire Substrate by Metal–Organic Chemical Vapor Deposition*. *Nanoscale Research Letters*, 2009. **4**(4): p. 377.
85. Nishimoto, N., et al., *Growth of ZnO thin films by using MOCVD with a high-speed rotating disk reactor*. *J. of the Korean Physical Soc.*, 2008. **53**: p. 2951-2954.
86. Ye, J., et al., *Raman and photoluminescence of ZnO films deposited on Si (111) using low-pressure metalorganic chemical vapor deposition*. *Journal of Vacuum Science & Technology A: Vacuum, Surfaces, and Films*, 2003. **21**(4): p. 979-982.
87. Klingshirn, C.F., et al., *Chapter 3: Growth*, in *Zinc Oxide: From Fundamental Properties towards Novel Applications*. 2010, Springer Science and Business Media: Berlin, Germany.
88. Kim, H., et al., *Transparent conducting aluminum-doped zinc oxide thin films for organic light-emitting devices*. *Applied Physics Letters*, 2000. **76**(3): p. 259-261.
89. Tan, S.T., et al., *Properties of polycrystalline ZnO thin films by metal organic chemical vapor deposition*. *Journal of Crystal Growth*, 2005. **281**(2–4): p. 571-576.
90. Hussain, B. and A. Ebong, *Specifications of ZnO growth for heterostructure solar cell and PCID based simulations*. *Data in Brief*, 2015. **5**: p. 516-521.
91. Mishra, P., et al. *Spatial analysis of ZnO thin films prepared by vertically aligned MOCVD*. in *2014 11th Annual High Capacity Optical Networks and Emerging/Enabling Technologies (Photonics for Energy)*. 2014.
92. Singh, A.K., *Advanced x-ray techniques in research and industry*. 2005: IOS Press.
93. Khan, T.M., T. Bibi, and B. Hussain, *Synthesis and optical study of heat-treated ZnO nanopowder for optoelectronic applications*. *Bulletin of Materials Science*, 2015. **38**(7): p. 1851-1858.
94. Stadler, A., *Transparent Conducting Oxides—An Up-To-Date Overview*. *Materials*, 2012. **5**(4).
95. Chanta, E., et al., *Effect of ZnO Double Layer as Anti-Reflection Coating Layer in ZnO Dye-Sensitized Solar Cells*. *Energy Procedia*, 2015. **79**: p. 879-884.
96. Mohamed, S.H. and M. Raaif, *Effects of thickness and rf plasma oxidizing on structural and optical properties of SiO_xN_y thin films*. *Surface and Coatings Technology*, 2010. **205**(2): p. 525-532.

97. Choudhary, N., D.K. Kharat, and D. Kaur, *Structural, electrical and mechanical properties of magnetron sputtered NiTi/PZT/TiO_x thin film heterostructures*. Surface and Coatings Technology, 2011. **205**(11): p. 3387-3396.
98. Zhang, Y., Q. Song, and Z. Sun, *Research on Thin Film Thickness Uniformity for Deposition of Rectangular Planar Sputtering Target*. Physics Procedia, 2012. **32**: p. 903-913.
99. Jiang, C.Z., et al., *Uniform film in large areas deposited by magnetron sputtering with a small target*. Surface and Coatings Technology, 2013. **229**: p. 222-225.
100. Gaspar, G., et al., *Identification of defects causing performance degradation of high temperature n-type Czochralski silicon bifacial solar cells*. Solar Energy Materials and Solar Cells, 2016. **153**: p. 31-43.
101. Choi, Y.-O., et al., *Influences of thickness-uniformity and surface morphology on the electrical and optical properties of sputtered CdTe thin films for large-area II–VI semiconductor heterostructured solar cells*. Materials Science and Engineering: B, 2010. **171**(1–3): p. 73-78.
102. Karpov, V.G., A.D. Compaan, and D. Shvydka, *Effects of nonuniformity in thin-film photovoltaics*. Applied Physics Letters, 2002. **80**(22): p. 4256-4258.
103. Müller, J., et al., *TCO and light trapping in silicon thin film solar cells*. Solar Energy, 2004. **77**(6): p. 917-930.
104. Müller, J., et al., *Development of highly efficient thin film silicon solar cells on texture-etched zinc oxide-coated glass substrates*. Solar Energy Materials and Solar Cells, 2001. **66**(1–4): p. 275-281.
105. Kluth, O., et al., *Texture etched ZnO:Al coated glass substrates for silicon based thin film solar cells*. Thin Solid Films, 1999. **351**(1–2): p. 247-253.
106. Baxter, J.B. and E.S. Aydil, *Nanowire-based dye-sensitized solar cells*. Applied Physics Letters, 2005. **86**(5): p. 053114.
107. Law, M., et al., *Nanowire dye-sensitized solar cells*. Nat Mater, 2005. **4**(6): p. 455-459.
108. Martinson, A.B.F., et al., *ZnO Nanotube Based Dye-Sensitized Solar Cells*. Nano Letters, 2007. **7**(8): p. 2183-2187.
109. Jiang, C.Y., et al., *Improved dye-sensitized solar cells with a ZnO-nanoflower photoanode*. Applied Physics Letters, 2007. **90**(26): p. 263501.
110. Chhajed, S., et al., *Nanostructured multilayer graded-index antireflection coating for Si solar cells with broadband and omnidirectional characteristics*. Applied Physics Letters, 2008. **93**(25): p. 251108.

111. Pethuraja, G.G., et al., *Current-voltage characteristics of ITO/p-Si and ITO/n-Si contact interfaces*. *Advances in Materials Physics and Chemistry*, 2012. **2**(2): p. 59-62.
112. Basore, P.A., *Numerical modeling of textured silicon solar cells using PC-1D*. *IEEE Transactions on Electron Devices*, 1990. **37**(2): p. 337-343.
113. Clugston, D.A. and P.A. Basore. *PC1D version 5: 32-bit solar cell modeling on personal computers*. in *Conference Record of the Twenty Sixth IEEE Photovoltaic Specialists Conference - 1997*. 1997.
114. Haug, H., et al., *A Graphical User Interface for Multivariable Analysis of Silicon Solar Cells Using Scripted PC1D Simulations*. *Energy Procedia*, 2013. **38**: p. 72-79.
115. Ginige, R., et al., *Characterization of Ge-on-Si virtual substrates and single junction GaAs solar cells*. *Semiconductor Science and Technology*, 2006. **21**(6): p. 775.
116. van Sark, W.G.J.H.M., et al., *Enhancing solar cell efficiency by using spectral converters*. *Solar Energy Materials and Solar Cells*, 2005. **87**(1-4): p. 395-409.
117. Lien, S.-Y. and D.-S. Wu, *Simulation and fabrication of heterojunction silicon solar cells from numerical computer and hot-wire CVD*. *Progress in Photovoltaics: Research and Applications*, 2009. **17**(7): p. 489-501.
118. Ali, A., B. Hussain, and A. Ebong. *Computer modeling of n-ZnO/p-Si single heterojunction bifacial solar Cell*. in *2016 IEEE 43rd Photovoltaic Specialists Conference (PVSC)*. 2016.
119. Ali, A., B. Hussain, and A. Ebong, *Computer simulation of the impact of interface trap density on n-ZnO/p-Si single heterojunction solar cells*, in *PVSEC-2016*. 2016.
120. Sundaram, K.B. and A. Khan, *Work function determination of zinc oxide films*. *Journal of Vacuum Science & Technology A: Vacuum, Surfaces, and Films*, 1997. **15**(2): p. 428-430.
121. Jiang, X., C.L. Jia, and B. Szyszka, *Manufacture of specific structure of aluminum-doped zinc oxide films by patterning the substrate surface*. *Applied Physics Letters*, 2002. **80**(17): p. 3090-3092.
122. Lee, J.Y., et al., *Optimizing n-ZnO/p-Si heterojunctions for photodiode applications*. *Thin Solid Films*, 2002. **403-404**: p. 553-557.
123. Lee, J.Y., et al., *Characterization of films and interfaces in n-ZnO/p-Si photodiodes*. *Thin Solid Films*, 2002. **420-421**: p. 112-116.

124. Shih, J.-L., *Zinc oxide-silicon heterojunction solar cells by sputtering*, in *Department of Electrical and Computer Engineering*. 2007, McGill University. p. 118.
125. Ruan, Y.C. and W.Y. Ching, *An effective dipole theory for band lineups in semiconductor heterojunctions*. *Journal of Applied Physics*, 1987. **62**(7): p. 2885-2897.
126. Avasthi, S., *Crystalline-silicon/organic heterojunctions for solar photovoltaics*, in *Department of Electrical Engineering*. 2011, Princeton University. p. 105.
127. Kerr, M.J. and A. Cuevas, *Generalized analysis of the illumination intensity vs. open-circuit voltage of solar cells*. *Solar Energy*, 2004. **76**(1–3): p. 263-267.
128. Untila, G.G., T.N. Kost, and A.B. Chebotareva, *Bifacial 8.3%/5.4% front/rear efficiency ZnO:Al/n-Si heterojunction solar cell produced by spray pyrolysis*. *Solar Energy*, 2016. **127**: p. 184-197.
129. Gandla, S.B. and M. Nagesh, *Effect of sputtered zinc oxide as anti-reflection coating in amorphous silicon solar cell*. *International Journal of Science and Research*, 2016. **5**(2): p. 1376-1379.
130. Jaramillo, R., et al., *Using Atom-Probe Tomography to Understand ZnO:Al/SiO₂/Si Schottky Diodes*. *Physical Review Applied*, 2016. **6**(3): p. 034016.
131. Jin, C., et al., *Epitaxial growth of zinc oxide thin films on silicon*. *Materials Science and Engineering: B*, 2005. **117**(3): p. 348-354.
132. Vispute, R.D., et al., *Epitaxial growth of AlN thin films on silicon (111) substrates by pulsed laser deposition*. *Journal of Applied Physics*, 1995. **77**(9): p. 4724-4728.
133. Fei-Fei, W., et al., *Photoluminescence and electroluminescence properties of ZnO films on p-type silicon wafers*. *Chinese Physics*, 2007. **16**(6): p. 1790.
134. Hu, J. and R.G. Gordon, *Atmospheric pressure chemical vapor deposition of gallium doped zinc oxide thin films from diethyl zinc, water, and triethyl gallium*. *Journal of Applied Physics*, 1992. **72**(11): p. 5381-5392.
135. Kaul, A.R., et al., *MOCVD of pure and Ga-doped epitaxial ZnO*. *Superlattices and Microstructures*, 2005. **38**(4–6): p. 272-282.
136. Ghosh, A.K., C. Fishman, and T. Feng, *SnO₂/Si solar cells—heterostructure or Schottky-barrier or MIS-type device*. *Journal of Applied Physics*, 1978. **49**(6): p. 3490-3498.
137. Li, X., et al., *Graphene-On-Silicon Schottky Junction Solar Cells*. *Advanced Materials*, 2010. **22**(25): p. 2743-2748.

138. Miao, X., et al., *High Efficiency Graphene Solar Cells by Chemical Doping*. Nano Letters, 2012. **12**(6): p. 2745-2750.
139. Hussain, B., *Improvement in Open Circuit Voltage of n-ZnO/p-Si Solar Cell by Using Amorphous-ZnO at the Interface*. To be submitted, 2017.
140. Ricca, A. and C.W. Bauschlicher Jr, *Accurate D0 values for SiF and SiF+*. Chemical Physics Letters, 1998. **287**(3-4): p. 239-242.
141. Michalak, D.J., et al., *Nanopatterning Si(111) surfaces as a selective surface-chemistry route*. Nat Mater, 2010. **9**(3): p. 266-271.
142. Das, S.C., et al., *Band Gap Tuning in ZnO Through Ni Doping via Spray Pyrolysis*. The Journal of Physical Chemistry C, 2013. **117**(24): p. 12745-12753.
143. Mayer, M.A., et al., *Band structure engineering of ZnO_{1-x}Sex alloys*. Applied Physics Letters, 2010. **97**(2): p. 022104.
144. Mayer, M.A., et al., *Tuning structural, electrical, and optical properties of oxide alloys: ZnO_{1-x}Sex*. Journal of Applied Physics, 2012. **111**(11): p. 113505.

PUBLICATIONS

Journal Papers (Only the papers directly related to the dissertation are included below)

1. **Babar Hussain***, “Improvement in open circuit voltage of n-ZnO/p-Si solar cell by using amorphous-ZnO at the Interface” to be submitted.
2. T. Ortiz, C. Conde, T. M. Khan, and **Babar Hussain***, “Thickness uniformity and optical evaluation of RF sputtered ZnO thin films for device application” to be submitted.
3. **Babar Hussain***, A. Ebong, and I. Ferguson, “Zinc oxide as an active n-layer and antireflection coating for silicon based heterojunction solar cell” *Solar Energy Materials & Solar Cells*, Vol. 139, pp. 95–100, 2015. (IF: 5.016, Citations: 19)
4. **Babar Hussain*** and A. Ebong, “Specifications of ZnO growth for heterostructure solar cell and PC1D based simulations” *Data in Brief*, Vol. 5, pp. 515–521, 2015.
5. T. M. Khan*, T. Bibi, **Babar Hussain**, “Synthesis and optical study of heat treated ZnO Nanopowder for optoelectronic applications” *Bulletin of Materials Science*, 2015. (IF: 1.017)
6. T. M. Khan* and **Babar Hussain**, “Study of UV-Green Emissions and Spectroscopic Properties of Polycrystalline ZnO Thin Films” *International Journal of Chemistry and Material Science*, Vol. 3, pp. 001–011, 2015.
7. **Babar Hussain***, M. Nawaz, M. Ahmed, and M. Y. A. Raja, “Measurement of thickness and refractive index using femtosecond and terahertz pulses” *Laser Physics Letters*, Vol. 10, No. 5 (6pp), 2013. (IF: 2.458, Citations: 8)

Conference Papers

8. **Babar Hussain***, “Optimization of bandgap and electron affinity of zinc oxide for n-ZnO/p-Si heterojunction solar cell” *Proc. of the 44th IEEE Photovoltaic Specialists Conference*, submitted.
9. **Babar Hussain*** and Thiara Ortiz, “Spatial thickness uniformity and structural evaluation of RF sputtered ZnO thin films for solar cell” *Proc. of the 44th IEEE Photovoltaic Specialists Conference*, submitted.

10. N. Bezawada, K. Batchu, **Babar Hussain**, and A. Ebong*, “Understanding the influence of tellurium oxide in front Ag paste for contacting silicon solar cells with homogeneous high sheet resistance emitter” Proc. of the 26th International Photovoltaic Science and Engineering Conference, Oct 2016, in press.
11. **Babar Hussain***, A. Ali, V. Unsur, and A. Ebong, “On structural and electrical characterization of n-ZnO/p-Si single heterojunction solar cell” Proc. of the 43rd IEEE Photovoltaics Specialist Conference, June 2016, DOI: 10.1109/PVSC.2016.7749952.
12. A. Ali, **Babar Hussain**, and A. Ebong*, “Thin bifacial n-ZnO/p-Si single heterojunction solar cells” Proc. of the 43rd IEEE Photovoltaics Specialist Conference, June 2016, DOI: 10.1109/PVSC.2016.7749665.
13. V. Unsur*, **Babar Hussain**, and A. Ebong, “Complete recovery of light induced degradation of Cz silicon solar cells with rapid thermal processing” Proc. of the 43rd IEEE Photovoltaics Specialist Conference, June 2016, DOI: 10.1109/PVSC.2016.7749695.
14. **Babar Hussain***, A. Ebong, and I. Ferguson, “Zinc oxide and silicon based heterojunction solar cell model” Proc. of the 42nd IEEE Photovoltaics Specialist Conference, June 2015, DOI: 10.1109/PVSC.2015.7356242. (Citations: 3)
15. B. Kucukgok*, **Babar Hussain**, C. Zhou, I. T. Ferguson, N. Lu, “Thermoelectric properties of ZnO thin films grown by metal-organic chemical vapor deposition” MRS Proceedings, Vol. 1805, 2015.
16. B. Kucukgok*, **Babar Hussain**, C. Zhou, I. T. Ferguson, N. Lu, “Investigation of thermoelectric properties of p-type GaN thin films” MRS Proceedings, Vol. 1774, 2015.
17. P. Mishra, B. Monroe, **Babar Hussain***, and I. Ferguson, “Temperature optimization for MOCVD-based growth of ZnO thin films” Proc. of the IEEE 11th International HONET Conference, pp. 238–242, 2014. (paper with my students Mishra and Monroe) (Citations: 3)
18. P. Mishra, R. Patel, **Babar Hussain***, J. Stansell, B. Kucukgok, M. Y. Raja, N. Lu, and I. Ferguson, “Spatial analysis of ZnO thin films prepared by vertically aligned MOCVD” Proc. of the IEEE 11th International HONET Conference, pp. 67–70, 2014. (paper with my students Mishra, Patel, and Stansell) (Citations: 4)

19. **Babar Hussain***, M. Y. A. Raja, N. Lu, and I. Ferguson, “Applications and synthesis of zinc oxide: an emerging wide bandgap material” Proc. of the IEEE 10th International HONET-CNS Conference, pp. 88–93, 2013. (Citations: 5)

Invited Papers

20. **Babar Hussain***, B. Kucukgok, M. Y. A. Raja, B. Klein, N. Lu, and I. T. Ferguson, “Is ZnO as a universal semiconductor material an oxymoron?” Proc. of SPIE, Vol. 8987, pp. 898718-1–14, 2014. (Citations: 6)